IOWA STATE UNIVERSITY
Digital Repository

Retrospective Theses and Dissertations

Iowa State University Capstones, Theses and Dissertations

1997

NDE data fusion using morphological approaches

Young-Won Song
Iowa State University

Follow this and additional works at: https://lib.dr.iastate.edu/rtd

 Part of the Electrical and Electronics Commons

Recommended Citation
Song, Young-Won, "NDE data fusion using morphological approaches " (1997). *Retrospective Theses and Dissertations*. 11748.
https://lib.dr.iastate.edu/rtd/11748

This Dissertation is brought to you for free and open access by the Iowa State University Capstones, Theses and Dissertations at Iowa State University Digital Repository. It has been accepted for inclusion in Retrospective Theses and Dissertations by an authorized administrator of Iowa State University Digital Repository. For more information, please contact digirep@iastate.edu.

INFORMATION TO USERS

This manuscript has been reproduced from the microfilm master. UMI films the text directly from the original or copy submitted. Thus, some thesis and dissertation copies are in typewriter face, while others may be from any type of computer printer.

The quality of this reproduction is dependent upon the quality of the copy submitted. Broken or indistinct print, colored or poor quality illustrations and photographs, print bleedthrough, substandard margins, and improper alignment can adversely affect reproduction.

In the unlikely event that the author did not send UMI a complete manuscript and there are missing pages, these will be noted. Also, if unauthorized copyright material had to be removed, a note will indicate the deletion.

Oversize materials (e.g., maps, drawings, charts) are reproduced by sectioning the original, beginning at the upper left-hand corner and continuing from left to right in equal sections with small overlaps. Each original is also photographed in one exposure and is included in reduced form at the back of the book.

Photographs included in the original manuscript have been reproduced xerographically in this copy. Higher quality 6" x 9" black and white photographic prints are available for any photographs or illustrations appearing in this copy for an additional charge. Contact UMI directly to order.

UMI

A Bell & Howell Information Company
300 North Zeeb Road, Ann Arbor MI 48106-1346 USA
313/761-4700 800/521-0600

NDE data fusion using morphological approaches

by

Young-Won Song

A dissertation submitted to the graduate faculty

in partial fulfillment of the requirements for the degree of

DOCTOR OF PHILOSOPHY

Major: Electrical Engineering (Communications and Signal Processing)

Major Professor: Satish S. Udpa

Iowa State University

Ames, Iowa

1997

Copyright © Young-Won Song, 1997. All right reserved.

UMI Number: 9725461

UMI Microform 9725461
Copyright 1997, by UMI Company. All rights reserved.

This microform edition is protected against unauthorized copying under Title 17, United States Code.

UMI
300 North Zeeb Road
Ann Arbor, MI 48103

Graduate College
Iowa State University

This is to certify that the Doctoral dissertation of

Young-Won Song

has met the dissertation requirements of Iowa State University

Signature was redacted for privacy.

Committee Member

Signature was redacted for privacy.

Committee Member

Signature was redacted for privacy.

Committee Member

Signature was redacted for privacy.

Committee Member

Signature was redacted for privacy.

Major Professor

Signature was redacted for privacy.

For the Major Program

Signature was redacted for privacy.

For the Graduate College

TABLE OF CONTENTS

LIST OF FIGURES vi

LIST OF TABLES x

ACKNOWLEDGEMENTS xi

ABSTRACT xii

CHAPTER 1 INTRODUCTION 1

Nondestructive Evaluation 1

Data Fusion in NDE 2

Literature Review: NDE Data Fusion Approaches 5

Motivation and Objectives 6

Scope of the Dissertation 8

CHAPTER 2 FUNDAMENTALS OF ULTRASONIC AND EDDY CURRENT TEST METHODS 9

Ultrasonic Test Methods 9

Eddy Current Test Methods 15

CHAPTER 3 MORPHOLOGY IN IMAGE PROCESSING 19

Binary Morphology in Image Processing 19

Mathematical definitions 20

Algebraic properties 22

Morphological filters 24

Simulation examples 29

Gray Scale Morphology in Image Processing 29

Mathematical definitions 32

Algebraic properties 34

Simulation examples 36

CHAPTER 4 A NEW MORPHOLOGICAL ALGORITHM FOR REDUCING SPECKLE NOISE IN ULTRASONIC IMAGES 48

Literature Review: Noise Reduction Approaches 48

Conventional Lowpass and Median Filters 50

Description of the Proposed Speckle Noise Reduction Algorithm 51

Residual image generation algorithm 54

Gating process algorithm 58

Feature extraction algorithm 59

Contrast enhancement algorithm 59

CHAPTER 5 A NEW MORPHOLOGICAL ALGORITHM FOR FUSING ULTRASONIC AND EDDY CURRENT IMAGES 70

Data Fusion Using LMMSE Filters 70

Description of the Proposed Data Fusion Algorithm 72

CHAPTER 6 SIMULATION RESULTS 80

Results of the Proposed Speckle Noise Reduction Algorithm 80

Results of the Proposed Data Fusion Algorithm 82

CHAPTER 7 PERFORMANCE EVALUATION 112

Performance of the Proposed Speckle Noise Reduction Algorithm 112

Performance of the Proposed NDE Data Fusion Algorithm 115

CHAPTER 8 CONCLUSIONS AND FUTURE WORK 146

Summary of Contributions 146

Summary of Dissertation 146

Future Work 148

APPENDIX MATHEMATICAL DESCRIPTION OF RESIDUAL IMAGES 149

BIBLIOGRAPHY 151

LIST OF FIGURES

Figure 1.1. Block diagram of a generic NDE data fusion system. 5

Figure 2.1. Block diagram of a typical ultrasonic test system. 10

Figure 2.2. Pulse-echo and pitch-catch modes of inspection. 10

Figure 2.3. Examples of C-scan ultrasonic images. 16

Figure 2.4. Examples of eddy current images. 18

Figure 3.1. Example of structuring element decomposition. 23

Figure 3.2. Binary morphological outputs obtained from a square-type binary image using a disk-type symmetric structuring element. 26

Figure 3.3. Binary morphological outputs obtained from a square-type binary image using a line-type non-symmetric structuring element. 26

Figure 3.4. Binary morphological outputs obtained from a dented square-type binary image using a disk-type symmetric structuring element. 26

Figure 3.5. Binary morphological outputs obtained from a protruding square-type binary image using a disk-type symmetric structuring element. 27

Figure 3.6. Binary morphological outputs obtained from the binary scale ultrasonic image using a square-type symmetric structuring element of size 3 x 3 pixel. 30

Figure 3.7. Example of duality relation between erosion and dilation operations. 35

Figure 3.8. Gray scale morphological outputs obtained from a 1-dimensional gray scale signal with low density noise using a symmetric structuring element of length 3. 37

Figure 3.9. Gray scale morphological outputs obtained from a 1-dimensional gray scale signal with high density noise using a symmetric structuring element of length 3. 39

Figure 3.10. Gray scale image containing positive and negative peaks and the corresponding line scan. 42

Figure 3.11. Gray scale morphological outputs obtained from the gray scale image shown in Figure 3.10(a). 43

Figure 3.12. Gray scale morphological outputs obtained using the gray scale C-scan ultrasonic image and a flat symmetric square-type structuring element of size 3x3 pixels. 45

Figure 4.1. Overall block diagram of the NDE data fusion algorithm using morphological approaches. 51

Figure 4.2. Block diagram of the proposed speckle noise reduction algorithm. 52

Figure 4.3. Specimen used in validation studies. 53

Figure 4.4. Block diagram of the residual image generation algorithm. 55

Figure 4.5. Sample images obtained using the residual image generation algorithm. 57

Figure 4.6. Block diagram of the gating algorithm. 58

Figure 4.7. Sample images obtained using the gating algorithm. 60

Figure 4.8. Histograms of the gated residual images. 61

Figure 4.9. Histograms of the residual images. 62

Figure 4.10. Block diagram of the feature extraction algorithm. 63

Figure 4.11. Images obtained using the feature extraction algorithm. 64

Figure 4.12. Block diagram of the contrast enhancement algorithm. 65

Figure 4.13. Images obtained (a) before and (b) after using the contrast enhancement algorithm. 66

Figure 4.14. Sample images obtained using conventional noise reduction filters and the proposed speckle noise reduction algorithm. 67

Figure 4.15. Example of C-scan image. 68

Figure 4.16. Noise reduced images. 69

Figure 5.1. Block diagram of the LMMSE filter employing multiple inputs. 71

Figure 5.2. Block diagram of the proposed morphological data fusion algorithm. 73

Figure 5.3. Original ultrasonic and eddy current images. 75

Figure 5.4. Granulometric size distribution and density, and restored binary image obtained using the algorithm shown in Figure 5.2. 76

Figure 5.5. Line scans obtained from the original ultrasonic and eddy current images. 77

Figure 5.6. Fused image and line scan obtained from the image after using the proposed algorithm. 78

Figure 5.7. Fused image and line scan obtained from the image after using the multi-resolution decomposition technique employing LMMSE filters. 79

Figure 6.1. Details of the test specimens used for validating the proposed speckle noise reduction algorithm. 84

Figure 6.2. Original C-scan ultrasonic images obtained from the specimens shown in Figure 6.1. 86

Figure 6.3. Fourier spectra of the ultrasonic images shown in Figure 6.2. 88

Figure 6.4. Lowpass filtered images. 90

Figure 6.5. Median filtered images. 92

Figure 6.6. Speckle noise reduced images obtained using the proposed algorithm. 94

Figure 6.7. Details of the test specimens used for validating the proposed NDE data fusion algorithm. 96

Figure 6.8. Original C-scan ultrasonic images. 98

Figure 6.9. Original eddy current images. 100

Figure 6.10. Speckle noise reduced images obtained using the proposed speckle noise reduction algorithm. 102

Figure 6.11. Granulometric size distributions of the images obtained using iterative closing operations. 104

Figure 6.12. Granulometric size densities obtained using the granulometric size distributions shown in Figure 6.11. 106

Figure 6.13. Restored binary images. 108

Figure 6.14. Fused images obtained using the proposed NDE data fusion algorithm. 110

Figure 7.1. Procedure for evaluating the performance of the proposed speckle noise reduction algorithm. 116

Figure 7.2. Noise corrupted images. 118

Figure 7.3. Histograms of the noise corrupted images. 122

Figure 7.4. Histograms of the original ultrasonic images. 126

Figure 7.5. Speckle noise reduced images obtained using the proposed algorithm. 130

Figure 7.6. Fused images obtained using multi-resolution decomposition technique employing LMMSE filters. 138

Figure 7.7. Line scans obtained from the original ultrasonic images. 140

Figure 7.8. Line scans obtained from the original eddy current images. 142

Figure 7.9. Line scans obtained from the fused images. 144

LIST OF TABLES

Table 2.1.	Acoustic properties of materials.	14
Table 7.1.	Comparison of MSE of the measured original and degraded images.	117
Table 7.2.	Comparison of performance using MSE as a performance index.	134
Table 7.3.	Comparison of performance using SNR_1(dB) as a performance index.	135
Table 7.4.	Comparison of performance using SNR_2(dB) as a performance index.	136
Table 7.5.	Comparison of performance using PSNR(dB) as a performance index.	137

ACKNOWLEDGEMENTS

I would like to express my sincere gratitude and appreciation to my major professor Dr. Satish S. Udpa for his continuous guidance, support and invaluable encouragement during my graduate study. He was very kind and understanding through the course of my research. His professional and personal encouragement will leave a lasting impression.

I wish to thank to Dr. William Lord and Dr. Lalita Udpa for sharing their rich knowledge and helpful discussions. I would also like to thank to Dr. Julie A. Dickerson and Dr. Eric B. Bartlett for willingly taking the time to serve as members of my graduate committee. I would like to thank to Dr. Shreekanth Mandayam for proofreading the manuscript.

I wish to give thanks to my Korean friends who helped by sharing computer memory space for storing my manuscript. I also express my thanks to many friends here at MCRG, Department of Electrical Engineering, whose advice, help and friendship have enriched my graduate school life.

I would like to express my thanks to my parents and family for their endless support through my educational career. Finally, I express my deep thanks to my wife Moon-Hee for her invaluable advice, encouragement and endless love during my life.

ABSTRACT

The objective of most data fusion algorithms is to combine information made available by various sensors synergistically in order to enhance the overall level of information. Since information obtained from data sources such as sensors is often incomplete or imprecise in nature, the application of data fusion techniques has evoked interest in a number of fields ranging from robotics to nondestructive evaluation (NDE). In NDE applications, such techniques can be used to integrate and fuse data obtained using multiple inspection modalities to produce a more comprehensive picture of the condition of the test specimen. As an example, ultrasonic and eddy current imaging techniques are used very widely to inspect a variety of materials. Each technique offers inspection capabilities and limitations that are dictated by the underlying material/energy interaction process. The information generated using the two methods can be construed either as complementary or redundant in nature. Ideally it should be possible to utilize the redundant information to improve the signal-to-noise ratio. Likewise, it should be possible to fuse the complementary information from the two tests to increase the overall level of information made available to the analyst. Unfortunately the task of segmenting data as noise, redundant and complementary components of information can be frustrating. Consequently, most of the approaches proposed to date in NDE have relied on alternate methods.

This dissertation proposes a new algorithm for fusing ultrasonic and eddy current images employing morphological imaging processing approaches. The fusion is accomplished in two stages. The first stage basically employs morphological approaches to reduce unwanted

artifacts such as speckle noise in the ultrasonic image. The second stage extracts information about the locations and boundaries of defects on the basis of information contained in the morphological granulometric size distribution of the ultrasonic image. Data fusion is accomplished by combining information relating to the locations and boundaries of the defect obtained from the ultrasonic data with the defect depth information derived from the eddy current image. The validity of the approach is demonstrated using several experimentally derived ultrasonic and eddy current images.

CHAPTER 1 INTRODUCTION

Nondestructive Evaluation

The science of detecting defects and inhomogeneities in materials and assessing their properties without impairing the usefulness of materials is known as nondestructive evaluation (NDE). Research areas in NDE encompass a broad range of disciplines such as material science, aerospace, nuclear and electrical engineering. NDE plays a very crucial role in the inspection of aircraft engines, nuclear reactors, railroads, gas pipelines and numerous other applications where failures can contribute to catastrophic disasters. These applications impose very strict criteria with respect to reliability of materials or parts to prevent catastrophic failures. Many NDE techniques have been developed to cater to these needs. The benefits which can be derived from NDE include the following: increased productivity, improved serviceability, reliability, profit and safety [1,2].

Every NDE method involves a certain type of energy source for inspection. This energy could be ultrasonic [3,4], electromagnetic [5-8], thermal [9-11] or radiographic [2,12]. The incident energy from the source interacts with the test specimen depending on the governing physical phenomena. The received (detected) signal is analyzed and interpreted in terms of the material characteristics of the defects such as their location or shape, or properties such as conductivity, permittivity, permeability, thickness and so on [13,14]. Almost every form of energy has been utilized to inspect defects or determine material properties. The wide range of NDE techniques also suggests that no single NDE method is sufficient to completely characterize the properties of materials. Each NDE technique has its own capabilities and

limitations. The following examples illustrate this fact. Ultrasonic techniques can be used to inspect a wide variety of materials with high resolution. However, the technique suffers from several limitations including problems associated with speckle. Eddy current methods are less prone to noise compared to ultrasonic methods. However, eddy current techniques can be used only for detecting flaws in conductive materials which are not embedded deeply under the test specimen surface. Radiographic NDE techniques employ X-rays and gamma radiation as inspection energy sources. They penetrate nearly all materials and have very short wavelengths. Hence they are used to test many types of materials with high resolution. However, their application is limited due to concerns of radiation hazards and safety problems. Visual inspection techniques can be used to examine the condition of materials. Test specimens are exposed to visible light and examined using the eye or other light sensitive devices such as photo diodes. However, they are limited to surface inspection. Since each method offers a limited amount of information, it is likely that one may profitably combine information from two or more inspection techniques to obtain a more comprehensive characterization of the test specimen. Techniques for combining information are often called data fusion techniques. This dissertation presents a novel approach for combining ultrasonic and eddy current NDE data.

Data Fusion in NDE

The desire to extract unambiguous and accurate information from measurements has been a major motivation for developing more advanced sensors, test equipment and methods. In reality, no single sensor is capable of providing perfectly reliable information about a test

environment. This ambiguity often results from lack of a complete understanding of the physical phenomena governing the interaction process between the sensor and environment under test [15]. In addition, all sensors and measurement systems inherently incorporate a random uncertainty in their measurements owing to noise and human errors. The physical limitations of technologies such as operating frequencies and the size of sensors, both of which are closely related to data resolution, cause accuracy problems. As a result of these limitations, a single sensor commonly offers uncertain and partial information about the object it senses. To overcome these fundamental problems, research on methods for optimally combining data obtained from multiple sensors has been performed in a number of fields [16-18]. Such techniques are often called data fusion techniques. The areas of data fusion applications may be broadly classified into three categories [17]: military, space and industrial applications. Military applications include: intelligence analysis and situation assessment, force command and control, autonomous vehicle, avionics and electronic warfare [19]. In space applications, examples of data fusion techniques include autonomous systems designed for the maintenance and repair of satellites and the assembly of production facilities in space environment [20,21]. Industrial applications of data fusion techniques include such as material handling, and parts fabrication, inspection and assembly [22,23].

The objective of most data fusion strategies is to combine information made available by various sensors synergistically in order to enhance the overall level of information [18]. The combined data contains not only information generated by each sensor, but also provides information that cannot be inferred by either sensor acting alone. In NDE applications [24,25], such techniques can be used to integrate and fuse data obtained using multiple inspection

modalities to produce a more comprehensive picture of the condition of the test specimen. As an example, ultrasonic and eddy current imaging techniques are used very widely to inspect a variety of materials. Each technique offers inspection capabilities and limitations that are dictated by the underlying material/energy interaction process. The data generated using the two methods can be construed either as complementary or redundant in nature. Ideally it should be possible to utilize the redundant component of the information to improve the signal-to-noise ratio. Likewise, it should be possible to fuse the complementary information from the two tests to increase the overall level of information made available to the analyst. Unfortunately the task of segmenting data as noise, redundant and complementary components of information can be frustrating. Consequently, most of the approaches proposed to date in NDE have relied on alternate methods. This dissertation proposes a new morphological approach for fusing ultrasonic and eddy current NDE images.

A generic NDE data fusion system can be configured as shown in Figure 1.1. The N sensors that are used to inspect the specimen are not identical and consequently the format and content of the data may be substantially different. The data generated by the transducers may be complementary, redundant or unnecessary, relative to each other. The first step in the data fusion procedure is to minimize the unnecessary data, such as noise, in the preprocessing stage in order to avoid complicating the fusion process. In addition, the raw data from each sensor may have to be registered in cases where the data are misaligned with respect to each other, using data registration techniques [26-29]. The preprocessed data are then combined in the data fusion module using an appropriate strategy [15,16,18,30-32]. The fused data can be analyzed and evaluated further to extract relevant information using appropriate classification

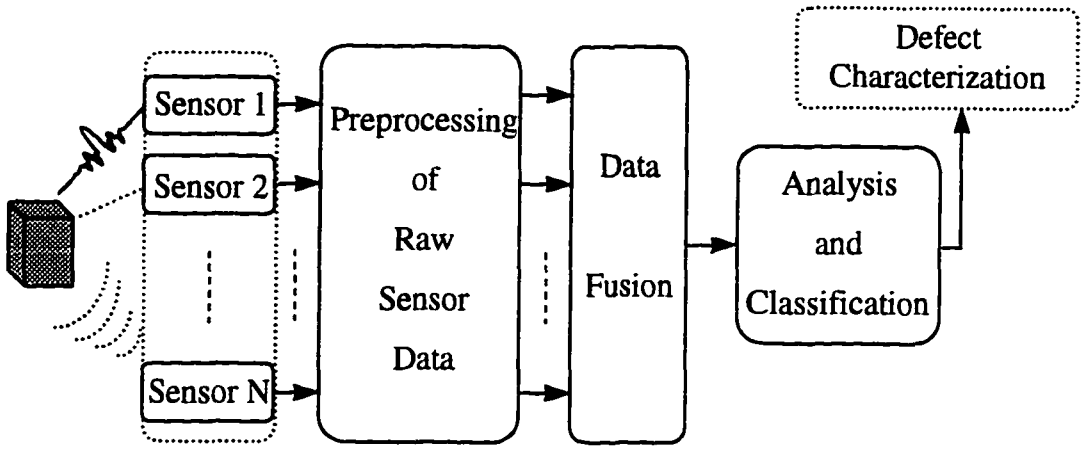

Figure 1.1 Block diagram of a generic NDE data fusion system.

and characterization algorithms [33-39].

Literature Review: NDE Data Fusion Approaches

Several techniques have been proposed in recent years to fuse information properly from a heterogeneous set of NDE sensors. Sun et al. [40,41] use the Q-transform to map the ultrasonic wave field to an equivalent diffusive field. The resulting diffusive field is used to augment information obtained from eddy current NDE measurements. Such techniques, however, tend to be overly sensitive to noise in the measurements. Gros et al. [25] use Dempster-Shafer evidential reasoning [42], which is an extension of the Bayesian inference method, to fuse statistical NDE measurement data. However, this approach requires large amounts of measurement data or a reasonable statistical distribution model of the measurements. Yim et al. [43,44] represent the NDE images using a linear model with additive random noise. A linear minimum mean square error (LMMSE) approach is used to fuse the images. Unfortunately, the method requires accurate estimates of the degradation

kernel and noise statistics. This dissertation employs morphological methods to fuse ultrasonic and eddy current NDE images. Such techniques have been used by Lee [45] to fuse millimeter wave radar images. The technique described in this dissertation is different from that proposed by Lee, in that it employs multiple gray scale residual images to extract features of interest and does not require exact estimates of the size of the structuring element to merge missing features of interest.

Motivation and Objectives

Nondestructive evaluation methods are used very widely to inspect a variety of materials in industry. Each technique offers inspection capabilities and limitations that are dictated by the underlying material/energy interaction process. It can, therefore, be argued that a more comprehensive picture of the condition of the test specimen may be gained by conducting multiple tests and subsequently combining the information gained from these tests. The development of robust data fusion techniques strengthens the case for using "multi-sensor" probes that can be employed for conducting "single-pass" inspections. Such probes can be particularly attractive in situations where access to the specimen is limited or the cost of multiple inspection scans is prohibitively high. Examples of such situations include nuclear steam generator tubing inspection, where the need for reducing exposure to radiation hazards and the desire for containing costs make the concept of a multi-sensor probe attractive. Another example that may benefit from using multi-sensor probes involves the inspection of gas transmission pipelines where the cost of conducting multiple test runs can be excessive.

This dissertation describes a new morphological approach for fusing ultrasonic and eddy

current images. In addition, an efficient morphological algorithm for reducing speckle noise while preserving thin or small features is presented. The algorithm for speckle noise reduction is part of a preprocessing procedure that is employed prior to implementing the data fusion algorithm. The effectiveness of the data fusion approach is demonstrated by solving a problem that is somewhat contrived and perhaps artificial. The problem involves the fusion of eddy current and normal incidence C-scan ultrasonic images. Eddy current NDE images offer a wide spread in gray levels providing information about the depth of the defect. However, the large size of the probe in relation to the width of the flaw results in severe blurring of the defect boundary. In contrast, ultrasonic NDE images obtained by scanning test specimens with thin surface breaking cracks offer excellent resolution, highlighting the edges of the defect. However, it is observed very often in practice that single normal incidence C-scan ultrasonic images tend to provide little information that allows us to infer the depth of narrow cracks. The useful data generated by the two methods can be construed either as complementary or redundant in nature. Ideally it should be possible to utilize the redundant information to improve the signal-to-noise ratio. Likewise, it should be technically possible to fuse the complementary information from the two tests to increase the overall level of information made available to the analyst.

The problem that we seek to solve is contrived for at least two reasons. First, it should be possible to improve the resolution of eddy current images by reducing the footprint of the probe. Second, it should be possible to obtain additional information about the defect including its depth using angle-beam ultrasonics or tomography. Nevertheless, the simplicity of the problem allows demonstration of the basic concept of data fusion very effectively.

In summary this dissertation

- provides an overview of ultrasonic and eddy current NDE test methods.
- describes fundamental morphological operations and their properties.
- presents a new morphological approach for fusing data from ultrasonic and eddy current images.
- discusses a new morphological approach for reducing speckle noise in ultrasonic images.
- demonstrates the validity of the approach using experimentally derived NDE data.

Scope of the Dissertation

This dissertation presents a new morphological data fusion algorithm. This dissertation begins with a brief introduction to ultrasonic and eddy current NDE in chapter 2. Chapter 3 describes some of the basic morphological operators that are employed in the work. Ultrasonic images are often contaminated with speckle noise. The presence of noise complicates the data fusion process. Chapter 4 describes a new morphological algorithm for minimizing speckle noise. The data fusion algorithm is described in chapter 5. The effectiveness of the proposed data fusion approach as well as the speckle noise filtering algorithm is presented in chapter 6. Chapter 7 is devoted to a discussion on a comparison of the performance of the algorithm relative to classical approaches. A summary of the work described in this dissertation as well as areas of future work are given in chapter 8.

CHAPTER 2 FUNDAMENTALS OF ULTRASONIC AND EDDY CURRENT TEST METHODS

This chapter presents a brief overview of ultrasonic and eddy current NDE test methods. The capabilities and limitations of each test method are also illustrated and discussed using experimentally derived normal incidence C-scan ultrasonic and eddy current images.

Ultrasonic Test Methods

Ultrasonic waves are mechanical vibrations generated above the human hearing frequency range (typically from 10Hz to 20KHz). Acoustic waves whose frequencies are above 20KHz are called ultrasonic waves [4]. In practice, the frequency range normally employed in ultrasonic NDE lies between 100KHz to 1GHz [46]. Ultrasonic NDE test methods utilize ultrasonic wave propagation in materials to ascertain the condition of the test specimen [4].

Figure 2.1 illustrates a typical experimental configuration for conducting an ultrasonic test. The ultrasonic pulser/receiver shown in Figure 2.1 generates an electrical pulse which is applied to an ultrasonic transducer that is coupled to the specimen under test. The ultrasonic wave is scattered within the specimen by defects and inhomogeneities. The scattered ultrasonic signal is observed through a receiver transducer which converts the ultrasonic signal to an electrical signal. The electrical signal is sampled, quantized and suitably encoded (A/D conversion) for further processing as shown in Figure 2.1.

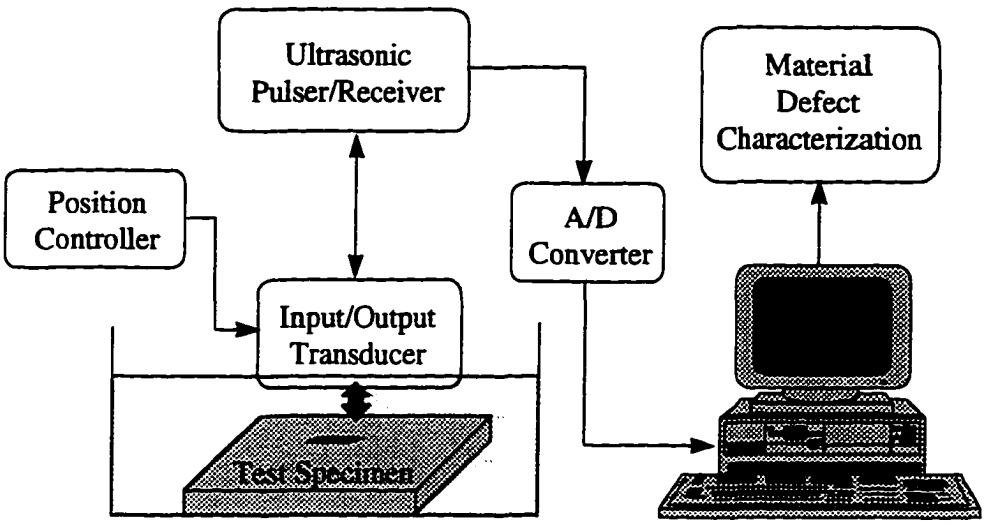

Figure 2.1. Block diagram of a typical ultrasonic test system.

When a transducer plays the role of both transmitter and receiver, the experimental setup is said to be configured in a pulse-echo mode as shown in Figure 2.2(a). When two separate transducers are used for transmitting and receiving the signal, the experimental setup is said to be configured in a pitch-catch mode as shown in Figure 2.2(b).

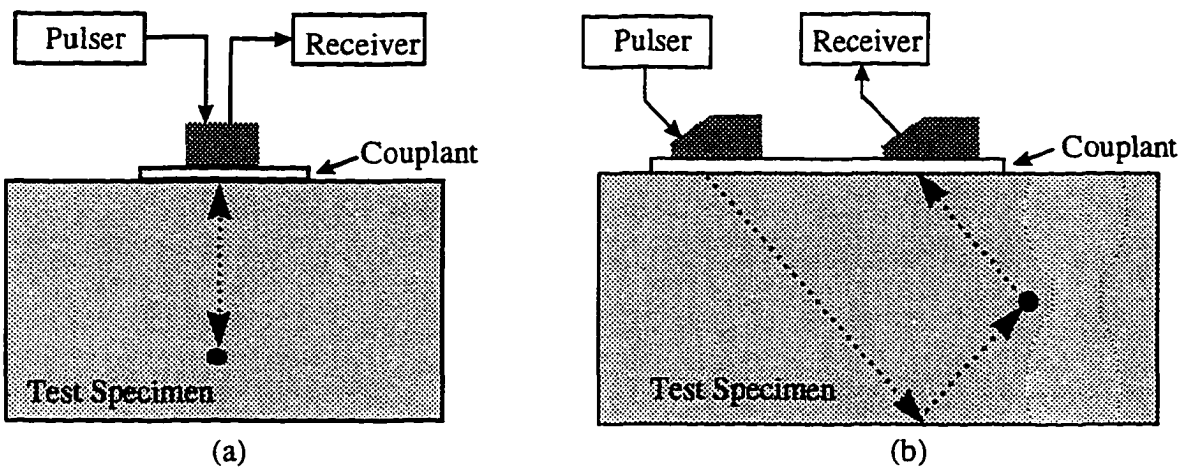

Figure 2.2. Pulse-echo and pitch-catch modes of inspection.

Ultrasonic transducers can be classified depending on the physical phenomenon that is exploited for energy conversion. Examples of transducers include piezoelectric, electromagnetic and magnetostrictive types [47]. The piezoelectric transducer, which is used widely in ultrasonic NDE applications, exploits the piezoelectric effect. This effect is observed in crystals such as quartz, tourmaline, lithium, sulphate, cadmium, sulphide and zinc oxide [47]. If an electrical alternating voltage is applied to a crystal such as a quartz slab, compression and shear waves are generated depending on the manner in which the facets of the crystal are cut.

When ultrasonic waves travel through the material, they cause vibration or displacement of the particles in the material. Many types of ultrasonic waves exist, depending on the manner in which particles vibrate relative to the direction of the ultrasonic propagation: longitudinal, transverse, surface and so on. If the particle motion is in the same direction as the propagation of the wave, it is called a longitudinal, compressional, dilational or irrotational wave. The transverse, shear or distortional wave is a wave motion in which the particle displacement is at right angles to the direction of wave propagation [47-50]. In contrast to longitudinal and transverse waves which travel in a bulk material, the surface waves propagate over or near the surface of materials. There are three types of surface waves: Rayleigh, Love and Stoneley waves [51-52]. If the thickness of surface waves is large compared to the wavelength of the wave, it is called a Rayleigh wave. The propagation velocities of Rayleigh waves are less than those of bulk waves. When a plate borders on one side on a material of different density, Love waves travel on the surface layer. The velocities of Love waves are dependent on frequency. The velocity decreases with increasing frequency. Waves which can be propagated along the

interface of the two materials differing in elastic properties and density are called Stoneley waves [2].

Depending on the direction of the traveling ultrasonic wave at the interface of the transducer, two types of transducers can be considered: normal beam and angle beam transducers. In reality, there are many cases where the use of a normal beam transducer may not provide adequate information. This is particularly true when it is difficult to gain access to the specimen fully or if the defect is located at an awkward place and orientation. As an example, angle beam transducers are used widely for detecting vertical planar cracks in pipe welds [53].

The energy from the transducer is coupled to the test specimen through a couplant. The reason underlying the need for using a couplant can best be understood through a physical acoustic property parameter called the acoustic characteristic impedance. The acoustic characteristic impedance which is analogous to electrical impedance is defined as [47]

$$Z = \rho \upsilon \tag{2.1}$$

where ρ and υ denote the density and the velocity of the material in which the ultrasonic wave travels. Table 2.1 shows longitudinal and shear wave velocities, the density and characteristic impedance for several materials [3]. When the ultrasonic wave is incident on an interface between two media, part of the incident wave energy is transmitted and the rest is reflected. The parameters that indicate the efficiencies of transmission and reflection of the wave are defined as

$$\begin{aligned} \textit{Transmission Coefficient } TC &= \frac{\textit{Intensity of transmitted waves at the boundary}}{\textit{Intensity of incident waves at the boundary}} \\ \textit{Reflection Coefficient } RC &= \frac{\textit{Intensity of reflected waves at the boundary}}{\textit{Intensity of incident waves at the boundary}} \end{aligned} \tag{2.2}$$

The transmission and reflection coefficients defined in (2.2) can be represented using the characteristic impedance defined in (2.1) as [54]

$$TC = \frac{4Z_1Z_2}{(Z_1+Z_2)^2}\ ,\ RC = \frac{(Z_1-Z_2)^2}{(Z_1+Z_2)^2} \tag{2.3}$$

where Z_1 and Z_2 denote the characteristic impedances of two materials. If the acoustic physical properties of the two interfaced materials are vastly different from each other, the transmission coefficient approaches zero. As an example, in the case of a quartz piezoelectric ultrasonic transducer and an air coupling medium, the transmission coefficient obtained by substituting the values in Table 2.1 into (2.3) is 8.68×10^{-5} which corresponds to -81 dB. Hence, the energy generated from the transducer cannot be coupled effectively to the specimen under test. If a coupling material that is similar to the transducer is used, the transmission efficiency rises to almost 100 %. However, if we use aluminum as a coupling medium for the quartz ultrasonic transducer, problems associated with machining an aluminum sample with a sufficiently smooth surface without any air gaps between the transducer and coupling medium become formidable. To overcome the impedance mismatch problem, a liquid coupling material such as water or lubricating oil is used. If we use water as a coupling medium, the transmission coefficient amounts to 0.32522 (32.5 %), which corresponds to -9.76 dB.

The received signal obtained from the ultrasonic transducer is converted to digital data using an A/D converter in order to store and process the information using digital signal

Table 2.1. Acoustic properties of materials.

Material	Longitudinal velocity υ_L*	Shear velocity υ_S*	Density ρ*	Characteristic Impedance $\rho\upsilon_L$*
Aluminum(2SO)	6.35	3.10	2.71	1.72
Copper	4.66	2.26	8.9	4.18
Iron	5.90	3.23	7.9	4.54
Steel	5.85	3.23	7.8	4.56
Stainless Steel(302)	5.66	3.12	8.03	4.55
Quartz (natural)	5.73	-	2.65	1.52
Water	1.49	-	1.00	0.149
Air	0.33	-	0.001	0.000033

* Unit: (υ_L, υ_S: m s^{-1} x 10^3), (ρ: kg m^{-3} x 10^3) and ($\rho\upsilon_L$: kg $m^{-2}s^{-1}$ x 10^7)

processing techniques.

In general, ultrasonic NDE signals or images are classified into three categories depending on the manner in which data is displayed: A-scan signal, B- and C-scan images. The A-scan signal is obtained by fixing the ultrasonic transducer position over the surface of a test specimen and plotting the transducer response as a function of time. The B-scan image is obtained by moving the ultrasonic transducer linearly over the surface of a specimen under test and placing the A-scans next to each other to obtain an image. Hence the B-scan image provides an indication of the cross section of the specimen under test [53]. In contrast to the A-scan signal and the B-scan image, the C-scan image involves the inspection of a specific volume of the material under test. The C-scan image is obtained by scanning the specimen in a

two dimensional grid and representing the peak value at each point in the grid in the form of a gray level to obtain a two dimensional image. The depths of defects correspond to the gray levels in the C-scan image. This dissertation focuses on methods for processing the C-scan image. Figures 2.3(c) and (d) illustrate examples of normal incidence ultrasonic C-scan images which were obtained from specimens shown in Figure 2.3(a) and (b) using a 60 MHz focused ultrasonic transducer and scan step size of 40 μm. The image size is 256 x 256 pixels. The scan area of the sample corresponds to 10.24 x 10.24 mm. As shown in Figure 2.3(c) and (d) the C-scan ultrasonic images offer excellent resolution, highlighting the edges of thin surface breaking cracks. However, it is apparent that the image does not provide sufficient information that allows us to infer the depth of the line-type surface crack. In addition, the C-scan ultrasonic images are contaminated with speckle noise as well as noise from the measurement system [55].

Eddy Current Test Methods

Eddy current test methods [56-59] rely on the interaction between alternating electromagnetic fields and conductive materials under test. When a coil is excited by an alternating current, a time varying magnetic field is generated. If the probe is moved close to the nonferromagnetic but conductive material under test, the time varying magnetic field induces a current in the conductive material. The induced current is called an eddy current since its shape is similar to a circulatory loop. The induced eddy current in turn generates a magnetic field whose direction is opposite to that of the field established by the coil in accordance with Lenz's law. Consequently the net flux linkages associated with the

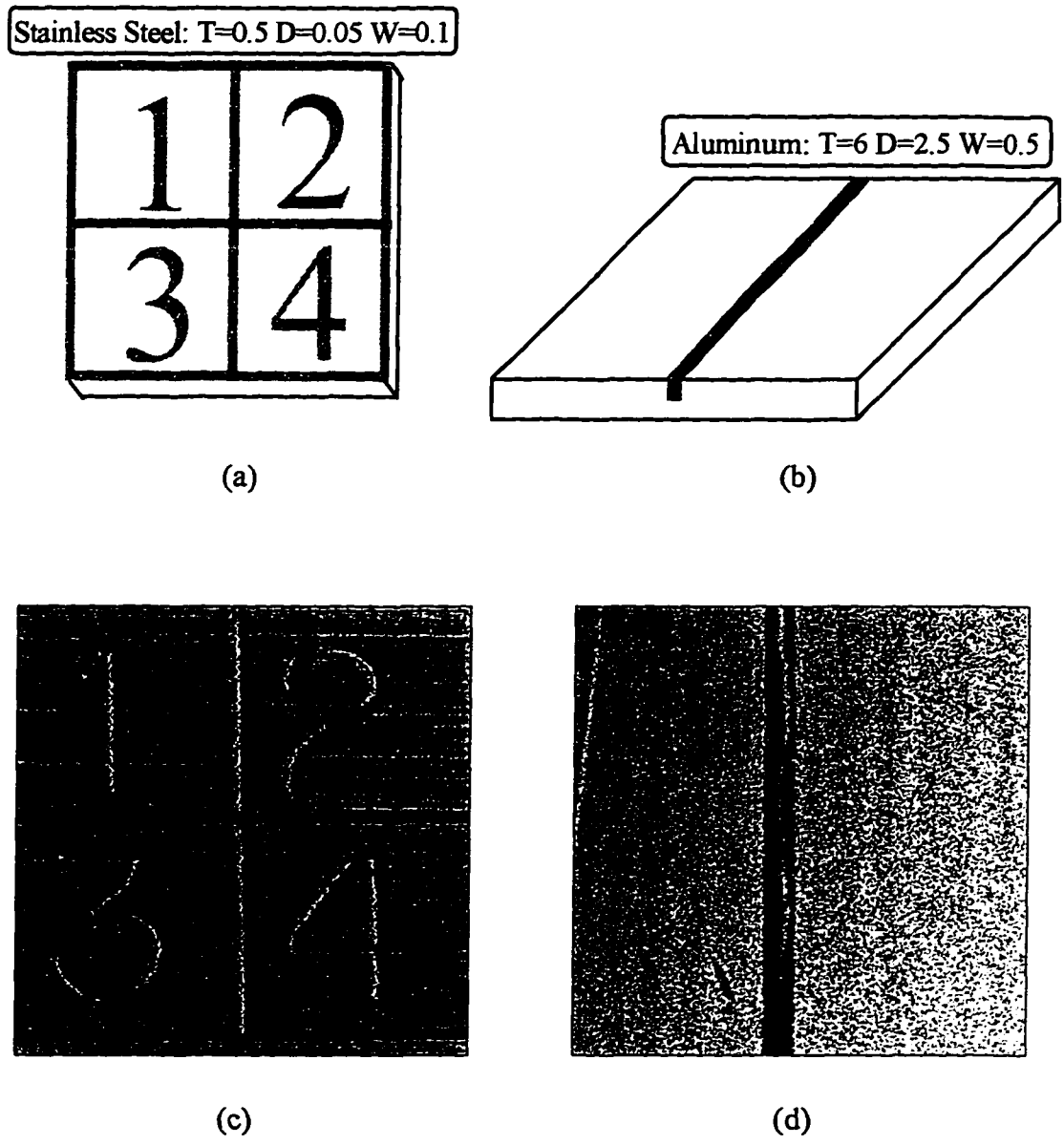

Figure 2.2. Examples of C-scan ultrasonic images. (a) and (b) show specimen details. (c) and (d) show the corresponding C-scan ultrasonic images.

excitation coil are decreased. Since the inductance of the probe is defined as the flux linkages per unit ampere, a net reduction in the probe inductance is observed. In addition, the presence of eddy currents in the material results in a resistive power loss. This results in a net increase in the terminal resistance of the probe. If anomalies or inhomogeneities exist near the surface of the material under test, the eddy current distribution and hence the terminal impedance changes. The changes in impedance of the coil can be monitored to ascertain the condition of the test specimen. An eddy current image is obtained by scanning the test specimen and transforming the magnitude of the impedance measured at each point in the two dimensional scan to a gray level. A number of other issues affect ultrasonic and eddy current measurements. In the case of eddy current methods, issues such as lift-off, choice of excitation frequency and probe design affect the quality of measurements. A detailed discussion of these issues is given in [60].

Figure 2.4 illustrates examples of eddy current NDE images obtained from specimens shown in Figures 2.3(a) and (b). The images were obtained using a Zetec© pencil-type probe (50KHz - 500KHz) with the excitation frequency set at 200KHz and scan step size of 40 μm. Each image shown in Figure 2.4 is of size 256 x 256 pixels. The eddy current image shown in Figure 2.4(a) shows severe blurring of the machined numerals on the surface in contrast to the ultrasonic C-scan image shown in Figure 2.3(c). However, the eddy current image shown in Figure 2.4(b) offers a wide spread in gray levels providing information about the depth of line-type surface crack. Hence, eddy current and ultrasonic NDE images can be construed as providing some complementary information.

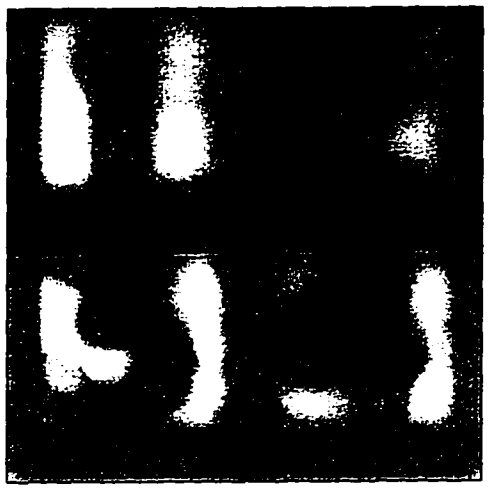

(a)

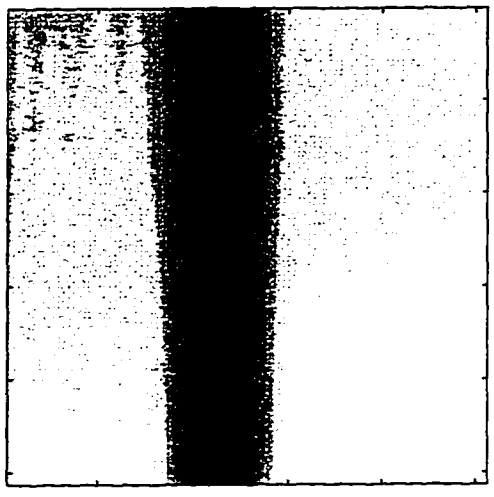

(b)

Figure 2.4. Examples of eddy current images.

CHAPTER 3 MORPHOLOGY IN IMAGE PROCESSING

This chapter provides definitions and describes the algebraic properties of morphological operators employed in binary and gray scale image processing. These include erosion, dilation, opening and closing operators. Simulation results obtained using binary and gray scale morphological operations from several images are illustrated and discussed. The capabilities and limitations of morphological noise reduction filters are demonstrated using an experimentally derived ultrasonic NDE image.

Binary Morphology in Image Processing

The term morphology, in biology, refers to the field of study of forms and structures of plants and animals. In image processing, however, the term is not used so generically. The scope of morphological methods is as wide as image processing itself [61]. Mathematical morphology in image processing was developed initially by G. Matheron and J. Serra to extract and analyze geometrical structures contained in images using set-theoretical operations [62-64]. The morphological approach to image processing is based on a primitive microstructure called a structuring element. The fundamental strategy employed in morphological image processing is to seek set-theoretical relationships between the given images and the predetermined structuring element by scanning the image using the structuring element [65]. All morphological operations depend on the concept of fitting structuring elements. Morphological methods were initially applied to binary (black and white) images. The concept was extended to analyze gray scale images in [66].

Mathematical definitions

We begin by defining the basic binary morphological operations for erosion (E), dilation (D), opening (O) and closing (C) as follows [61,65]:

$$\text{Erosion}: \quad E(B,S) = \bigcap\{B - s \mid s \in S\} \tag{3.1}$$

$$\text{Dilation}: \quad D(B,S) = \bigcup\{B + s \mid s \in S\} \tag{3.2}$$

$$\text{Opening}: \quad O(B,S) = D\{E(B,S),S\} \tag{3.3}$$

$$\text{Closing}: \quad C(B,S) = E\{D(B,S),S\} \tag{3.4}$$

where B is the given binary image and S is a predetermined microstructure image, called the structuring element in a two dimensional discrete Euclidean plane. Since we are interested in pixels of value 1 in binary images, a pixel of value 1 is called an activated pixel. The domain of B or S consists of activated pixel locations in the plane. The minus or plus sign in set parentheses denotes vector subtraction or addition, respectively. That is, these operations perform an image translation in the plane. As we know from (3.1) to (3.4), the basic operations are composed of set intersection, union and translations in a given domain. The erosion and dilation operations can be defined in an alternative form as [61,65]:

$$E(B,S) = \{v : S + v \subset B\} \tag{3.5}$$

$$D(B,S) = \{v : (-S + v) \cap B \neq \varnothing\} \tag{3.6}$$

where v is a coordinate vector in the plane which denotes the translation quantity in the plane. The results of (3.5) and (3.6) are exactly the same as those of (3.1) and (3.2), respectively. However, the definitions of (3.5) and (3.6) are very useful for understanding the operations of erosion and dilation. In (3.5), the output of the erosion operation is obtained by translating a structuring element and checking whether the structuring element can fit inside a given object

in an image. If the translated structuring element can be included inside the object, the translated quantity is said to be a subset of the erosion output. In (3.6), the output of dilation operation is also obtained by translating the 180° rotated structuring element (-S) and checking if the intersection of that with the given object is a null set or otherwise. If the 180° rotated and translated structuring element intersects with the object, the translated quantity is a subset of the dilation output. Similarly the opening and closing operations can be defined in an alternative form as

$$O(B,S) = \cup\{S+v : S+v \subset B\} \tag{3.7}$$

$$C(B,S) = [O(B^C,S)]^C \tag{3.8}$$

where the superscript c denotes a set complementary operation. In (3.7), the output of the opening operation is obtained by translating the structuring element and checking if the translated structuring element is a subset of the image domain. If the translated structuring element is inside the activated object domain, the union of the set containing the translated structuring element itself becomes the output of the opening operation. Similarly in (3.8), the output of a closing operation is obtained by complementing the output after performing an opening operation using the complemented image and the structuring element. It should be mentioned that while the opening operation is performed to assess the fitness of the structuring element inside the activated object domain, the closing operation involves looking for the fitness of the structuring element outside the activated object domain [67]. Although (3.5) to (3.8) are very useful to understand these operations, practical implementations of these operations are achieved using (3.1) to (3.4). In hardware, the union, intersection and translation operations can be simply implemented using OR, AND gates and shift registers,

respectively. In software, these operations are simply programmed using maximum, minimum and vector addition/subtraction functions, respectively. Based on the mathematical definitions of (3.1) through (3.4) and the understanding of morphological operations using (3.5) through (3.8), we can establish some of the more important algebraic properties of the morphological operations.

Algebraic properties

An understanding of the algebraic properties of fundamental morphological operations is important for implementing the operations in image processing applications efficiently. Some of the important algebraic properties of the operations are [61,65]:

Commutativity: $$D(B,S) = D(S,B) \tag{3.9}$$

Associativity: $$E[B,D(S_1,S_2)] = E[E(B,S_1),S_2] \tag{3.10}$$

$$D[B,D(S_1,S_2)] = D[D(B,S_1),S_2] \tag{3.11}$$

Duality: $$E(B,S) = [D(B^c,-S)]^c \tag{3.12}$$

$$D(B,S) = [E(B^c,-S)]^c \tag{3.13}$$

where $-S$ denotes the reflection of S through the origin. The properties of the operations with respect to translation are:

$$D[B,(S+v)] = D(B,S)+v \tag{3.14}$$

$$E[B,(S+v)] = E(B,S)-v \tag{3.15}$$

In general, the structuring element can be decomposed into a set of smaller sizes as shown by Serra [68,69,76]. Assume that the structuring element can be decomposed as

$$S = S_1 \oplus S_2 \oplus \ldots\ldots S_{N-1} \oplus S_N \tag{3.16}$$

where $\oplus$ denotes the dilation operation. Using the associativity property of erosion or dilation operation, the theorem shown in (3.16) can be implemented using an iterative technique by employing consecutive erosion or dilation operations with a sequence of smaller structuring elements instead of a single large structuring element. This property can reduce the computational load significantly. Since the erosion or dilation operation is composed of translations and intersections or unions, we can minimize the computational burden by decomposing the operation. Figure 3.1 shows the decomposition of a structuring element of size 5 x 5 into two structuring elements of each size 3 x 3. In Figure 3.1, the star mark denotes the origin in the discrete Euclidian space. If we erode or dilate an image using a 5x5 structuring element as shown in Figure 3.1(a), the total number of image set translations amounts to 24 (=25-1). However, if we erode or dilate an image iteratively using the decomposed structuring elements as shown Figure 3.1(b), the total number of image set translations is reduced to 16 (=(9-1)x2). The size of the eroded or dilated image is decreased or increased by 2 pixels along the X and Y directions.

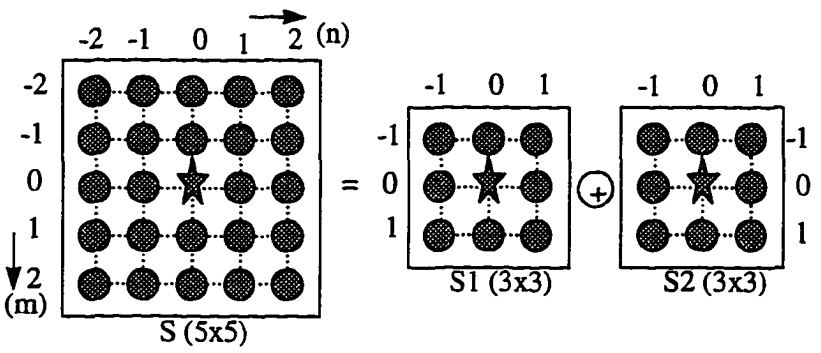

Figure 3.1 Example of structuring element decomposition.

In reality, the size of the structuring element is negligibly small in comparison with the image. Hence the computational load can be estimated approximately using the given image size and the total number of activated structuring element pixels. In the case of opening or closing operation, the dilation or erosion operation is followed by an erosion or dilation operation, respectively and consequently the final image size does not change. In employing the structuring element decomposition as shown in Figure 3.1, the relative computational load can be reduced by (24 - 16) / 24 x 100 = 33 (%). It can be shown that if we decompose a structuring element (N x N pixels) into n structuring elements of size M x M pixels, the relative computational load can be reduced *by* $(N \times N - n \times M \times M) / (N \times N) \times 100$ *(%).* Thus a structuring element decomposition strategy that exploits the associative property is very useful in fast implementation of morphological operations. The structuring element decomposition property is also valid in the case of gray scale morphology. The morphological algorithm, described in chapter 4, uses the structuring element decomposition concept.

Morphological filters

This section describes how morphological operations can be viewed as filters in binary image processing. Morphological filters can also be extended to gray scale images [63,64]. The relationship between morphological and linear filters is described in detail in [70]. In a broad sense, filtering is a transformation or mapping from one vector space to another vector space. If we assume $B_1 \subset B_2$ and define a mapping function $\Theta : 2^{R \times R} \rightarrow 2^{R \times R}$, where R and $2^{R \times R}$ denote real number and the set of all subsets of R x R, and $\Theta(B_1) \subset \Theta(B_2)$ for $B_1 \subset B_2$, then Θ is called an increasing mapping. If $\Theta(B + v) = \Theta(B) + v$ for any subset B of R x R and

coordinate point or vector v, Θ is called translation invariant or τ–mapping. In mathematical morphology, the morphological filter is defined as increasing and τ–mapping [67]. One of the important properties of morphological filters is the fact that the combination of morphological filters represents increasing τ–mapping since it preserves the set-theoretical ordering and is space translation invariant [67]. The fundamental morphological operations, erosion, dilation, opening and closing and their combinations satisfy increasing and τ–mapping criteria. Thus they can also be said to be morphological filters.

Digital images can be commonly represented through matrix forms. In contrast to common linear algebra matrices, image matrices contain the origin of the image. Thus they are called bound matrices [67,71]. The origin of an image and structuring element affects the outputs of morphological operations. Thus the definition of the origin is important in morphological image processing. Figures 3.2 to 3.5(a) through (e) show the original image, the outputs of erosion, dilation, opening and closing operations (or morphological filters), respectively, for different types of images and structuring elements. Figures 3.2 and 3.3(b) through (e) show the outputs of morphological filters for a binary image using disk-type symmetric and line-type non-symmetric structuring elements, respectively. As shown in Figures 3.2(c) and (d), the corners of dilated and opened images become rounded due to the nature of dilation, opening operations and the shape of the structuring element. These results are similar to those obtained with lowpass filters. From the results shown in Figures 3.2 and 3.3 for the same given image, we know that the morphological filter outputs also depend both on the structuring element as well as the morphological operations. In Figures 3.4 and 3.5, the dents and protrusions at the top and bottom edges of image B shown in Figures 3.4 and 3.5(a)

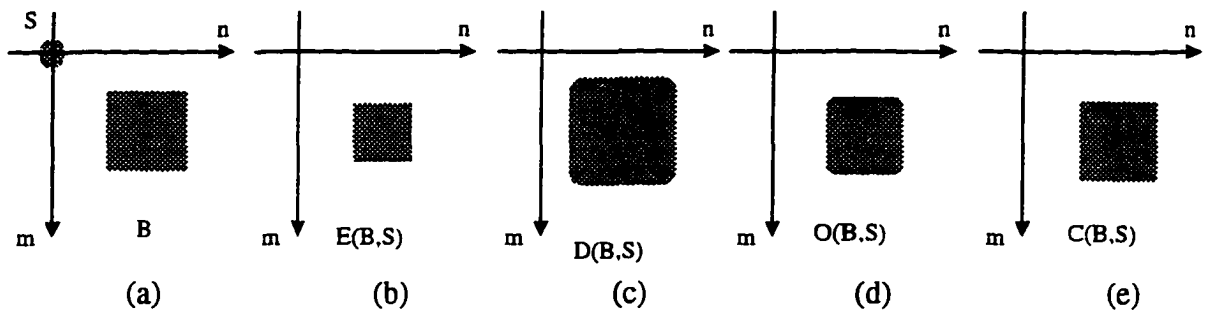

Figure 3.2. Binary morphological outputs obtained from a square-type binary image using a disk-type symmetric structuring element.

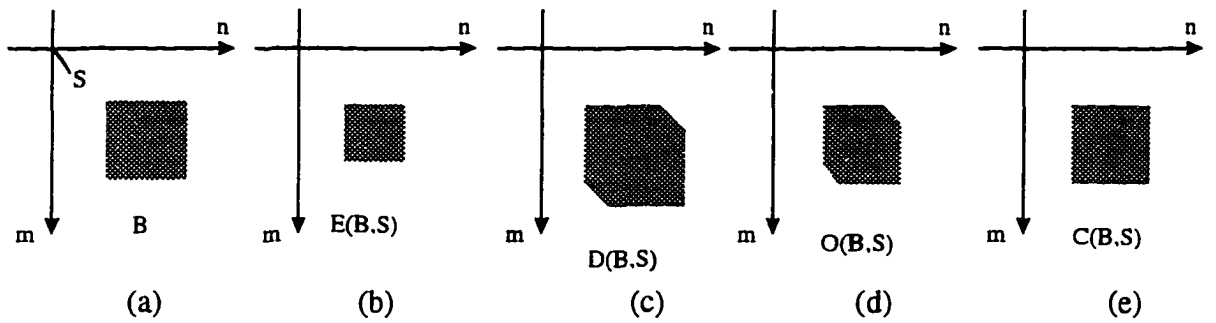

Figure 3.3. Binary morphological outputs obtained from a square-type binary image using a line-type non-symmetric structuring element.

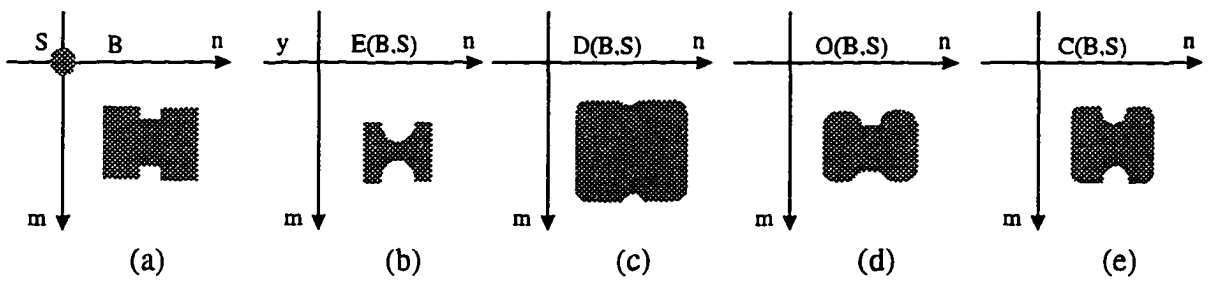

Figure 3.4. Binary morphological outputs obtained from a dented square-type binary image using a disk-type symmetric structuring element.

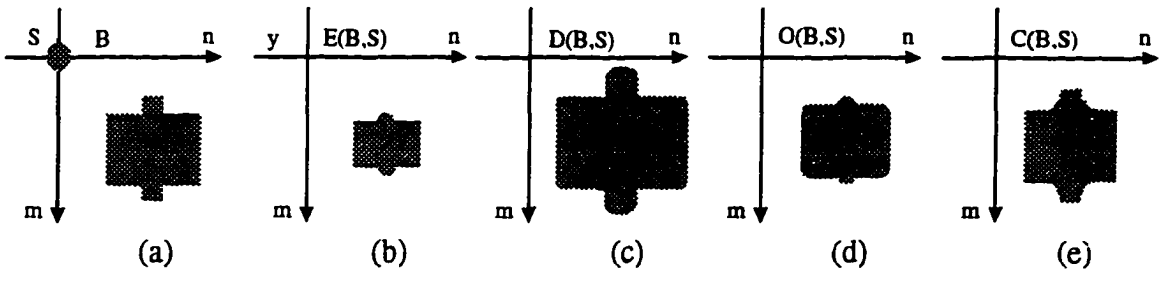

Figure 3.5. Binary morphological outputs obtained from a protruding square-type binary image using a disk-type symmetric structuring element.

can be removed by dilation and closing operations in Figure 3.4 and erosion and opening operations in Figure 3.5. In contrast to conventional linear filters, the morphological filters have the ability to preserve edges without blurring or smoothing them. Also, Figures 3.2 and 3.3 demonstrate that morphological operations are strongly dependent on the shape of the structuring elements. A considerable amount of research on the design of the optimal structuring element is presented in [72-74].

As we know from (3.1) and (3.2), the outputs of erosion and dilation operations depend on the position of the structuring element. However, the outputs of opening and closing operations are not affected by the location of the structuring element. Since the opening and closing operations are a cascade of erosion and dilation operations and vice versa, it is natural that the opening and closing are independent of the position of the structuring element. As shown in Figures 3.2 through 3.5, the erosion and dilation operations shrink or expand the activated binary image domain of white ("0") background and black ("1") objects, respectively. In practical image processing applications, we often do not wish to change the shape of the original object during the filtering process. In such cases the opening and closing

operations or their combinations are more useful than simple erosion or dilation operations since they preserve the object shapes if the structuring element fits into the objects as shown in Figures 3.4 and 3.5. However, significant features can be distorted or removed as a result of the opening and closing operations if the size of the object is smaller than that of the structuring element. A hybrid morphological filter is defined as [75,76]

$$OCCO = \frac{1}{2}[C\{O(B,S),S\} + \{O(B,S),S\}] \tag{3.17}$$

where B and S denote binary input image and structuring element.

The opening and closing operations satisfy the following properties:

Antiextensivity:	$O(B,S) \subset B$	(3.16)
Extensivity:	$C(B,S) \supset B$	(3.17)
Increasing monotonicity:	$O(B_1,S) \subset O(B_2,S)$ *if* $B_1 \subset B_2$	(3.18)
	$C(B_1,S) \subset C(B_2.S)$ *if* $B_1 \subset B_2$	(3.19)
Idempotence:	$O[O(B,S),B] = O(B,S)$	(3.20)
	$C[C(B,S),B] = C(B,S)$	(3.21)

From the property of (3.17), we know that the original image set is a subset of the closed image set. Also, if an image B_1 is a subset of an B_2, then the images obtained by performing closing operations with images B_1 and B_2 preserve the same relation according to property (3.19). These properties are useful, especially in the case of gray scale morphological image processing. These properties are utilized in chapter 4 for multi-resolution image processing using residual images.

Simulation examples

Figure 3.6 shows examples of the binary morphological operations. A square-type symmetric structuring element with size 3x3 pixels is used in the simulation. The image shown in Figure 3.6(a) is obtained by thresholding the original gray scale ultrasonic image. Images (b) through (g) are the corresponding eroded, dilated, opened, closed, open-closed and close-opened binary images, respectively. Since erosion or opening operations are basically "similarity" processes, noise regions that are not similar to the predetermined structuring element are removed as shown in Figures 3.6(b) and (d). However, patterns such as thin features are partially removed together with noise. The outputs of dilation and closing operations show an increase in noise due to the nature of dilation and closing operations. Figure 3.6(g) shows that the closing-opening operation has the potential to reduce noise. However, it distorts line-type objects considerably. Hence, an alternative method for reducing noise in images is required. A technique for accomplishing this is described in chapter 4.

Gray Scale Morphology in Image Processing

We considered the case of binary morphology where the pixels take the values "1" and "0" in the previous sections. In gray scale morphology the pixel values in an image range lie in the 0 to L - 1 where L is an integer representing the number of quantization levels. In practice, $L = 2^n$, where n is the number of bits used in representing the gray scale value. For example, if $n = 8$, the maximum number of gray levels L is 256. Since the binary scale ($n = 1$) is a subset of gray scale, gray scale morphology is a generalization of binary scale morphology. In gray scale morphology the minimum or maximum operator is used in place

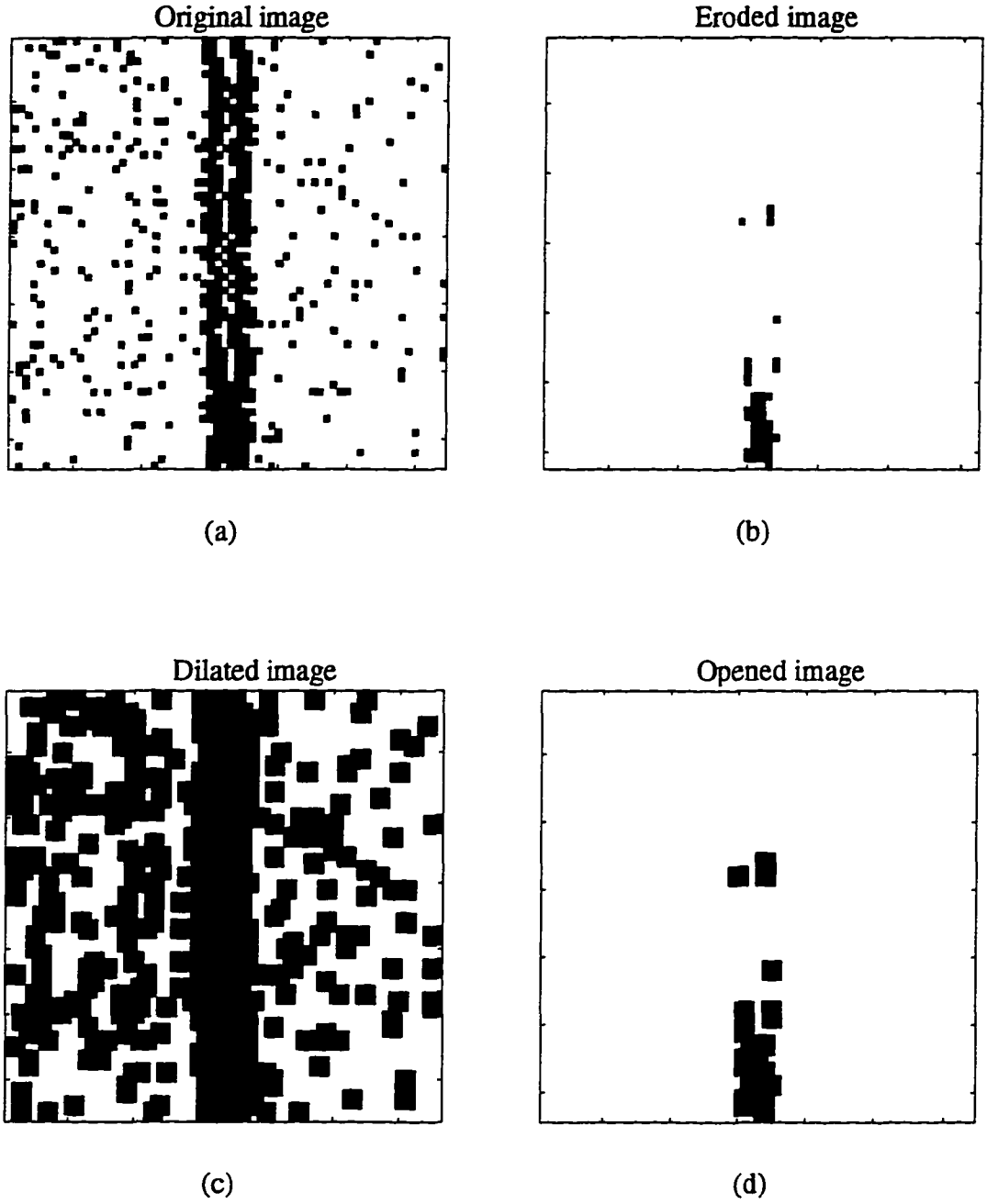

Figure 3.6. Binary morphological outputs obtained from the binary scale ultrasonic image using a square-type symmetric structuring element of size 3 x 3 pixels.

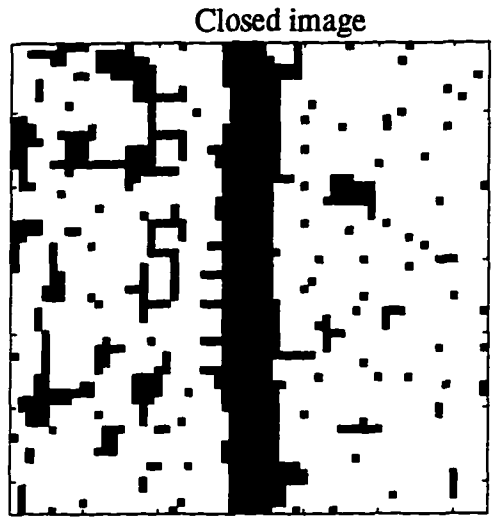

(e)

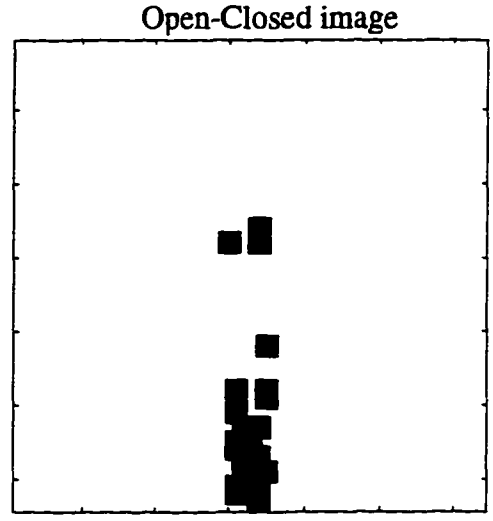

(f)

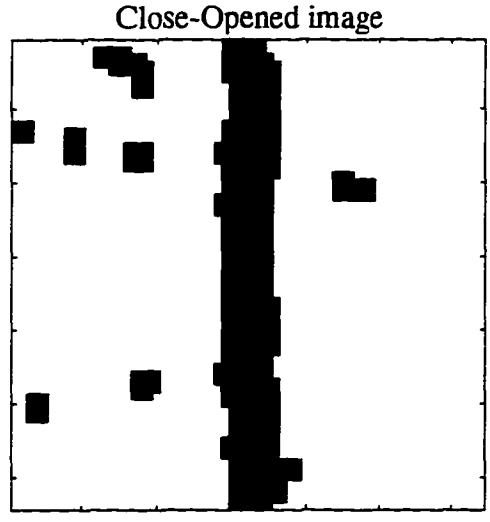

(g)

Figure 3.6. (Continued)

of intersection or union in binary erosion or dilation operation, respectively. Since the pixel values of the structuring element in the gray scale are multi-valued, the subtraction or addition of the gray scale structuring element reflects the shrinkage or expansion of the gray scale range.

Mathematical definitions

We begin by defining the fundamental gray scale morphological operations for erosion (E), dilation (D), opening (O) and closing (C) as follows [61,65]:

$$\text{Erosion: } [E(G,S)](m,n) = \min\{G(m+i,n+j) - S(i,j) \mid (i,j) \in D_S\} \tag{3.22}$$

$$\text{Dilation: } [D(G,S)](m,n) = \max\{G(m-p,n-q) + S(p,q) \mid (p,q) \in D_S\} \tag{3.23}$$

$$\text{Opening: } [O(G,S)](m,n) = D\{E(G,S),S\} \tag{3.24}$$

$$\text{Closing: } [C(G,S)](m,n) = E\{D(G,S),S\} \tag{3.25}$$

where G and S are the image function and the structuring element, respectively and (m,n) denotes the pixel coordinate in the image, and Ds is the domain of S. Substituting (3.22) and (3.23) into (3.24) and (3.25), the closing and opening operators can be expressed as

$$O(G,S)(m,n) = \max[\min\{G(m+i-p,n+j-q) - S(i,j) \mid (i,j) \in D_S\} + S(p,q) \mid (p,q) \in D_S] \tag{3.26}$$

$$C(G,S)(m,n) = \min[\max\{G(m-p+i,n-q+j) + S(p,q) \mid (p,q) \in D_S\} - S(i,j) \mid (i,j) \in D_S] \tag{3.27}$$

As in case of binary morphology, G and S are represented as bound matrices. The primitive operations in gray scale morphology are min (minimum) and max (maximum). If the intersection and union operations of set theory replace min and max operations and the gray

levels in the structuring elements are not subtracted or added in (3.22) and (3.23), the equations of fundamental gray scale morphology are exactly the same as those of fundamental binary morphology.

If the gray levels of a structuring element are all zeros, it is called a flat structuring element [61]. Since it contains only geometrical coordinates, it is used widely if gray levels are desired to be preserved in an overall sense in an image. In simulating binary morphological operations, the intersection and union operations can be implemented using minimum and maximum operations, respectively. Thus if we use a flat structuring element, then programs and algorithms implementing gray scale erosion and dilation operations can be used for performing binary erosion and dilation operations. The simulation results shown in Figure 3.7 were obtained using the same program that was used in simulating the gray scale morphological operations using a flat structuring element.

The gray scale operations can be defined in an alternative manner as [65]:

Erosion: $$E(G,S) = max\{l : S(m-i,n-j)+l \le G\} \tag{3.28}$$

Dilation: $$D(G,S) = -[E(-G,\hat{S})] \tag{3.29}$$

Opening: $$O(G,S) = max\{S(m-i,n-j)+l : S(m-i,n-j)+l \le G\} \tag{3.30}$$

Closing: $$C(G,S) = -O(-G,-S) \tag{3.31}$$

where l denotes the gray level. Although expressions (3.28) through (3.31) are equivalent to (3.22) through (3.25), respectively, they serve to help gain an understanding of the fundamental morphological operations.

Algebraic properties

Basically, the algebraic properties of gray scale morphology correspond to those of binary morphology. The details are explained in [61,63-65]. Some of the important algebraic properties of the gray scale morphology can be summarized as follows:

Commutativity: $$D(G,S) = D(S,G) \tag{3.32}$$

Associativity: $$E[G,D(S_1,S_2)] = E[E(G,S_1),S_2] \tag{3.33}$$

$$D[G,D(S_1,S_2)] = D[D(G,S_1),S_2] \tag{3.34}$$

Duality: $$D(G,S) = -[E(-G,-\hat{S})] \tag{3.35}$$

In (3.35), $-\hat{S}$ denotes a reflected structuring element through the origin. However, this duality property holds only in the domain $E(G,\hat{S})$. Figure 3.7 shows an example of the duality relation between erosion and dilation operations. The translation invariance property of the structuring element in dilation operation is:

$$D[G,\{S(m-i,n-j)+l\}] = [D(G,S)](m-i,n-j)+l \tag{3.36}$$

The property of (3.36) shows the invariance of position and gray level translations. However, in case of erosion operations, the translation invariance of the structuring element in dilation operations is not valid as:

$$E[G,\{S(m-i,n-j)+l\}] = [E(G,S)](m+i,n+j)-l \tag{3.37}$$

The opening and closing operations also satisfy the following fundamental properties:

Antiextensivity: $$O(G,S) \subset G \tag{3.38}$$

Extensivity: $$C(G,S) \supset G \tag{3.39}$$

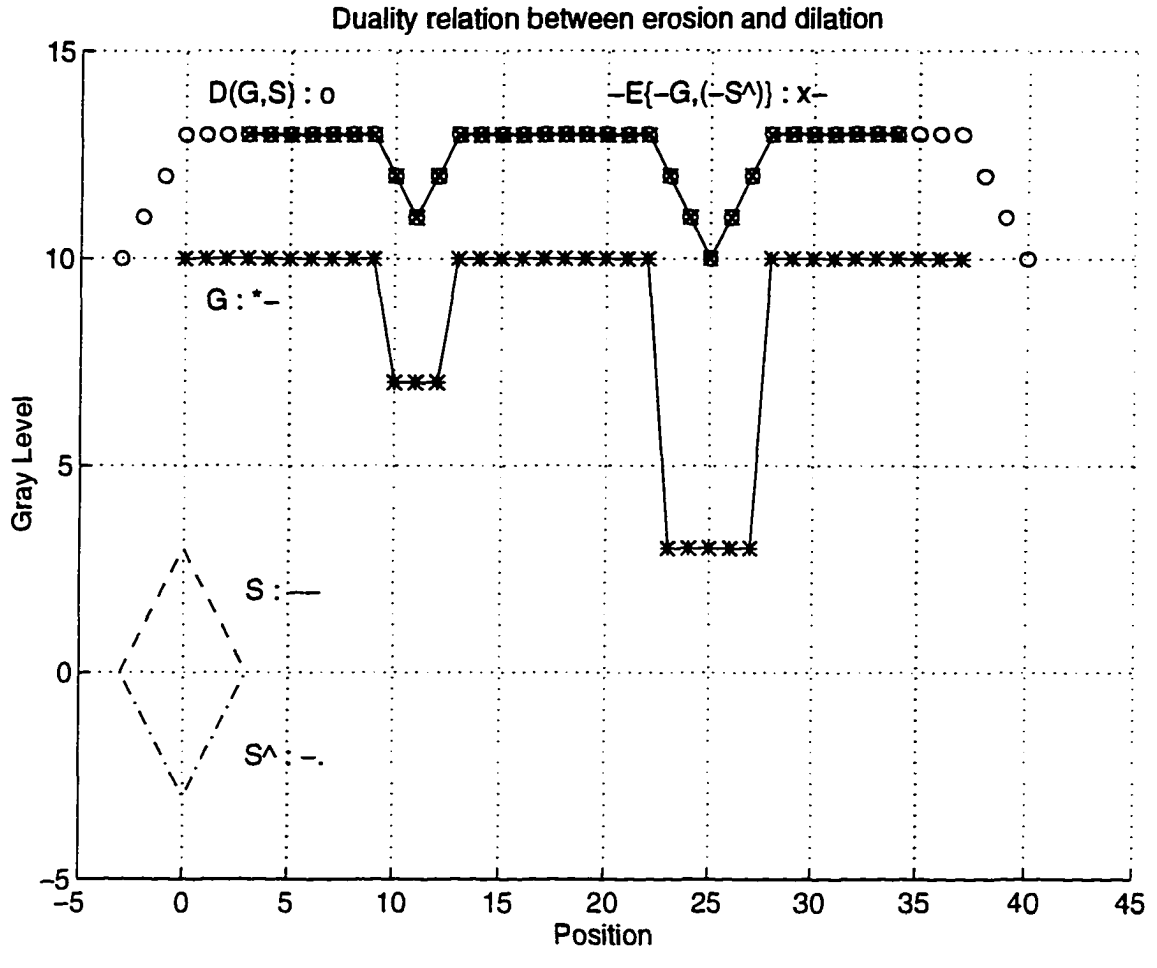

Figure 3.7. Example of duality relation between erosion and dilation operations.

Increasing monotonicity: $O(G_1,S) \subset O(G_2.S)$ *if* $G_1 \subset G_2$ (3.40)

$$C(G_1,S) \subset C(G_2.S) \text{ if } G_1 \subset G_2 \quad (3.41)$$

Idempotence: $$O[O(G,S),B] = O(G,S) \quad (3.42)$$

$$C[C(G,S),B] = C(G,S) \quad (3.43)$$

For structuring elements, while the closing operation is a monotonously increasing property, the opening operation displays monotonously decreasing property, i.e.

$$O(G,S_1) \supset O(G.S_2) \text{ if } S_1 \subset S_2 \tag{3.44}$$

$$C(G,S_1) \subset C(G.S_2) \text{ if } S_1 \subset S_2 \tag{3.45}$$

Simulation examples

Figures 3.8 and 3.9 show simulation examples of the 1-dimensional gray scale morphological operations for two kinds of test signals which contain additive positive and negative impulse-type noise. The original signal, shown in Figure 3.9(a), contains additional noise components relative to those shown in Figure 3.8(a). A symmetric structuring element of length 3 was used in the simulations. As shown in Figures 3.8(b), (d) and (c), (e), erosion, opening and dilation, and closing operations attempt to remove positive and negative peaks which do not fit into the given structuring element, respectively,. Hence, the cascade of opening and closing (open-closing) or closing and opening (close-opening) operations removes both positive and negative peaks in signals as shown in Figures 3.8(f) and (g). As a result, the hybrid morphological filter defined in (3.17) is used widely to remove impulse-type noise in signals and images. Figure 3.8(h) illustrates the output of the hybrid morphological filter. However, if the noise density is high as shown in Figure 3.9(a), the morphological operations and their combinations are inadequate for removing noise effectively. Figures 3.9(b) through (f) show the outputs of erosion, dilation, opening, closing, open-closing, close-opening and hybrid morphological operations, respectively. Although a hybrid morphological filter reduces the magnitude of noise in signals as shown in Figure 3.9(h), it is obvious that its capabilities are limited.

Figures 3.10(a) and (b) show an example gray scale test image of size 6 x 32 pixels and

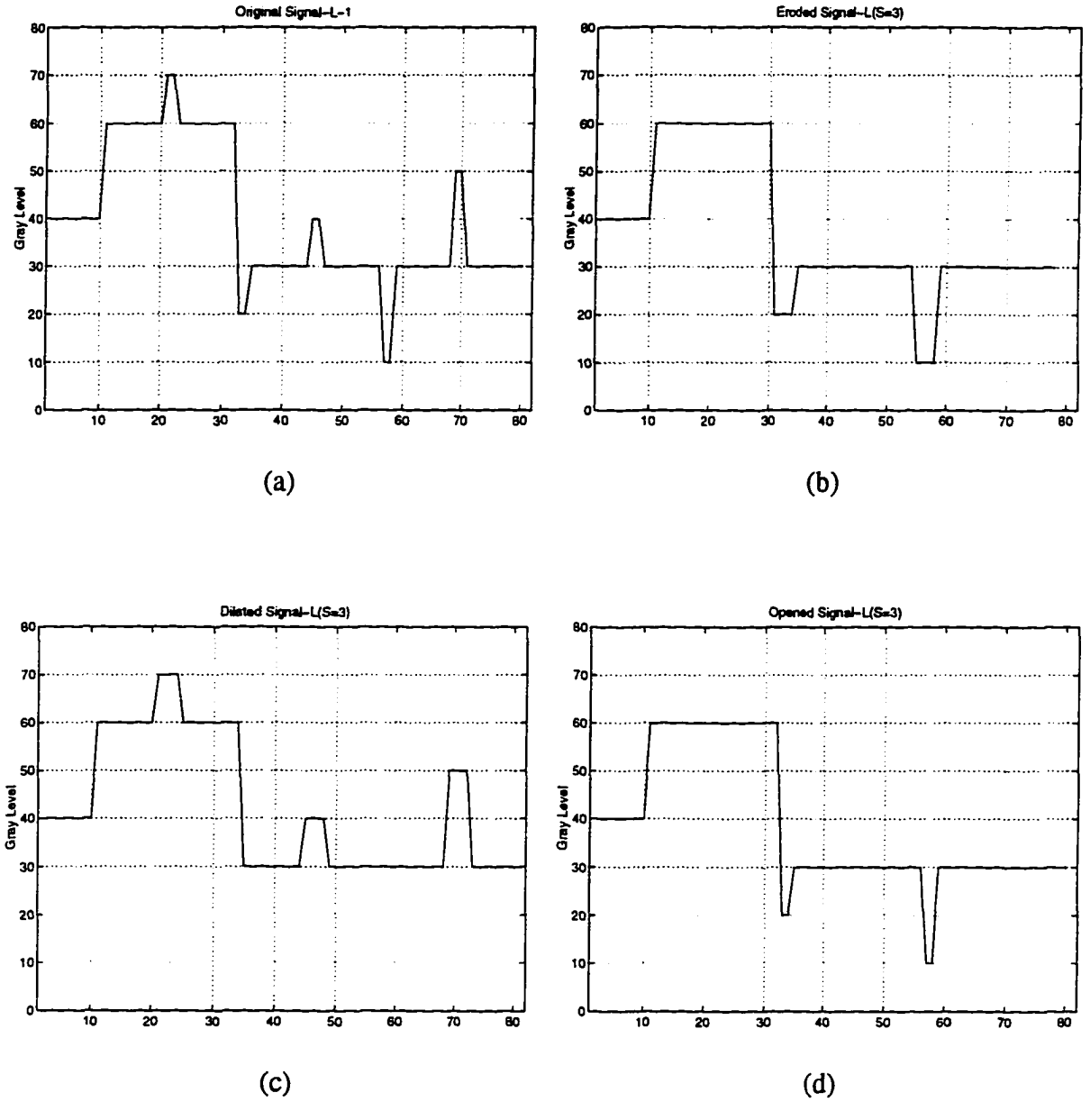

Figure 3.8. Gray scale morphological outputs obtained from a 1-dimensional gray scale signal with low density noise using a symmetric structuring element of length 3.

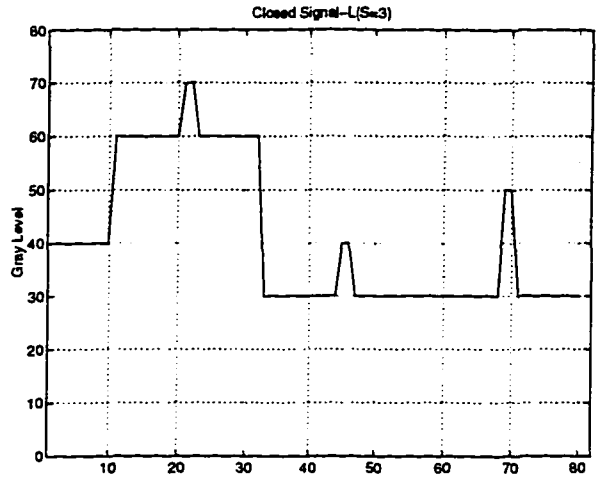

(e)

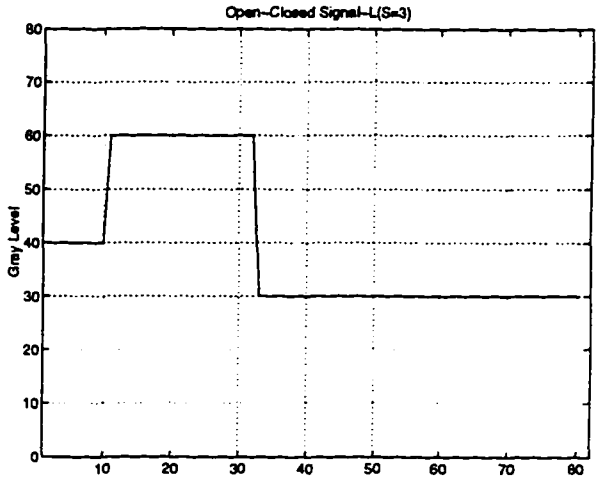

(f)

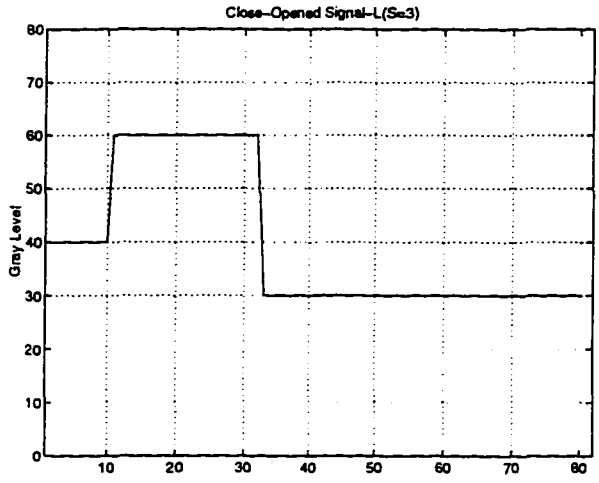

(g)

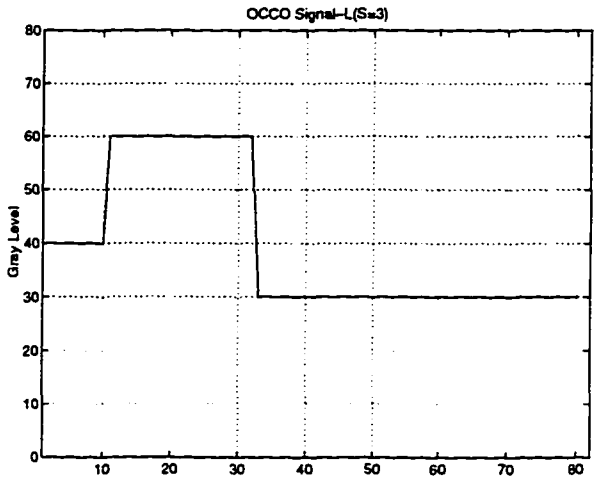

(h)

Figure 3.8. (Continued)

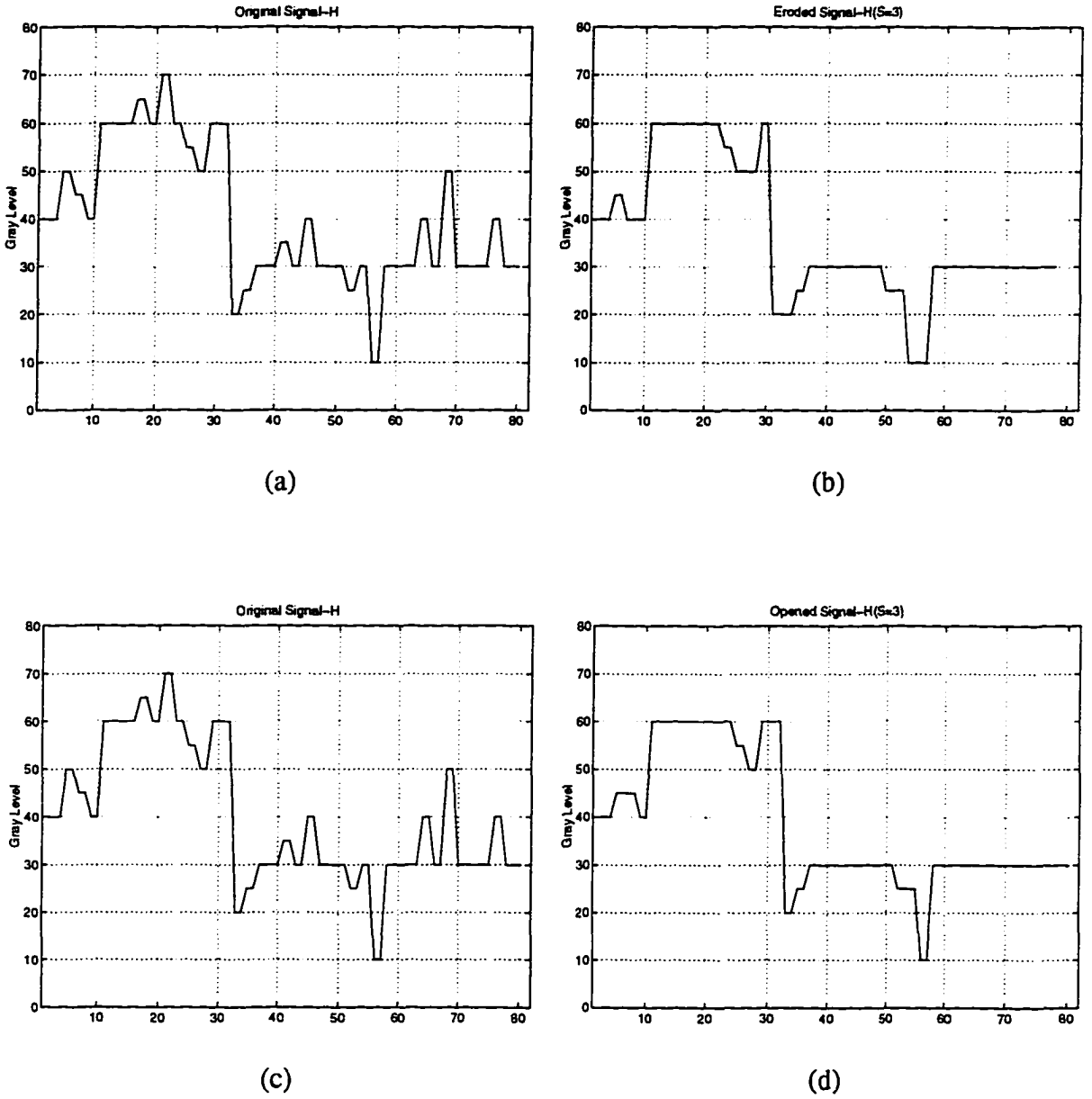

Figure 3.9. Gray scale morphological outputs obtained from a 1-dimensional gray scale signal with high density noise using a symmetric structuring element of length 3.

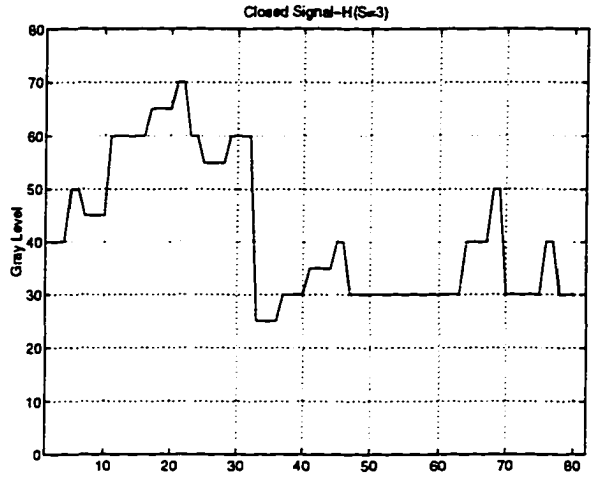

(e)

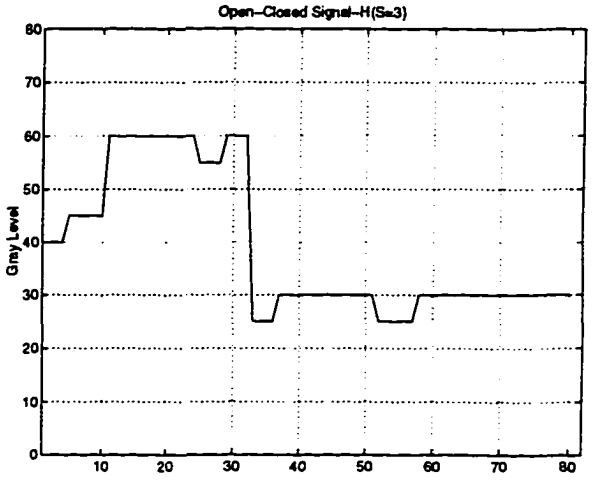

(f)

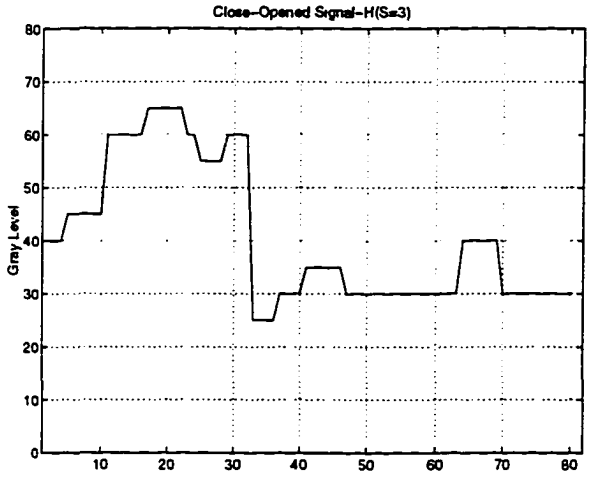

(g)

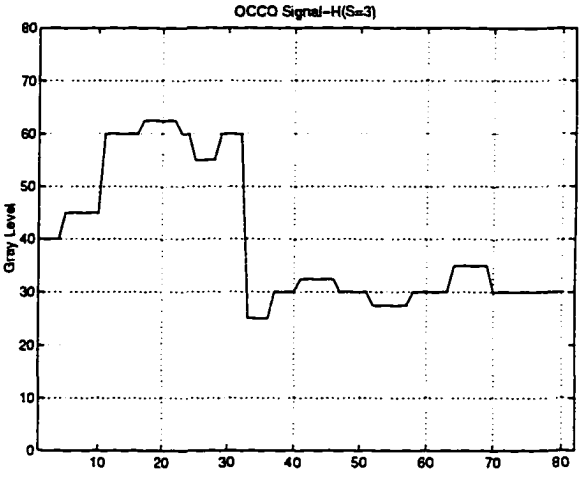

(h)

Figure 3.9. (Continued)

the corresponding line scan which shows finite positive and negative peaks of width 2 and 4 pixels in the horizontal direction (Figure 3.10(b)). Figures 3.11(a) through (h) show fundamental morphological operations obtained using flat symmetric square-type structuring elements of sizes 3 x 3 and 5 x 5 pixels. As shown in Figures 3.11(a) through (d), the erosion and dilation operations are capable of removing positive and negative peaks which do not fit into the predetermined structuring element, respectively. However, the active domains of both regions shrink and enlarge by as much as the size of the structuring elements. Figures 3.11(e) through (h) show that the opening and closing operations are capable of removing positive and negative peak objects that do not fit into the structuring element while preserving the original shape and size of the image. Hence, instead of using simple erosion and dilation operations, opening and closing operations or their combinations are used in morphological image processing. However, opening and closing operations require almost twice the computation effort relative to erosion and dilation operations.

Figure 3.12(a) shows an acoustic microscopy C-scan image obtained using a 60 MHz focused transducer and a scan step size of 40 μm. The image size is 64 x 64 pixels. Figures 3.12(b) through (e) show the corresponding eroded, dilated, opened and closed images obtained by implementing equations (3.22) through (3.25), respectively. Figure 3.12(f) shows the output of a hybrid morphological filter represented by (3.17). A flat symmetric square-type structuring element of size 3 x3 pixels was used in the simulation.

The dilation and closing operations reduce the speckle noise in the background as shown in Figures 3.12(c) and (e). It is apparent that thin features such as those due to cracks may be eliminated from the images by using these operations. Although erosion and opening

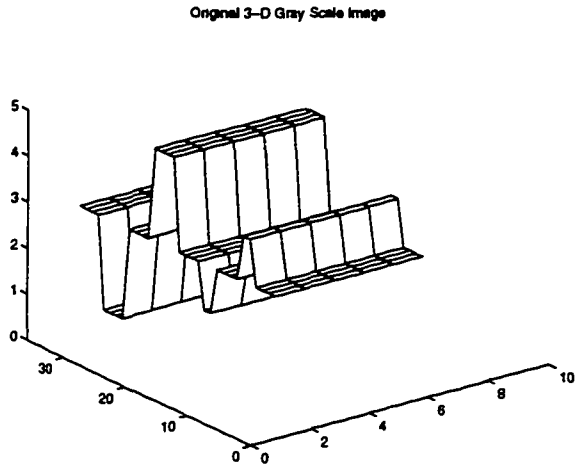

(a)

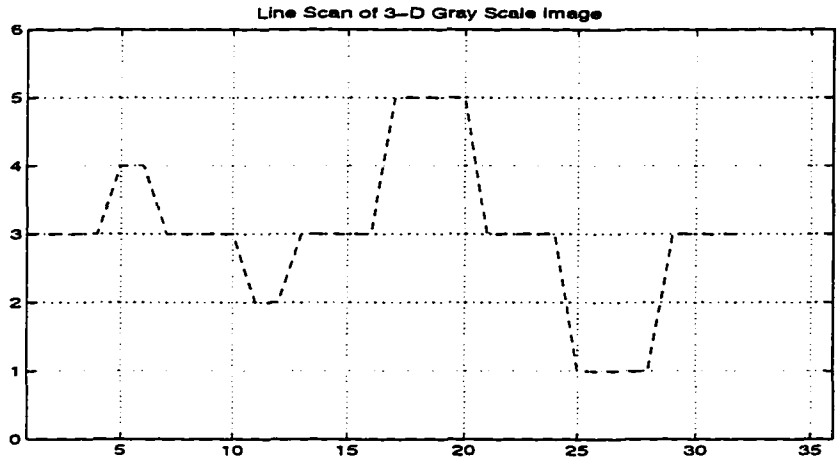

(b)

Figure 3.10. Gray scale image containing positive and negative peaks and the corresponding line scan.

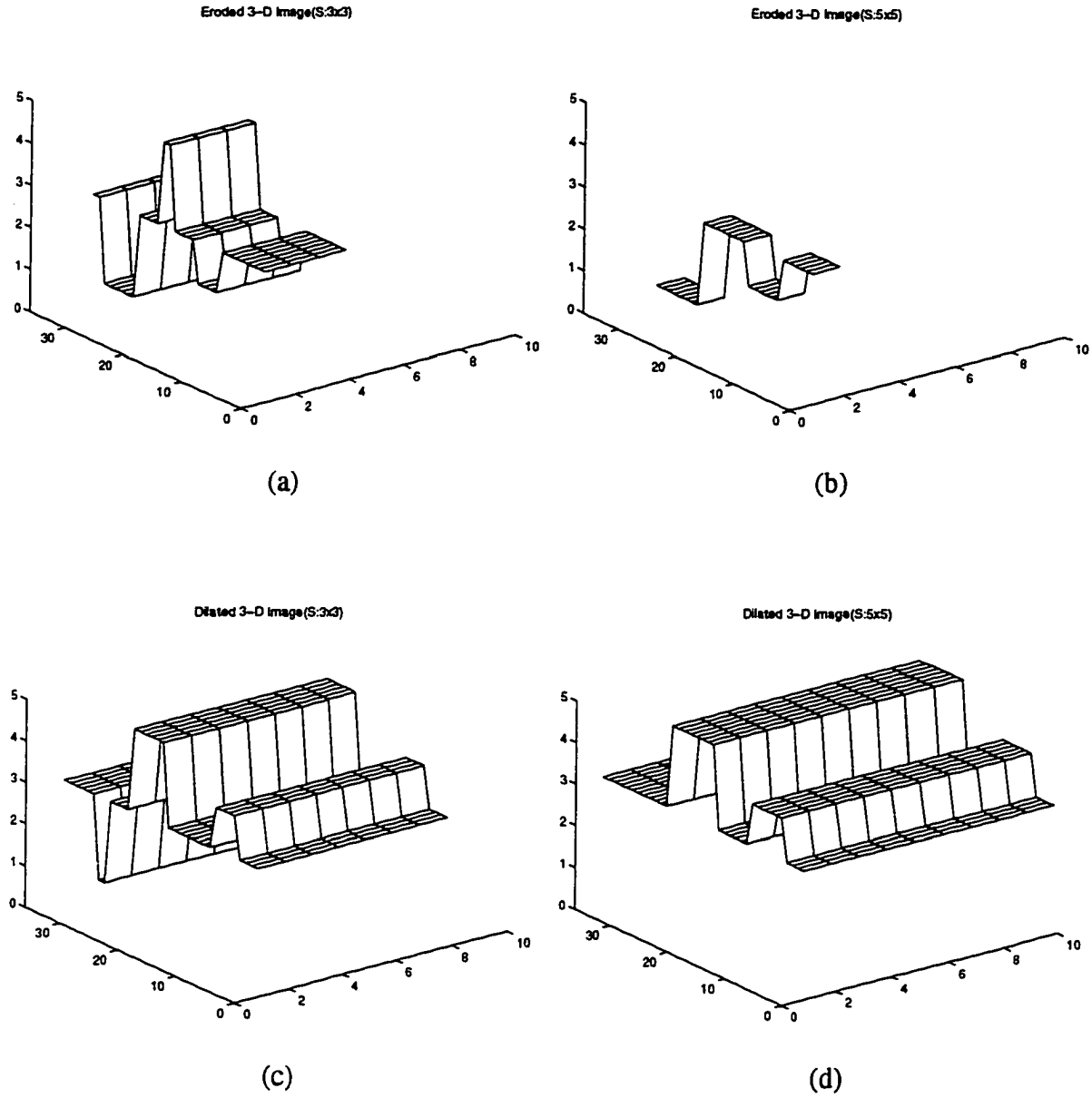

Figure 3.11. Gray scale morphological outputs obtained from the gray scale image shown in Figure 3.10(a).

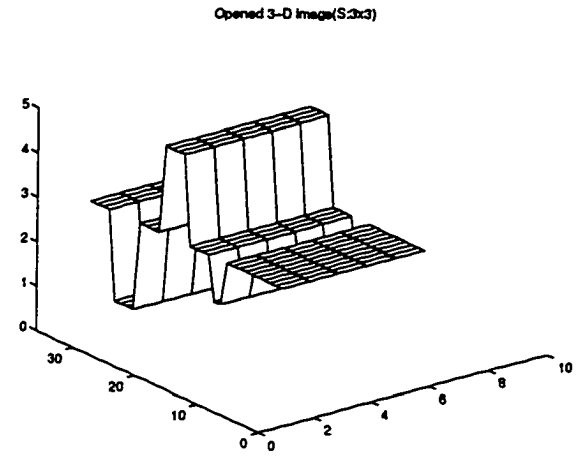

(e)

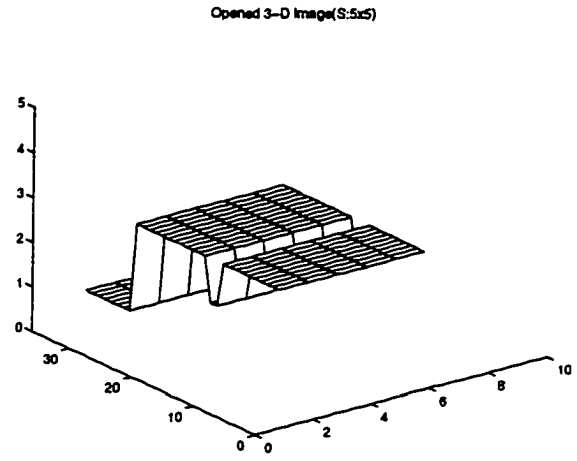

(f)

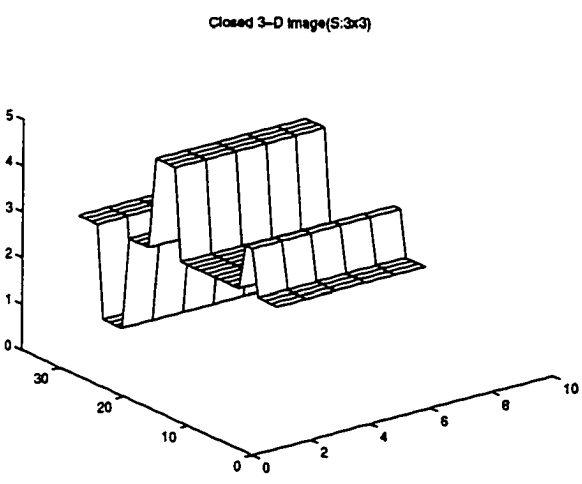

(g)

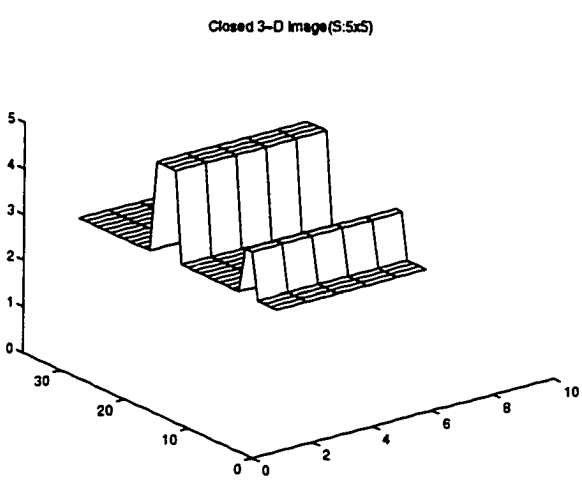

(h)

Figure 3.11. (Continued)

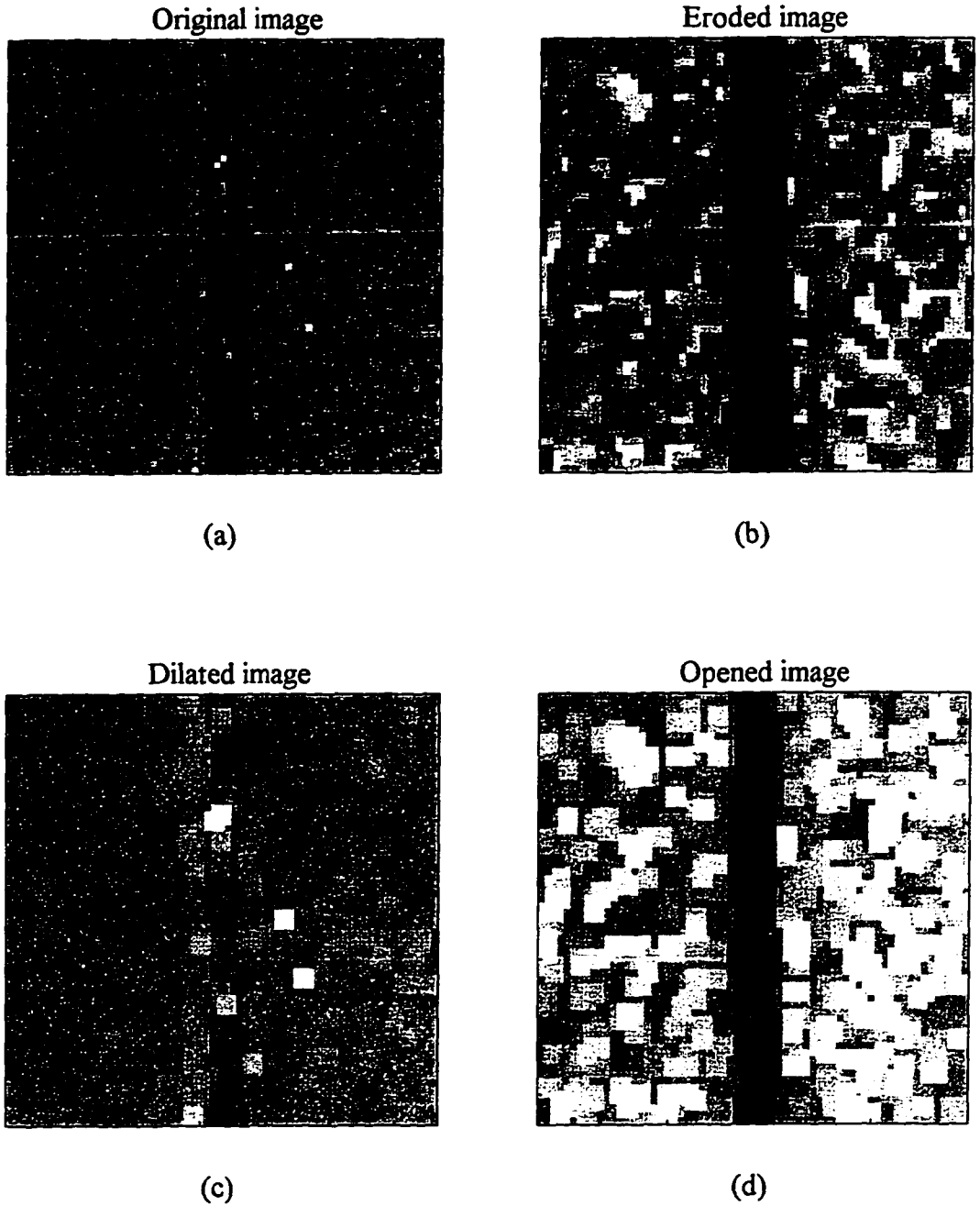

Figure 3.12. Gray scale morphological outputs obtained using the gray scale C-scan ultrasonic image and a flat symmetric square-type structuring element of size 3x3 pixels.

Closed image

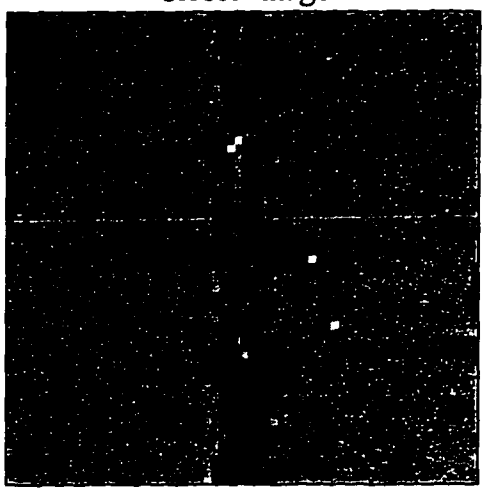

(e)

Morphological hybrid filtered image

(f)

Figure 3.12. (Continued)

operations preserve thin features, the noise reduction capability associated with the use of these operations is poor and the features in the resulting images are distorted.

Although the images processed using a morphological hybrid filter appear to be better than those obtained by implementing the more basic operations (erosion, dilation, opening and closing operations), the results are not satisfactory due to distortion introduced as a consequence of the nature of the morphological operations.

CHAPTER 4 A NEW MORPHOLOGICAL ALGORITHM FOR REDUCING SPECKLE NOISE IN ULTRASONIC IMAGES

This chapter describes a new speckle noise reduction algorithm. This algorithm is used to reduce speckle noise in the ultrasonic image prior to implementing the data fusion algorithm. The chapter begins with a literature review on noise reduction approaches and a brief description of conventional noise reduction techniques such as lowpass and median filters. The proposed algorithm is then described in detail using block diagrams. The performance of each block is illustrated by showing the input and output images obtained using an experimentally derived ultrasonic test image.

Literature Review: Noise Reduction Approaches

The development of tools for reducing noise in images represents one of the fundamental problems in image processing [77-80]. Such tools are particularly useful in NDE applications where they are often called upon to highlight flaws in low quality images. One of the major problems associated with ultrasonic images is the presence of speckle noise. The presence of speckle noise degrades image quality and sometimes makes it difficult to identify features (defects) of interest that are typically thin or small in nature.

A number of strategies have been proposed to date in order to reduce speckle noise and enhance the image quality. As an example, lowpass and median filters have been used widely to reduce noise in images. However, lowpass filters tend to blur sharp edges such as those introduced by surface breaking cracks in the material under test. It is well known that median

filters are capable of removing impulse type noise while preserving edges in images [81-86]. Unfortunately, when the spatial density of the noise is high as in the case of ultrasonic NDE images contaminated with speckle noise, median filters perform poorly [84,87]. A quantitative analysis of the streaking or blotching effects commonly observed in median filtered images is presented in detail by Bovik [88]. Morphological techniques have a demonstrated track record of success in reducing speckle noise in images [89,90,75]. Basart et al. [76], Saniie et al.[91,92] and Chu et al. [93] use morphological hybrid (lowpass) filters for minimizing speckle noise. However, it is observed that such filters often contribute to problems of distortion, particularly when thin and small objects (defects) are present in images, depending on the width and shape of the structuring element that is employed. A variety of techniques have been proposed in order to estimate the optimal morphological filter design using statistical approaches [72-74,94,95]. Unfortunately many of these techniques require an accurate model of the additive noise and image degradation process. It is also found that the estimation process involves computationally intensive search procedures [74]. One of the promising approaches involves the use of residual images obtained by employing a sequence of structuring elements [87.96]. These algorithms, however, tend to perform poorly if the signal-to-noise ratio is low. In addition they are usually computationally expensive to implement [87]. An alternative morphological approach for reducing speckle noise in ultrasonic images that uses a sequence of simple closing operations to generate residual images was proposed in [97,98]. Since each residual image contains noise as well as features of interest, it is necessary to isolate the features from the noise. In general, the amplitudes associated with ultrasonic speckle noise are lower than those of features. It may, therefore, be

possible to sort the noise pixels from the feature pixels using the histogram of each residual image. However, the histograms of residual images generated are usually not bimodal. Consequently the threshold level required to isolate noise pixels has to be determined using a trial and error approach.

Conventional Lowpass and Median Filters

Lowpass filters have been used widely in reducing noise in images. A typical example of a lowpass filter is a Butterworth lowpass filter. The transfer function of a Butterworth filter order n with cutoff frequency d_0 is given by

$$H(u,v) = \frac{1}{1+(\sqrt{2}-1)(d(u,v)/d_0)^{2n}} \tag{4.1}$$

where $d(u,v)$ is the distance from the origin to (u,v) in the frequency domain. By controlling the cutoff frequency d_0 and filter order n, we can design an appropriate lowpass filter for reducing high frequency noise at the expense of sharpness in images. One of the problems with linear filters such as lowpass filters is that they blur the edges in images. To prevent blurring, nonlinear filters such as median filters have been used widely. Median filters convert the gray level of a pixel into a median level in the neighborhood of that pixel. A basic two dimensional median filter of window size $(2l+1)$x$(2l+1)$ can be defined as

$$Y(m,n) = median\{G(m+i,n+j) \mid i,j = -l,\ldots,-1,0,1,\ldots,l\} \tag{4.2}$$

where $G(m,n)$ *and* $Y(m,n)$ represent the input and output of median filter at pixel coordinate (m,n), respectively.

Description of the Proposed Speckle Noise Reduction Algorithm

This dissertation proposes a new NDE data fusion algorithm using morphological approaches. The overall algorithm is implemented in two stages as shown in Figure 4.1, where the variables $G_u(m,n)$ and $G_e(m,n)$ denote the gray scale ultrasonic and eddy current images, and $S(m,n)$ represents the structuring element at the pixel coordinate (m,n). The first stage employs a morphological algorithm to reduce speckle noise in ultrasonic images. The second stage fuses the speckle noise reduced ultrasonic image with the eddy current image to obtain a composite image.

The proposed speckle noise reduction algorithm reduces unwanted artifacts in ultrasonic images prior to fusing ultrasonic and eddy current images. The algorithm is composed of four basic blocks: residual image generation, gating process, feature extraction and contrast enhancement. The overall block diagram is shown in Figure 4.2, where the input variables $G(m,n)$ *and* $S(m,n)$ denote the ultrasonic image and the structuring element at the pixel coordinate (m,n), respectively.

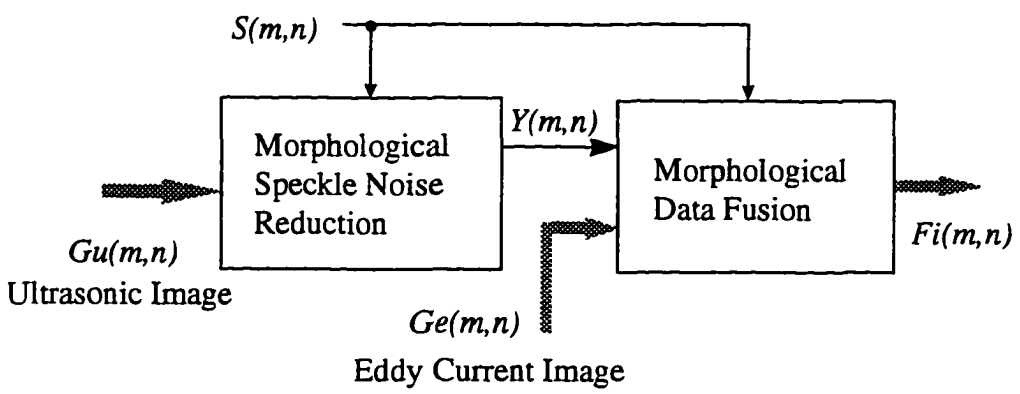

Figure 4.1. Overall block diagram of the NDE data fusion algorithm using morphological approaches.

First, a residual image generation block generates a sequence of residual images which are defined as the difference between morphological closed images using a pair of structuring elements of different sizes. Hence this block sieves objects of various sizes depending on the size of the structuring element that is used. Second, a gating process block recovers the original gray level amplitudes of the objects in a residual image. This gating process makes it easier to determine the threshold level required to isolate the desired features from noise in each residual image. Third, the feature extraction block isolates features from noise by thresholding each gated residual image. Finally, the contrast enhancement block serves to enhance the quality of the extracted feature images. In order to illustrate the function of each block, an experimentally derived ultrasonic sample image was used as a test image. Figure 4.3(a) shows the test specimen to obtain the ultrasonic image. The test specimen consists of a 6 mm thick aluminum sample machined with a butterfly shaped slot. The depth of the slot along each wing and center is 0.5 mm and 2.0 mm, respectively. An acoustic microscopy C-

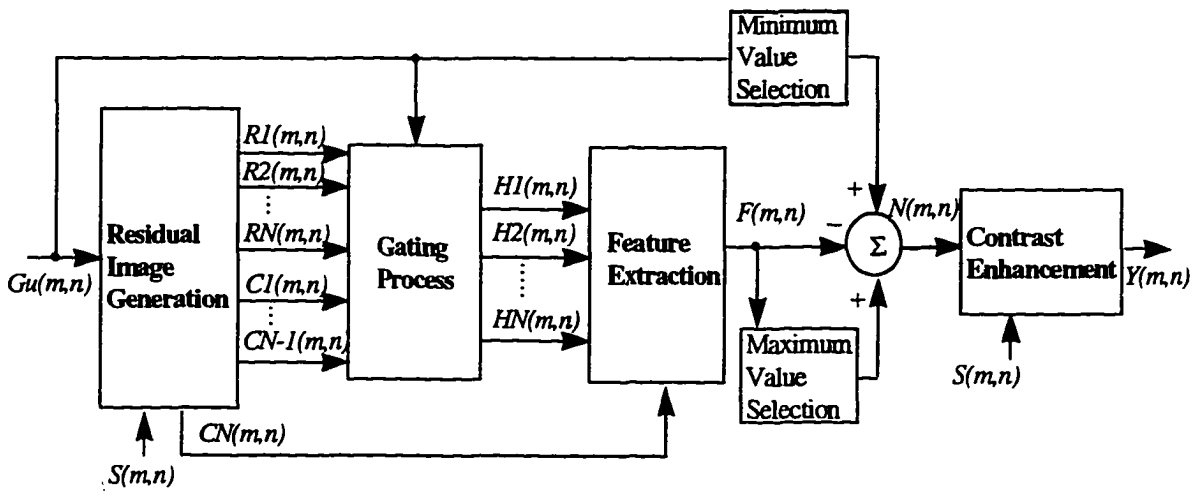

Figure 4.2. Block diagram of the proposed speckle noise reduction algorithm.

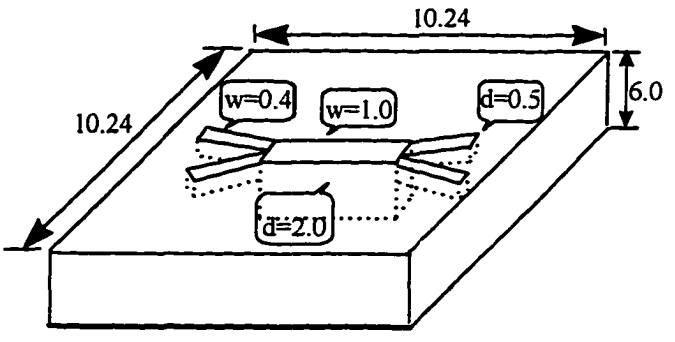

(a) unit : mm

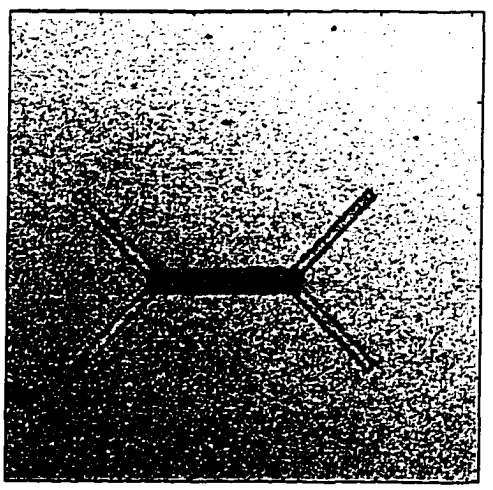

(b)

Figure 4.3. Specimen used in validation studies.

scan image of the specimen obtained using a 25 MHz focused transducer and a scanning step size of 40 μm is shown in Figure 4.3(b). A C-scan image of size 256 x 256 pixels was used for validating the approach. In implementing and simulating the algorithms, flat symmetric square-type structuring elements were used.

Residual image generation algorithm

The residual image generation block as shown in Figure 4.4 generates residual images using a sequence of morphological closing operations employing different structuring elements. The closing operations consists of a cascade of morphological dilation and erosion operations. If a flat symmetric structuring element is used, the dilation operation sets the gray level of a pixel to the maximum gray level in the neighborhood contained within the domain of the structuring element. An erosion operation following the dilation operation restores the shape of dilated objects that are not replaced by the maximum gray level in the neighborhood to that of original image. In addition, it restores the size of dilated image to that of the original image.

Consider three flat symmetric square-type structuring elements, S_1, S_2 and S_3 of sizes 3 x 3, 5 x 5 and 7 x 7 pixels, respectively. In Figure 4.4, C_1 denotes the result after a closing operation using S_1. C_1 contains objects that are equal to or greater than the structuring element S_1 of size 3 x 3 pixels. Hence the residual image $R_1=C_1-G$ is composed of objects smaller than S_1 (3 x 3 pixels). Similarly the residual images $R_2=C_2-C_1$ and $R_3=C_3-C_2$ are composed of objects which are greater than or equal to S_1 but smaller than S_2 (5 x 5 pixels), and greater than or equal to S_2 but smaller than S_3 (7 x 7 pixels). In general, if we use a pair

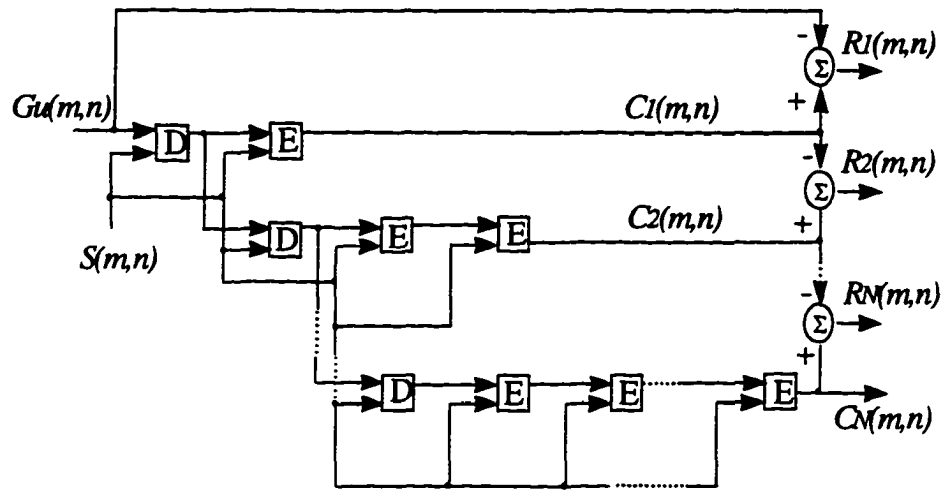

Figure 4.4. Block diagram of the residual image generation algorithm.

of structuring elements with different sizes, for example $(2k+1)$ x $(2k+1)$ and $(2k+3)$ x $(2k+3)$ pixels where $k=1,2,\ldots$, in closing operations as shown in Figure 4.4, the difference image obtained by subtracting the closed image with structuring element of size $(2k+1)$ x $(2k+1)$ pixels from that of size $(2k+3)$ x $(2k+3)$ pixels contains objects that are greater than or equal in size to $(2k+1)$ x $(2k+1)$ but less than $(2k+3)$ x $(2k+3)$ pixels. Hence a residual image generation block serves as a sieve, isolating objects of various sizes depending on the size of the predetermined structuring element. Mathematical representations of the residual images are described in the appendix.

The structuring element decomposition theorem described in chapter 3 can be used to implement the block shown in Figure 4.4 efficiently. Assume a M x M flat symmetric square-type structuring element, where M is an odd, positive integer and $M \geq 3$. This structuring element can be decomposed into $(M - 1) / 2$ structuring elements with the smallest structuring element of size 3 x 3 pixels. If we perform closing operations using a structuring element of

size M x M pixels in images, the total number of image translations is equal to $(M^2 - 1)$. However, if we decompose the structuring element of size M x M pixels into $(M - 1) / 2$ structuring elements with each size 3 x 3 pixels, the total number of image translations reduces to $8(M - 1) / 2 = 4(M - 1)$. Thus the relative reduction in image translations equals to $R_T = (M^2 - 1 - 4M + 4) / (M^2 - 1) \times 100 = (M^2 - 4M + 3) / (M^2 - 1) \times 100$ (%). For example, if M = 5, 7, 9, 11 and 13, then the corresponding values of R_T are 33, 49, 60, 66 and 77 %, respectively. Thus, as the structuring element size increases, the structuring element decomposition theorem allows us to reduce the computational load significantly. If N residual images are generated as shown in Figure 4.3, then the total number of dilation or erosion operations becomes $N (N + 1) / 2$. If we utilize the dilation output associated with the previous closing operation in the next dilation operation, we can reduce the number of decomposed dilation operations even further. Thus, for the N residual images, we need only N dilation operations with the smallest structuring element size 3 x 3 pixels. Hence we can reduce the number of dilation operations by $N (N + 1) / 2 - N = N (N - 1) / 2$. For example if $N = 5$, we can save 10 dilation operations using the scheme shown in Figure 4.4. Figure 4.5 shows examples of residual images generated. The images shown in Figure 4.5 were obtained using flat symmetric square-type structuring elements of sizes that sieve objects which are (a) less than 3 x 3 pixels (b) greater than or equal to 3 x 3 but less than 5 x 5 pixels (c) greater than or equal to 5 x 5 but less than 7 x 7 pixels (d) greater than or equal to 7 x 7 pixels, respectively. The dark regions represent high gray levels and vice versa.

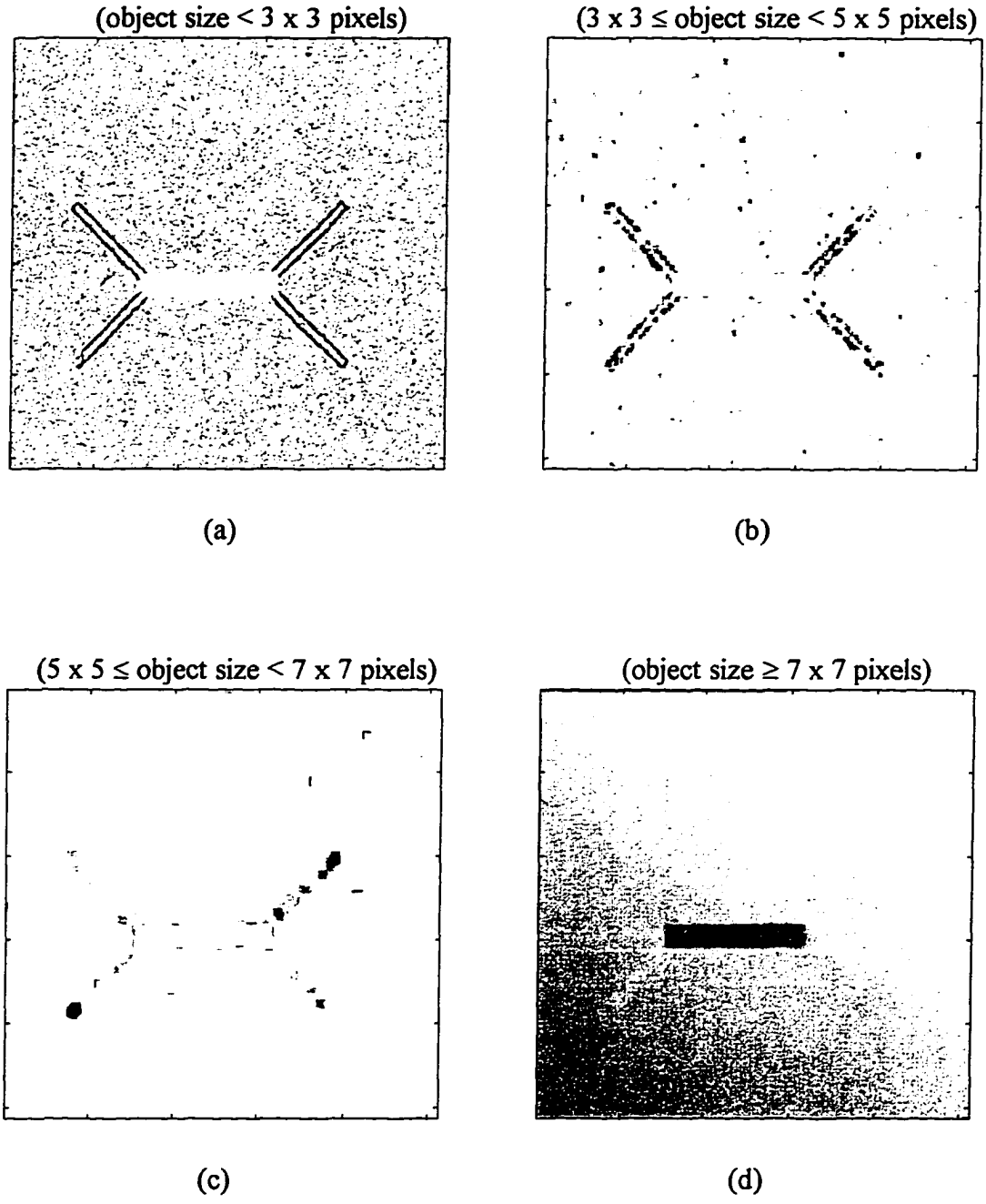

Figure 4.5. Sample images obtained using the residual image generation algorithm.

Gating algorithm

In the second step, a bank of gating blocks as shown in Figure 4.6 is used to recover the original gray levels of the objects in a residual image. The gating or indicator function is defined as

$$I_k(m,n)=\begin{cases}1 & \text{if } R_k(m,n)>0\\ 0 & \text{if } R_k(m,n)=0\end{cases} \tag{4.3}$$

where $R_k(m,n)$ denotes the *kth* residual image function at the pixel coordinate (m,n). The output of the *kth* gate can be written as

$$H_k(m,n)=I_k(m,n)\{max(G)-C_{k-1}(m,n)\} \tag{4.4}$$

where G and C_{k-1} denote the original and $(k-1)th$ closed image functions, and $C_0=G$.

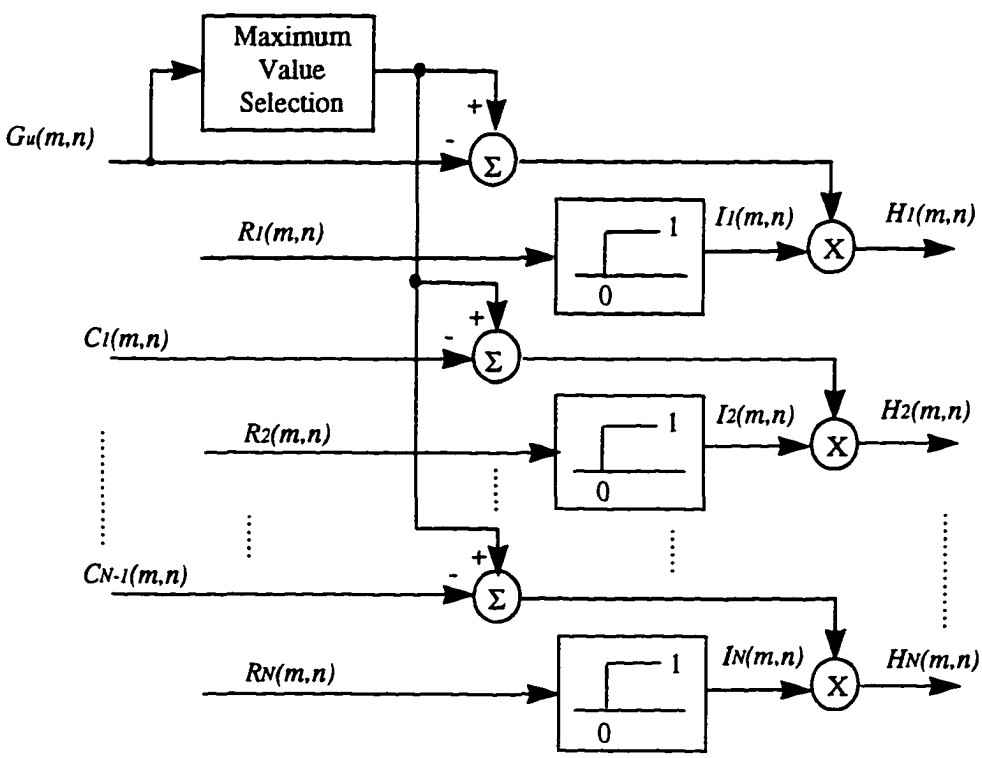

Figure 4.6. Block diagram of the gating algorithm.

Figures 4.7(a) through (c) show examples of gated residual images. The image shown in Figure 4.7(d) was obtained by performing a closing operation using a flat square-type structuring element of size 7x7 pixels. Once again, the dark regions represent high gray levels and vice versa. From the results shown in Figures 4.5 and 4.7(a) through (c), it is apparent that the sieved objects are highlighted much more effectively in the gated residual image. Figures 4.8 and 4.9 show the histograms of the residual images obtained with and without using the gating process. It is clear that the gating process makes it easier to eliminate the threshold level required to distinguish the desired features from noise.

Feature extraction algorithm

A feature extraction block, shown in Figure 4.10, is used in the third step to isolate features from speckle noise by thresholding each gated residual image. Examples of feature images extracted by thresholding the gated residual images whose histograms are shown in Figure 4.8 are presented in Figure 4.11. The images were obtained by thresholding the gated residual images shown in Figures 4.7(a) through (d) with threshold levels set at 95, 80, 70 and 70, respectively.

Contrast enhancement algorithm

A morphological contrast enhancement process is employed in the final step as shown in Figure 4.12 to improve the quality of the extracted feature image. If $F(m,n)$ denotes the input image and $Y(m,n)$ represents the output of the contrast enhancement block, then [99]

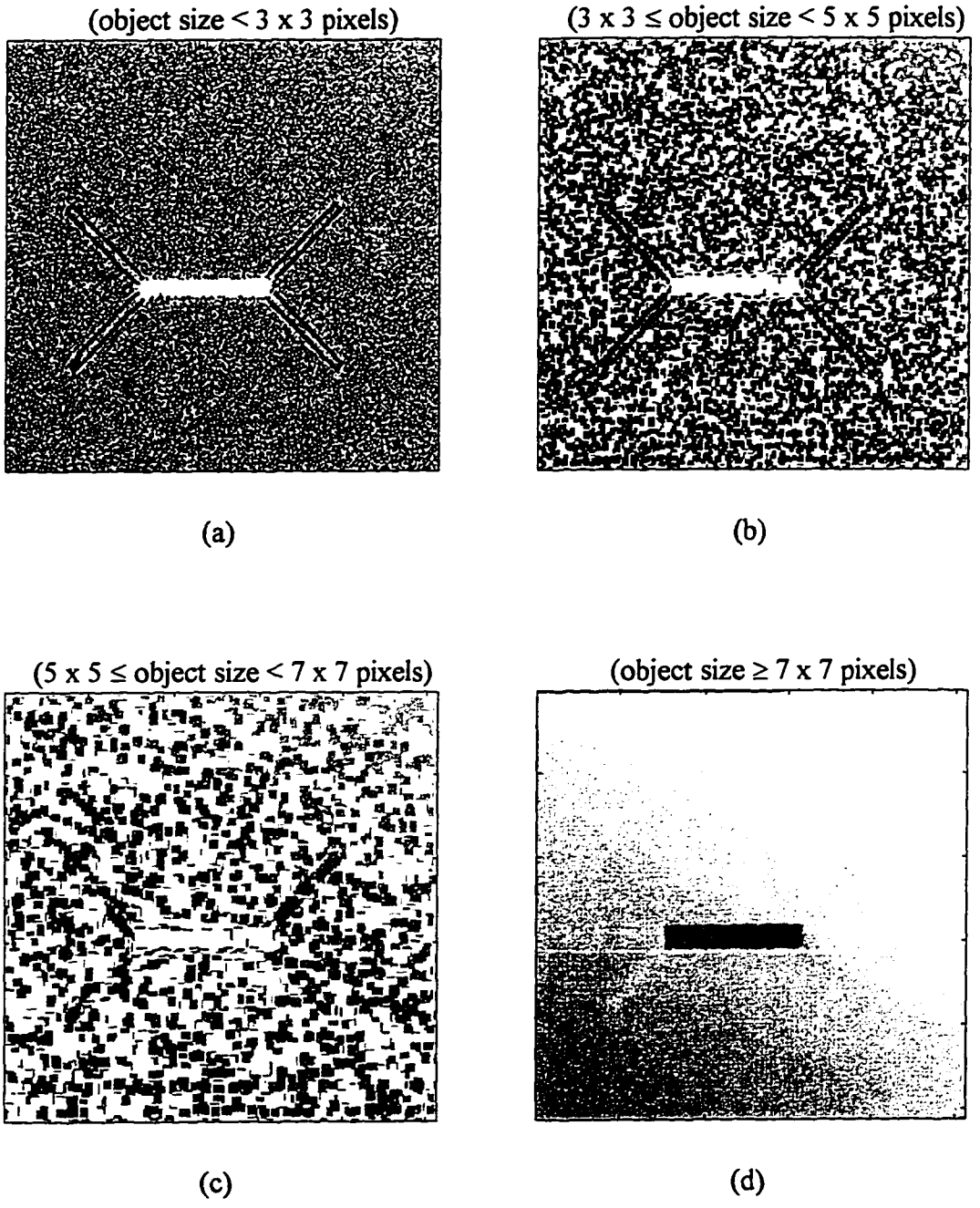

Figure 4.7. Sample images obtained using the gating algorithm.

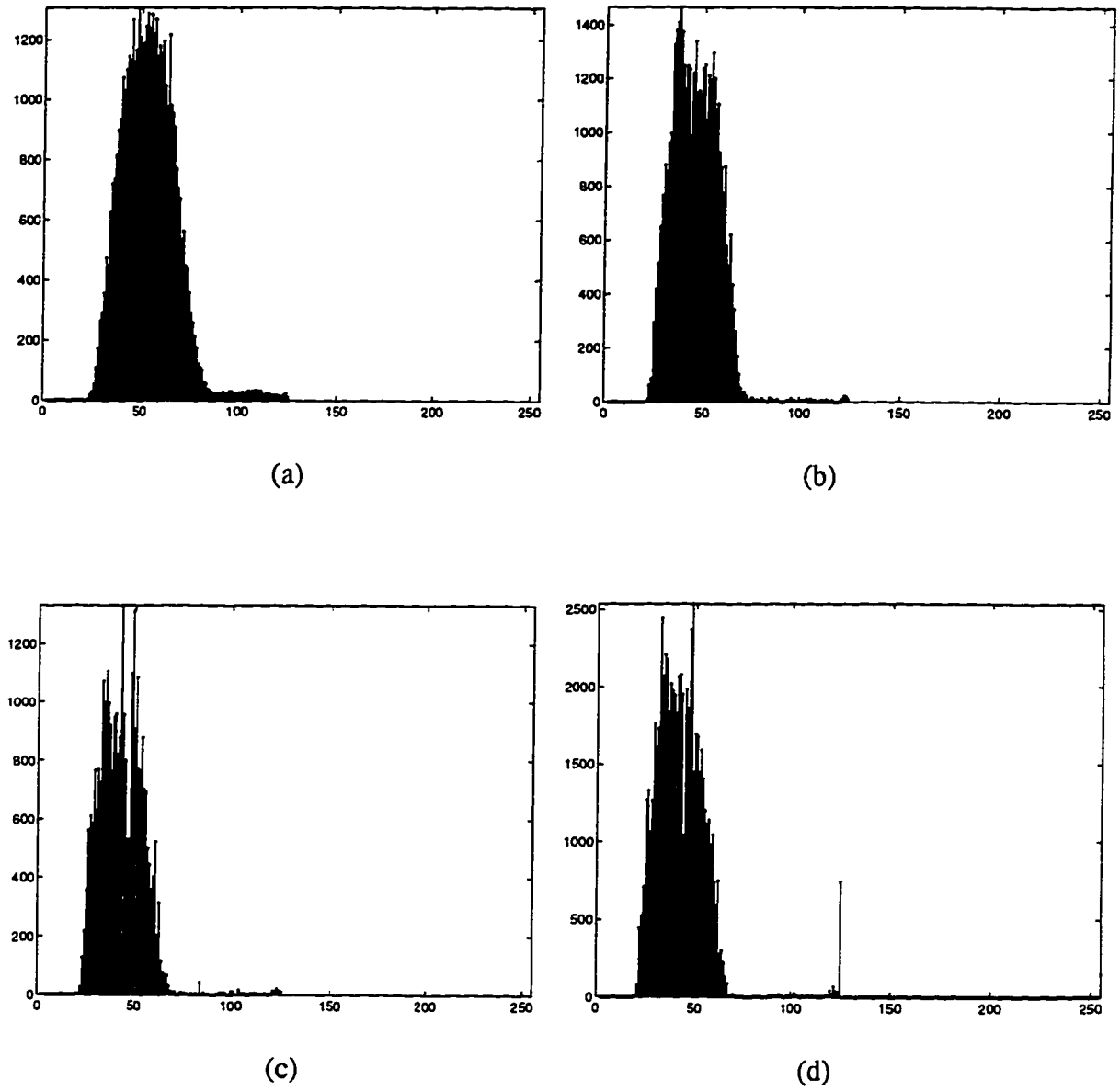

Figure 4.8. Histograms of the gated residual images. . The original images are shown in Figure 4.7.

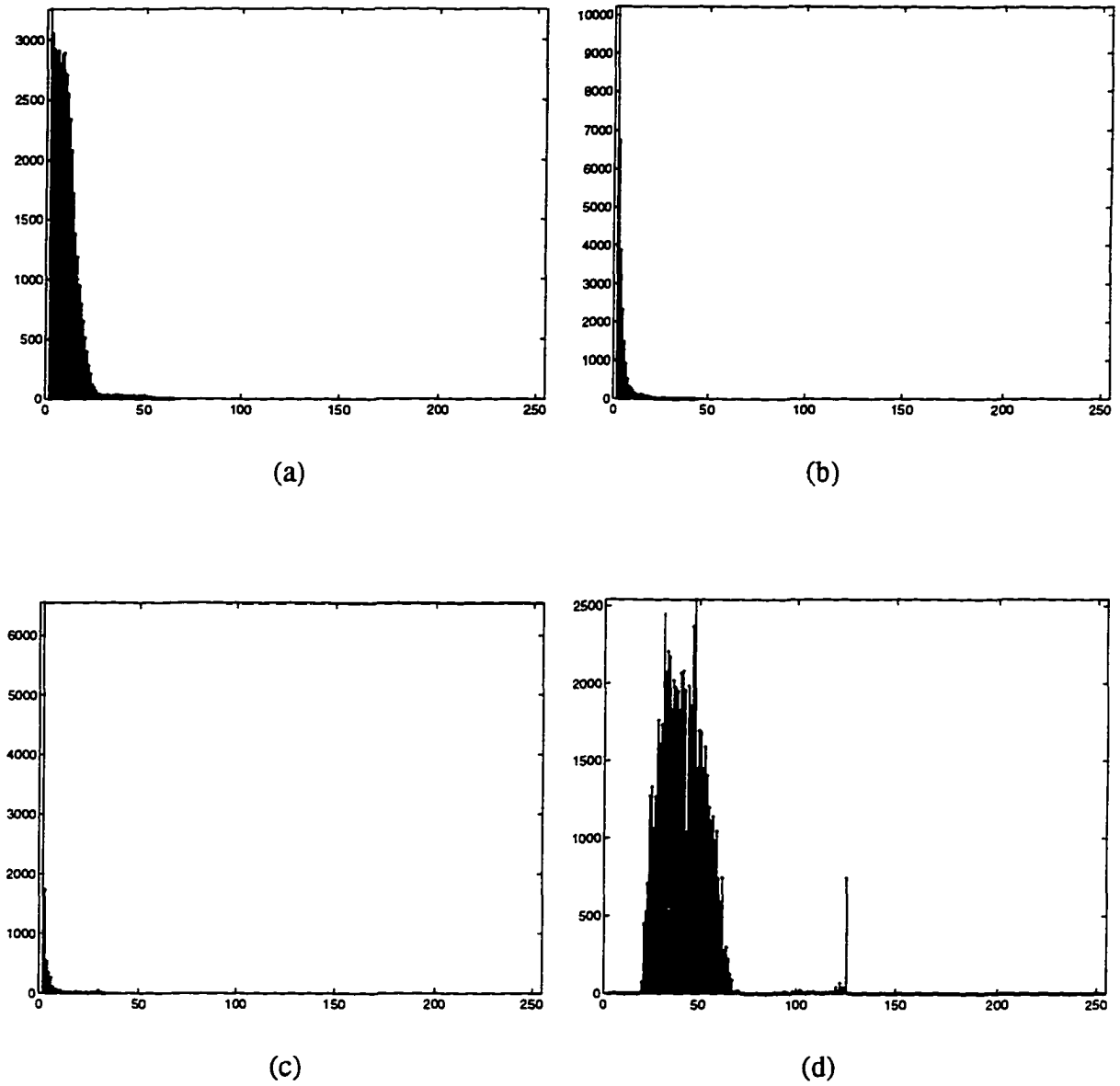

Figure 4.9. Histograms of the residual images. The original images are shown in Figure 4.5.

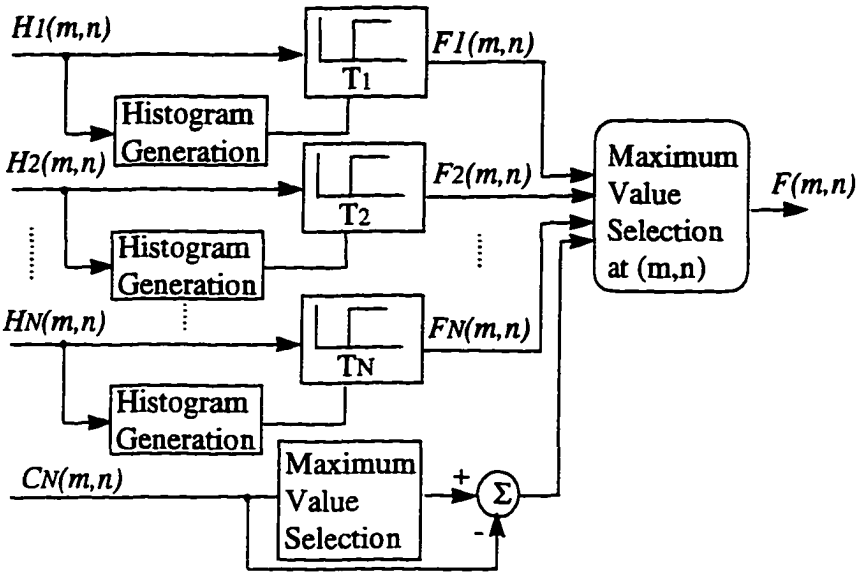

Figure 4.10. Block diagram of the feature extraction algorithm.

$$Y(m,n)=\begin{cases} D(F,S)(m,n) & \text{if } D(F,S)(m,n)-F(m,n)<F(m,n)-E(F,S)(m,n) \\ E(F,S)(m,n) & \text{otherwise} \end{cases} \quad (4.5)$$

where (m,n) represents the pixel coordinate. If the gray level of a pixel is close to the maximum or minimum gray level in the domain of the translated structuring element, the gray level of the pixel is set at the maximum or minimum gray level as shown in Figure 4.12. The sharpness of edges can be enhanced as a result of this process. The images shown in Figures 4.13(a) and (b) were obtained before and after using the contrast enhancement algorithm, respectively. Figure 4.14 shows sample images obtained from the image shown in Figure 4.3(b) using a 2nd order Butterworth lowpass and median filters, and the proposed algorithm. Figure 4.15 shows another test specimen and the corresponding normal incidence ultrasonic C-scan image obtained using a 60MHz focused transducer and a scanning step size of 40 μm. The specimen consists a 6 mm thick aluminum sample with a 0.5 mm deep and

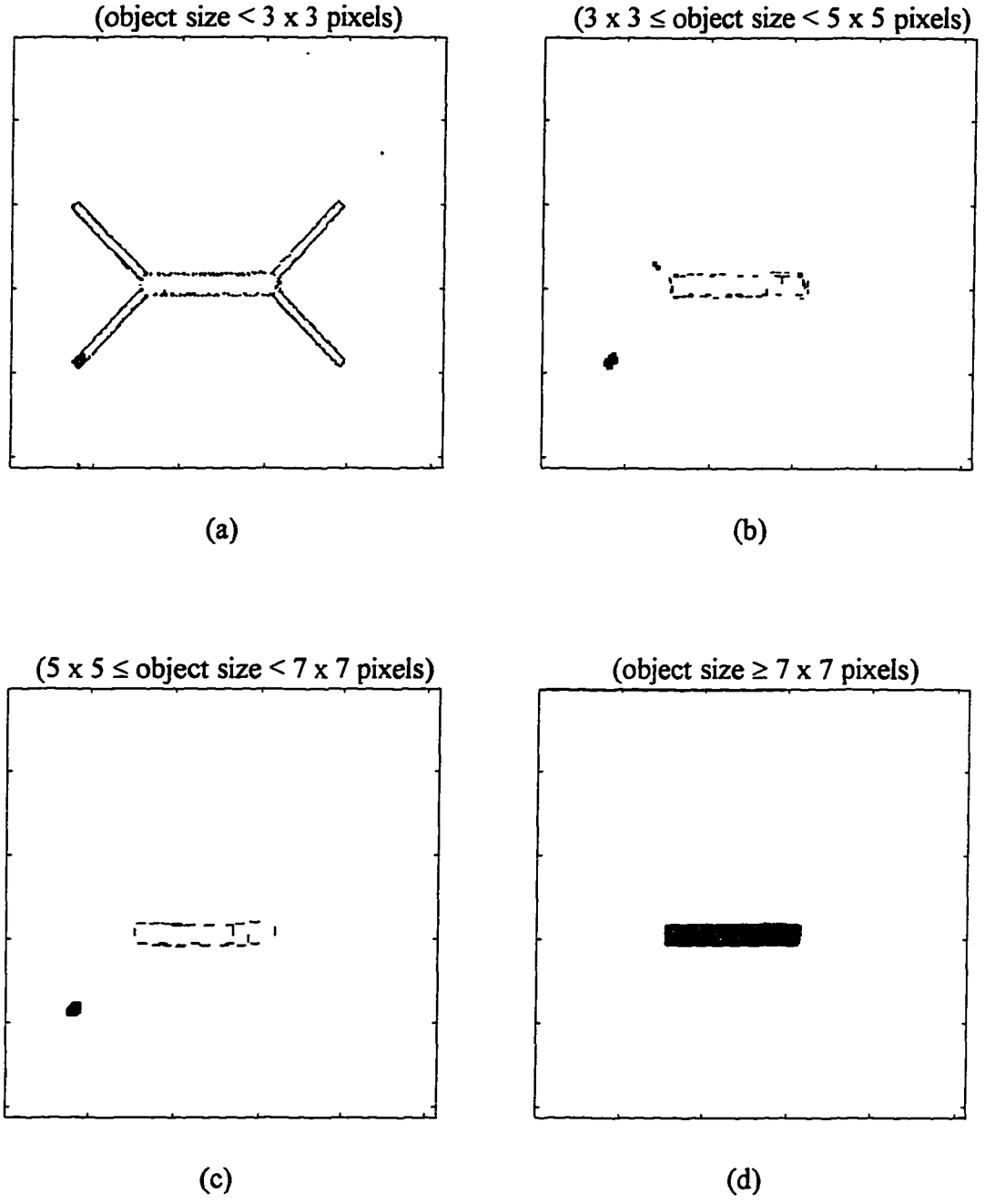

Figure 4.11. Images obtained using the feature extraction algorithm. The histograms of these images are shown in Figure 4.8 and the original images are presented in Figure 4.7.

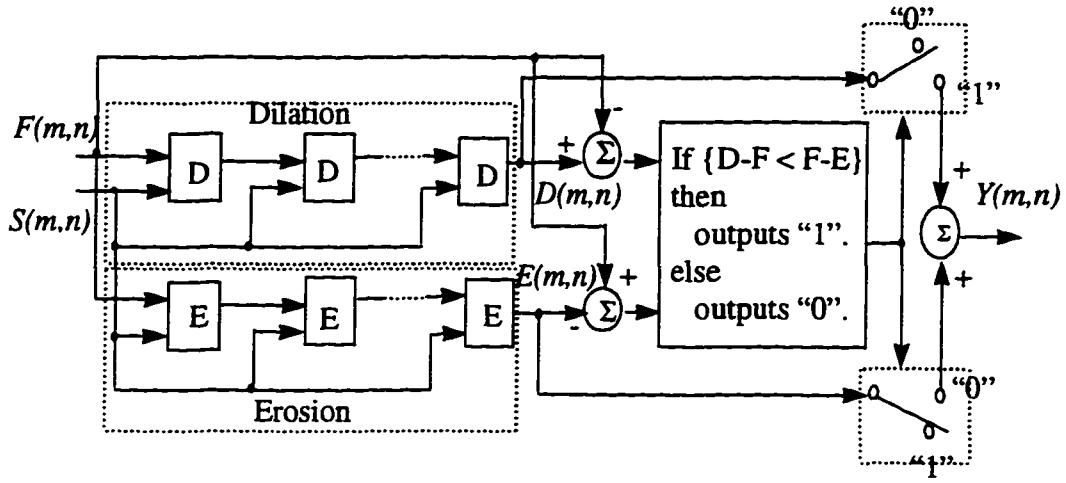

Figure 4.12. Block diagram of the contrast enhancement algorithm.

0.2 mm wide slot machined on it. Figures 4.16(a) through (c) show noise reduced images obtained using a 2nd order Butterworth lowpass and median filters, and the proposed algorithm, respectively. The lowpass filtered image shown in Figures 4.14 and 4.16(a) were obtained by setting the filter cutoff radius equal to 130 and 70 which corresponds to 99.46 and 97.76 % of the total energy, respectively. The window size of the median filter was 5 x 5 pixels.

It is obvious from the images shown in Figures 4.14 and 4.16(a)-(b) that lowpass filtering has a blurring effect on thin features and edges. Also, median filters perform poorly when the spatial density of noise is high. In contrast to lowpass and median filters, the image shown in Figures 4.14 and 4.16(c) shows that the proposed algorithm is able to remove noise while preserving thin features and edges in the image.

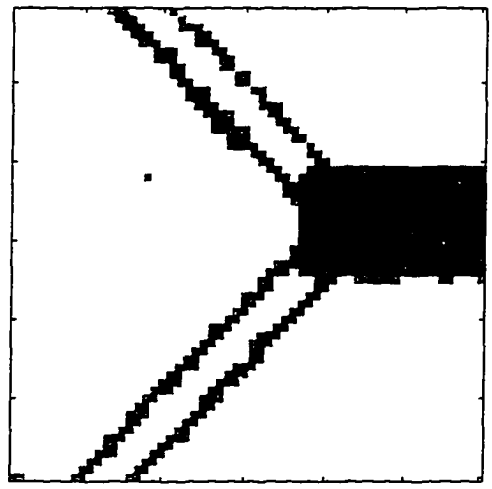

(a)

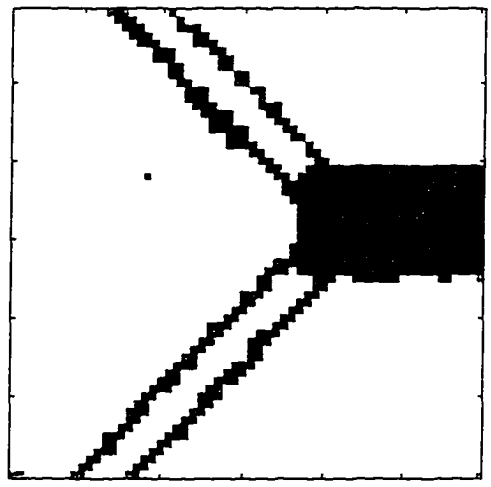

(b)

Figure 4.13. Images obtained (a) before and (b) after using the contrast enhancement algorithm.

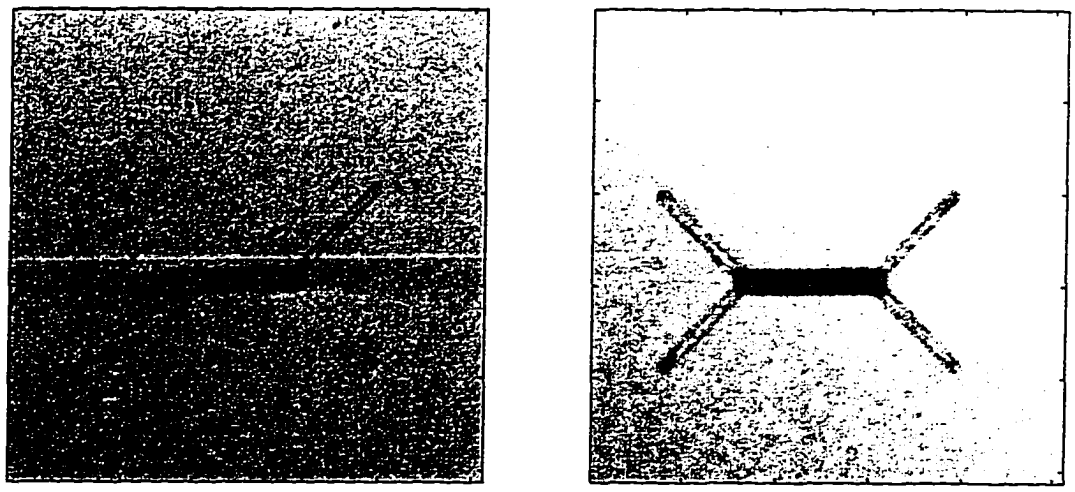

(a) (b)

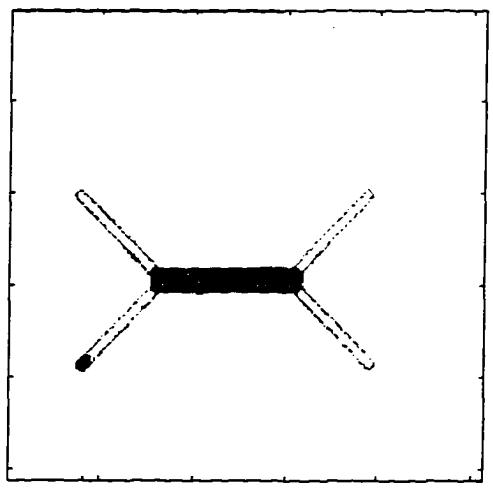

(c)

Figure 4.14. Sample images obtained using conventional noise reduction filters and the proposed speckle noise reduction algorithm. (a) Lowpass (Butterworth) filtered image. (b) Median filtered image. (c) Image obtained using the proposed morphological approach.

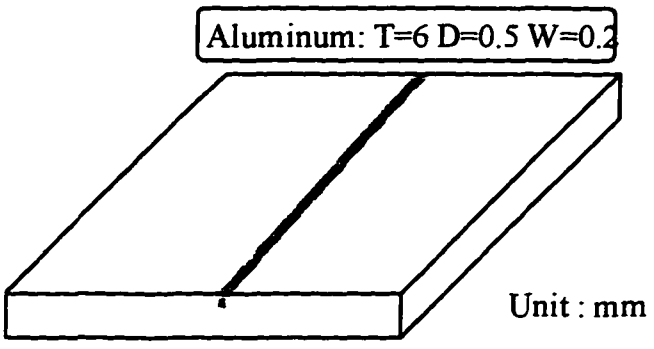

(a)

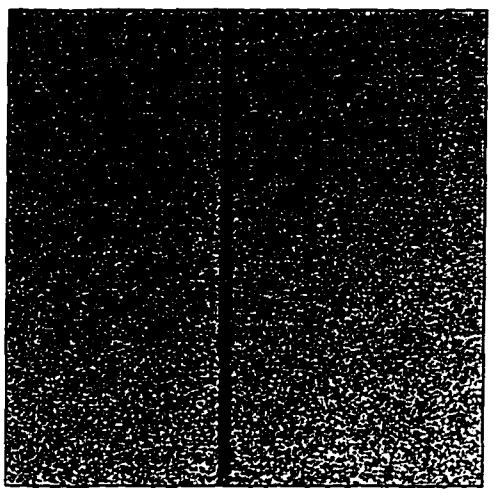

(b)

Figure 4.15. Example of C-scan ultrasonic image. (a) Specimen details. (b) Corresponding C-scan ultrasonic image.

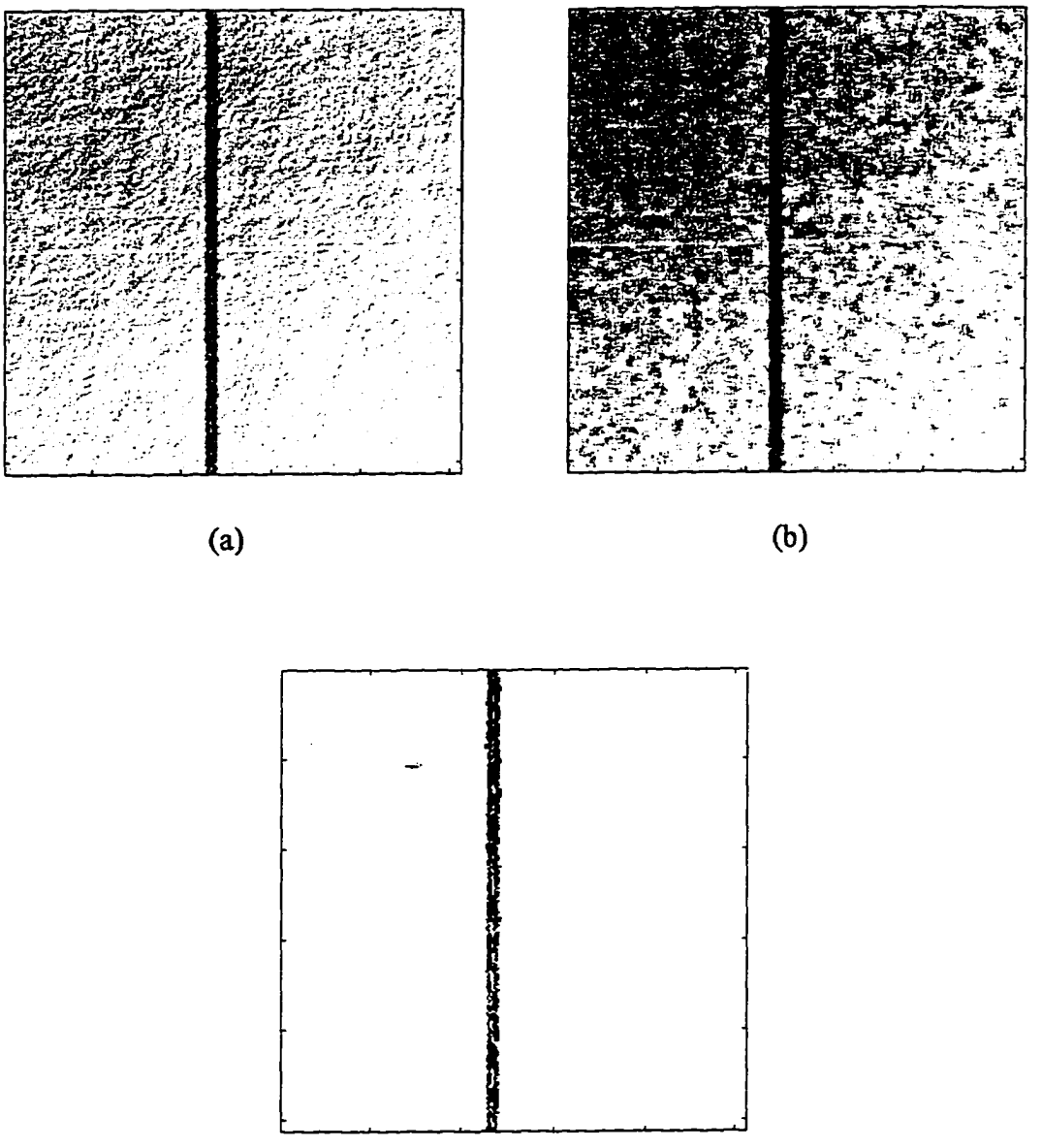

Figure 4.16. Noise reduced images. (a) Lowpass (Butterworth) filtered image. (b) Median filtered image. (c) Image obtained using the proposed algorithm.

CHAPTER 5 A NEW MORPHOLOGICAL ALGORITHM FOR FUSING ULTRASONIC AND EDDY CURRENT IMAGES

This chapter describes the second stage of the overall NDE data fusion algorithm which involves fusion of the speckle noise reduced ultrasonic image with the eddy current image. The speckle noise reduced image is used to derive information relating to the locations and boundaries of the flaw using a morphological closing operation. The gray levels of the eddy current image are then superimposed within the defect regions using an AND operation to obtain the fused image. Simulation results obtained using the proposed data fusion algorithm from the sample image illustrated in chapter 4 are compared with those of the multi-resolution decomposition technique employing LMMSE filters. A brief description of the LMMSE approach follows for the sake of completeness.

Data Fusion Using LMMSE Filters

The multi-resolution decomposition techniques employing LMMSE filters were proposed by Yim et al. [43,44] as a tool for fusing data. The method assumes that the measured NDE images can be represented using a linear model with additive random noise. The objective of the method is to linearly combine the noisy versions of the images in a manner, then minimizes the energy in the error image in the least square sense. Figure 5.1 shows a block diagram of the LMMSE filter for N inputs where $s(t)$ and $\hat{s}(t)$ denote the input signal representing the true NDE image and the fused image representing the output of the LMMSE filter, respectively. The variables $H_i(w)$, $y_i(t)$, $n_i(t)$, $x_i(t)$ and $G_i(w)$ depicted in Figure 5.1 denote

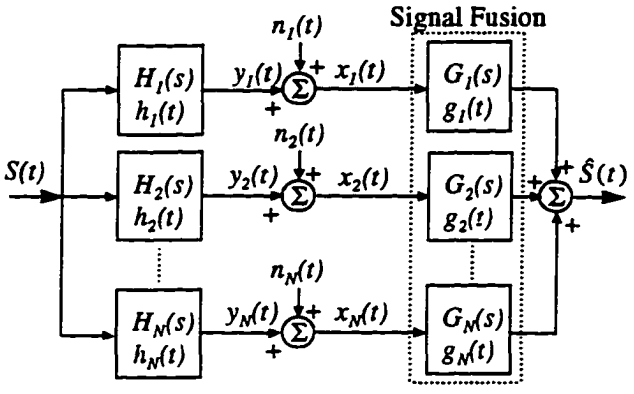

Figure 5.1. Block diagram of the LMMSE filter employing multiple inputs.

the transfer function of degradation process, degraded signal, additive noise, the input image and the transfer function of desired restoration filter at the *jth* stage, respectively, where $1 \le j \le N$ and N denotes the total number of inputs. In case of two NDE image inputs, $G_j(w)$ can be derived and shown to be [44]:

$$G_j(\omega_1,\omega_2) = \frac{\sqrt{S_S(\omega_1,\omega_2)\{S_{x_j}(\omega_1,\omega_2) - S_{n_j}(\omega_1,\omega_2)\}}}{-S_{n_j}(\omega_1,\omega_2) + S_{n_j}(\omega_1,\omega_2)\sum_{i=1}^{2}\frac{S_{x_i}(\omega_1,\omega_2)}{S_{n_i}(\omega_1,\omega_2)}} \quad for\ 1 \le j \le 2. \tag{5.1}$$

where $S_S(\omega_1,\omega_2)$, $S_{x_j}(\omega_1,\omega_2)$ *and* $S_{n_j}(\omega_1,\omega_2)$ denote the power spectra of $s(m,n)$, $x_j(m,n)$ and $n_j(m,n)$, respectively. Unfortunately it is often not easy in practice to obtain the transfer function associated with the degradation process and noise spectra. The problem can be simplified if we assume that the noise power is much smaller than that of the signal and the noise spectra are all identical. Under these assumptions, (5.1) can be approximated as

$$G_j(\omega_1,\omega_2) = K\frac{\sqrt{S_{x_j}(\omega_1,\omega_2)}}{\sum_{i=1}^{2} S_{x_i}(\omega_1,\omega_2)} \tag{5.2}$$

We use the results obtained using equation (5.2) to compare the performance obtained using the algorithm presented in this dissertation.

Description of the Proposed Data Fusion Algorithm

The data fusion algorithm, shown in Figure 5.2, involves combining the speckle noise reduced ultrasonic image with the eddy current image. We begin the process by using a morphological closing operation to obtain an outline of the defect from the speckle noise reduced ultrasonic image. The major challenge associated with this step lies in identifying a structuring element that is optimal in size. This is accomplished by computing the granulometric size distribution [61,65] using iterative closing operations with a sequence of structuring element sizes.

$Y(m,n)$ and $F_i(m,n)$ in Figure 5.2, denote the speckle noise reduced and fused images. $S_k(m,n)$ denotes the kth structuring element in a family of structuring elements of different sizes. The preprocessed ultrasonic image containing the outline of the defect is thresholded to obtain a binary image where the defect outline pixels have a gray level 'one' while the background or non-defect outline pixels are tagged 'zero'. As mentioned in chapter 1, it is observed very often that in practice single C-scan acoustic microscopy images offer little information for inferring the depth of narrow cracks. Consequently such images are utilized largely to identify the boundary of the defect.

The morphological closing operation is capable of filling "holes" whose characteristics do not "match" those of the predetermined structuring element. The closing operation can be used, therefore, to merge the unidentified defect regions. The challenge is to determine the

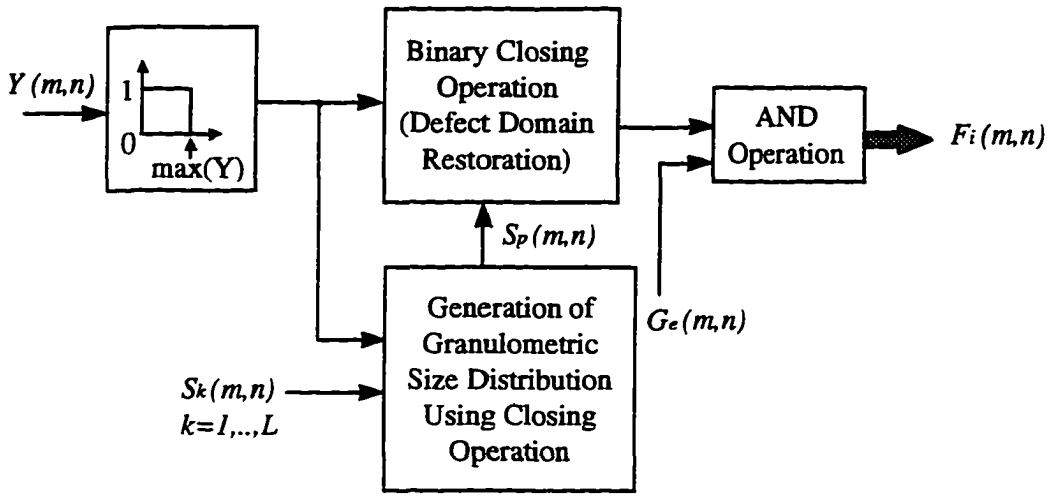

Figure 5.2. Block diagram of the proposed morphological data fusion algorithm.

size of the structuring element that is necessary to merge such regions effectively. We estimate the structuring element size by examining the granulometric size (density) distribution obtained by using iterative closing operations. Consider a sequence of structuring elements $\{S_k \mid k=0,1,2,\ldots\}$, where S_{k+1} is a superset of S_k. Since the closing operation has the extensivity property, the closed image $C(B, S_{k+1})$ is also a superset of $C(B, S_k)$. Thus if we define $N'(k)$ as the number of pixels activated in $C(B,S_k)$, then $N(k)=N'(k)/M^2$, called the granulometric size distribution, is a nondecreasing function of k, where M^2 is the total number of pixels in the image. Here, $N(0)$ is the fraction of pixels activated in the binary image B itself. The granulometric size density can be computed using $p(k)=\{N(k+1)-N(k)\}$. The optimal size of the structuring element can be determined by looking for abrupt transitions in the granulometric size density. After identifying the appropriate structuring element size $S_p(m,n)$, binary closing operations are performed to restore the defect regions. Figures 5.3(a) and (b) show the original ultrasonic and eddy current images obtained from the specimen shown in

Figure 4.3(a). Figure 5.4(a) and (b) show examples of granulometric size and density functions obtained from the image shown in Figure 5.3(a). The variable k along the horizontal axes in Figures 5.4(a) and (b) indicate that the size of the structuring element is $(2k+1)$ x $(2k+1)$ pixels, $k=1,2,....$ In Figure 5.4(a), the values of vertical axis represent the normalized numbers of pixels which are merged using binary closing operations employing structuring elements of size $(2k+1)$ x $(2k+1)$ pixels, $k=1,2,....$ In this example, a structuring element of size 5 x 5 pixels was determined to be optimal based on the granulometric size density function. A closing operation using this structuring element was performed to merge the unidentified defect regions in the binary image to obtain the result shown in Figure 5.4(c). The gray levels in the eddy current image shown in Figure 5.3(b) are then superimposed on the defect regions using an AND operation as shown in Figure 5.2. The highest gray level in the original eddy current image was chosen as the background level in the fused image in simulation. Figures 5.5(a) and (b) show sample line scans of the original ultrasonic and eddy current images shown in Figures 5.3(a) and (b), respectively. Figures 5.6 and 5.7 show the fused images and their line scans obtained using the proposed algorithm and the multi-resolution decomposition technique, respectively. A line scan of the fused image shown in Figure 5.6(b) reveals the gray level transitions in the defect region. The fused image obtained using the proposed algorithm reveals the defect locations and their gray levels clearly demonstrating the effectiveness of the approach compared to the multi-resolution decomposition technique employing LMMSE filters.

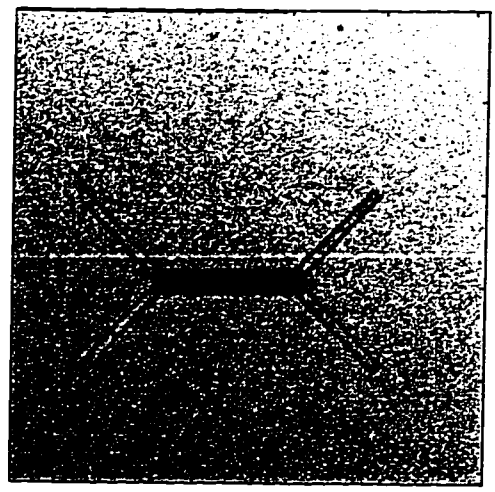

(a)

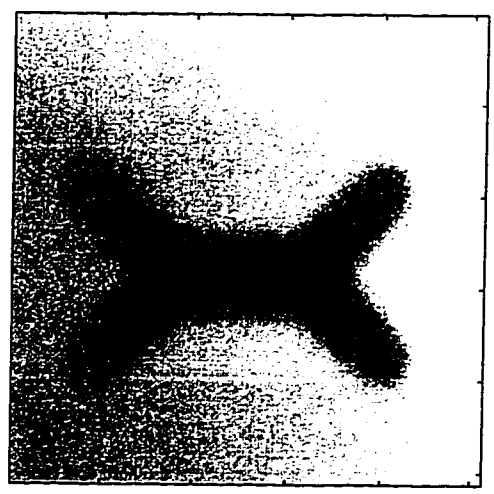

(b)

Figure 5.3. Original ultrasonic and eddy current images.

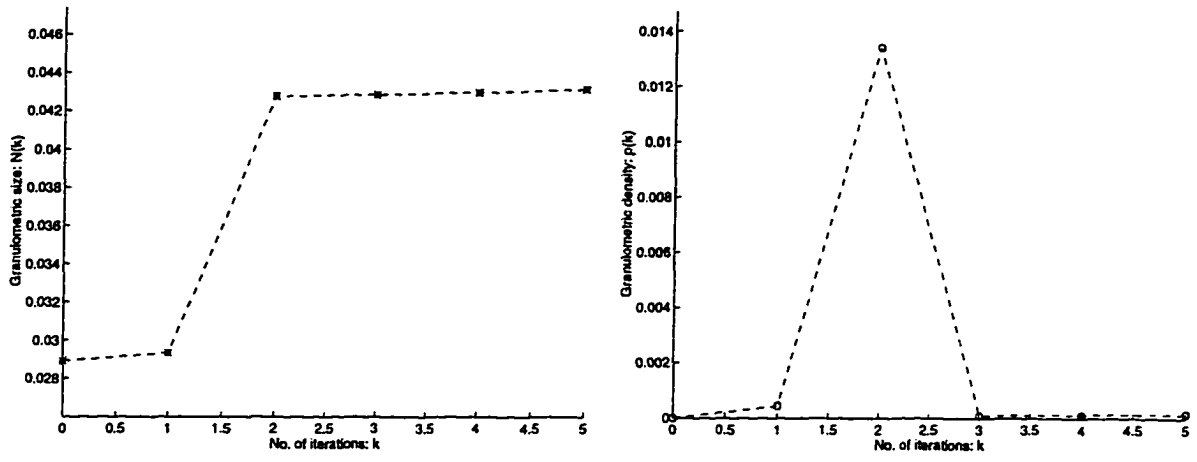

(a) (b)

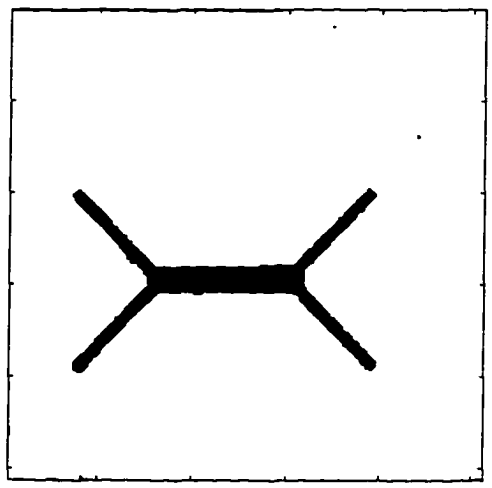

(c)

Figure 5.4. Granulometric size distribution and density, and restored binary image obtained using the algorithm shown in Figure 5.2. (a) and (b) Granulometric size distribution and density for the image shown in Figure 5.3(a), respectively. (c) Restored binary image obtained after using a closing operation employing a structuring element of size 5 x 5 pixels.

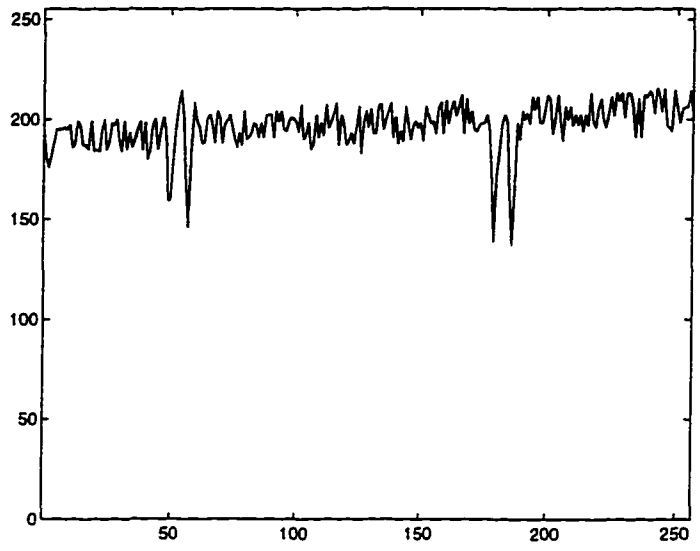

(a)

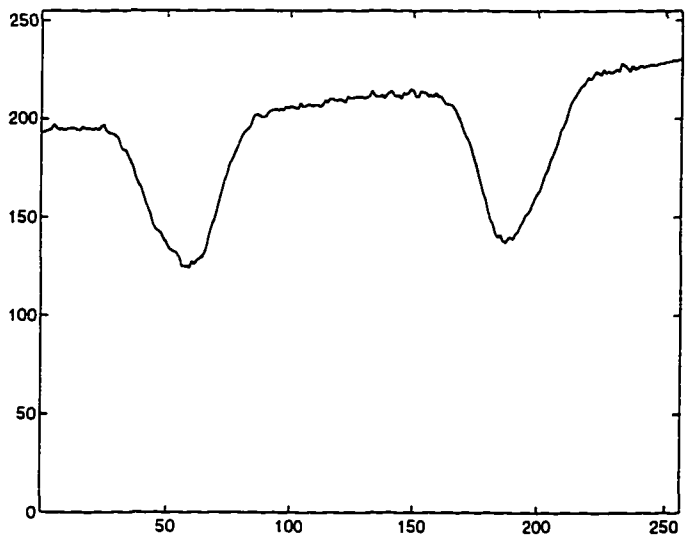

(b)

Figure 5.5. Line scans obtained from the original ultrasonic and eddy current images.

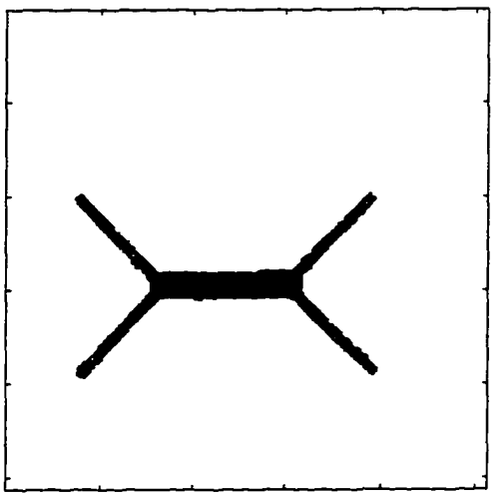

(a)

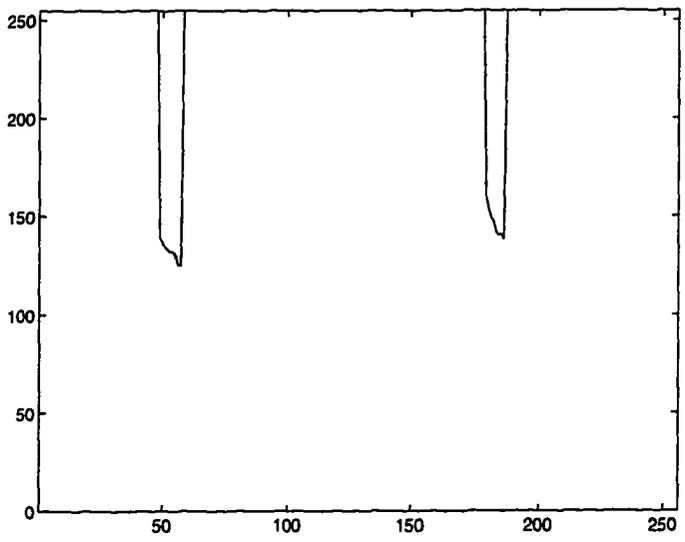

(b)

Figure 5.6. Fused image and line scan obtained from the image after using the proposed algorithm.

(a)

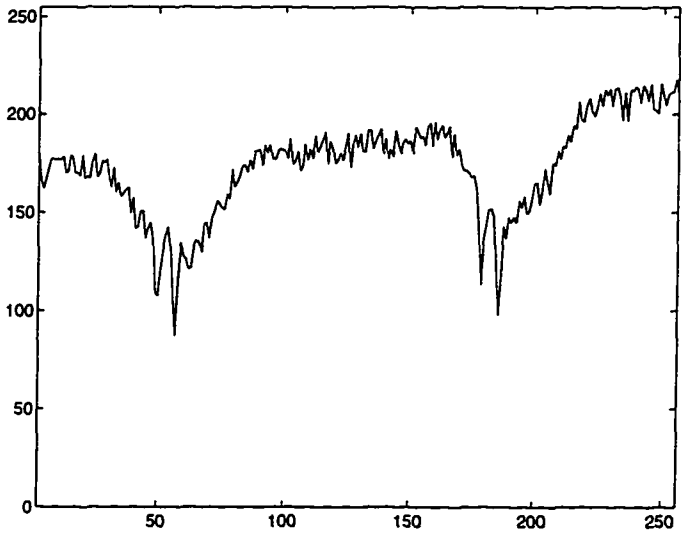

(b)

Figure 5.7. Fused image and line scan obtained from the image after using the multi-resolution decomposition technique employing LMMSE filters.

CHAPTER 6 SIMULATION RESULTS

This chapter presents simulation results obtained using a variety of experimentally derived data to demonstrate the effectiveness of the speckle noise reduction and data fusion algorithms described in chapters 4 and 5. The chapter begins with a description of the test specimens used for validating the speckle noise reduction algorithm. Next, simulation results obtained using conventional methods such as lowpass and median filters are presented for comparison. Following this, the images obtained using the proposed algorithm are shown. Details of the test specimens used for validating the new morphological data fusion algorithm are also shown. Finally, the fused images obtained from ultrasonic and eddy current images using the proposed algorithm are presented.

Results of the Proposed Speckle Noise Reduction Algorithm

Figure 6.1 shows diagrams of test specimens identified as "a", "b", "c", "d", "e", "f", "g" and "h". Specimen "a" consists of a 0.5 mm thick aluminum sample with approximately 0.1 mm deep numerals of 4 mm height and lines etched on it. Specimen "b" is similar to specimen "a" except that it is made from stainless steel and the patterns are 0.05 mm deep. Specimen "c" consists of a 6 mm thick aluminum sample with 0.5 mm deep numerals of 2 mm height and lines etched on it. Specimens "d" is similar to specimen "c" except that it is made from stainless steel and the patterns are 0.05 mm deep. Specimen "e" consists of a 6 mm thick aluminum sample with a 0.2 mm deep and 0.2 mm wide slot machined on it. Specimen "f" consists of a 6 mm thick stainless steel sample with a 1 mm deep, 0.2 mm wide and 1.3 mm

long slot machined on it. Specimen "g" consists of a rough surfaced 12 mm thick steel sample with a 2 mm diameter, 0.2 mm deep flat bottomed hole. Specimen "h" was obtained by gluing two 2.5 mm thick machined aluminum pieces with staircase type surfaces in a complementary manner.

Figure 6.2 shows the normal incidence ultrasonic acoustic microscopy images obtained using a 60 MHz focused transducer and a scanning step size of 40 μm. The C-scan images of size 256 x 256 pixels were used for validating the algorithm described in chapter 4. Images shown in Figures 6.2(a) through (h) correspond to the specimens shown in Figures 6.1(a) through (h), respectively. The scan area of each image is 10.24 x 10.24 mm^2.

Figures 6.3(a) through (h) show the spectra of the original ultrasonic images shown in Figures 6.2(a) through (h), respectively. The lowpass filtered images shown in Figures 6.4(a) through (h) were obtained from images shown in Figures 6.2 using 2nd order Butterworth filters. The cutoff frequencies of the Butterworth filters correspond to the cutoff radii equal to 100, 110, 110, 100, 50, 40, 60, and 60 enclosing 92.5, 96.4, 94.2, 94.7, 97.4, 97.9, 93.4 and 81.7 percent of the image power, respectively.

Figures 6.5(a) through (h) show the corresponding median filtered images using a window size of 5x5 pixels. The simulation results shown in Figures 6.4 and 6.5 demonstrate that conventional lowpass and median filtering techniques are not effective for reducing speckle noise while preserving the shapes of thin features. The algorithm described in chapter 4 was implemented using flat symmetric square-type structuring elements.

Figures 6.6(a) through (h) show the speckle noise reduced images obtained using the algorithm described in chapter 4. In contrast to the results obtained using lowpass and median

filters, the results shown in Figure 6.6 demonstrate that the proposed algorithm is capable of reducing speckle noise very effectively while preserving the desired features.

Results of the Proposed Data Fusion Algorithm

The new morphological data fusion algorithm was evaluated using ultrasonic and eddy current images obtained from the six test specimens. The test specimens identified as "A", "B", "C", "D", "E" and "F" as shown in Figures 6.7(a) through (f), respectively. Specimen "A" consists of a 0.5 mm thick stainless steel sample with 0.05 mm deep and 0.1 mm wide numerals and lines etched on it. Specimen "B" is similar to specimen "A" except that it contains different character and line patterns. Specimen "C" consists of a 6 mm thick aluminum plate containing a 2.5 mm deep and 0.5 mm wide slot. Specimen "D" is similar to specimen "C" except that it contains an 1 mm deep and 0.2 mm wide slot. Specimen "E" is the same as the specimen shown in Figure 6.1(g). Specimen "F" consists of a 0.5 mm thick aluminum sample with 0.1 mm deep and 0.2 mm wide characters "SC" and "IU" on the front and back wall, respectively and lines etched on both sides. As described in chapter 2, eddy current NDE test methods are effective in detecting flaws near the surface of the conductive test material. Ultrasonic test methods are capable of detecting flaws that are embedded deep in the specimen. It may be argued that additional information can be gained by combining information from the ultrasonic and eddy current images. This premise was verified using specimen "F". Figures 6.8 and 6.9 show the corresponding 256 x 256 size ultrasonic and eddy current images that were used for validating the data fusion algorithm. The ultrasonic images were obtained using a 60 MHz focused transducer while the eddy current images were

obtained using a Zetec© pencil-type eddy current probe (50-500 KHz) with the excitation frequency set at 200 KHz. A scanning step size of 40 μm was used to obtain the images shown in Figures 6.8 and 6.9.

Figure 6.10 shows the ultrasonic images obtained after reducing speckle noise. Flat symmetric square-type structuring elements were used in implementing the speckle noise reduction algorithm. Figures 6.11 and 6.12 show the granulometric size distributions and density functions obtained using iterative closing operations with a sequence of flat symmetric square-type structuring elements. As described in chapter 5, the variable along the horizontal axis in Figures 6.11 and 6.12 corresponds to the structuring element size. The results presented in Figures 6.11 and 6.12 show that the optimal sizes of the structuring elements for restoring the unidentified regions in ultrasonic images are 3x3, 3x3, 5x5, 3x3, 31x31 and 7x7 pixels, respectively. Figures 6.13(a) through (f) show the restored binary images, highlighting the defect regions which are not identified explicitly in the C-scan ultrasonic images. Figures 6.14(a) through (f) show the results obtained after fusing the corresponding ultrasonic and eddy current images. The fused images obtained using the proposed algorithm reveal the defect locations and their gray levels clearly.

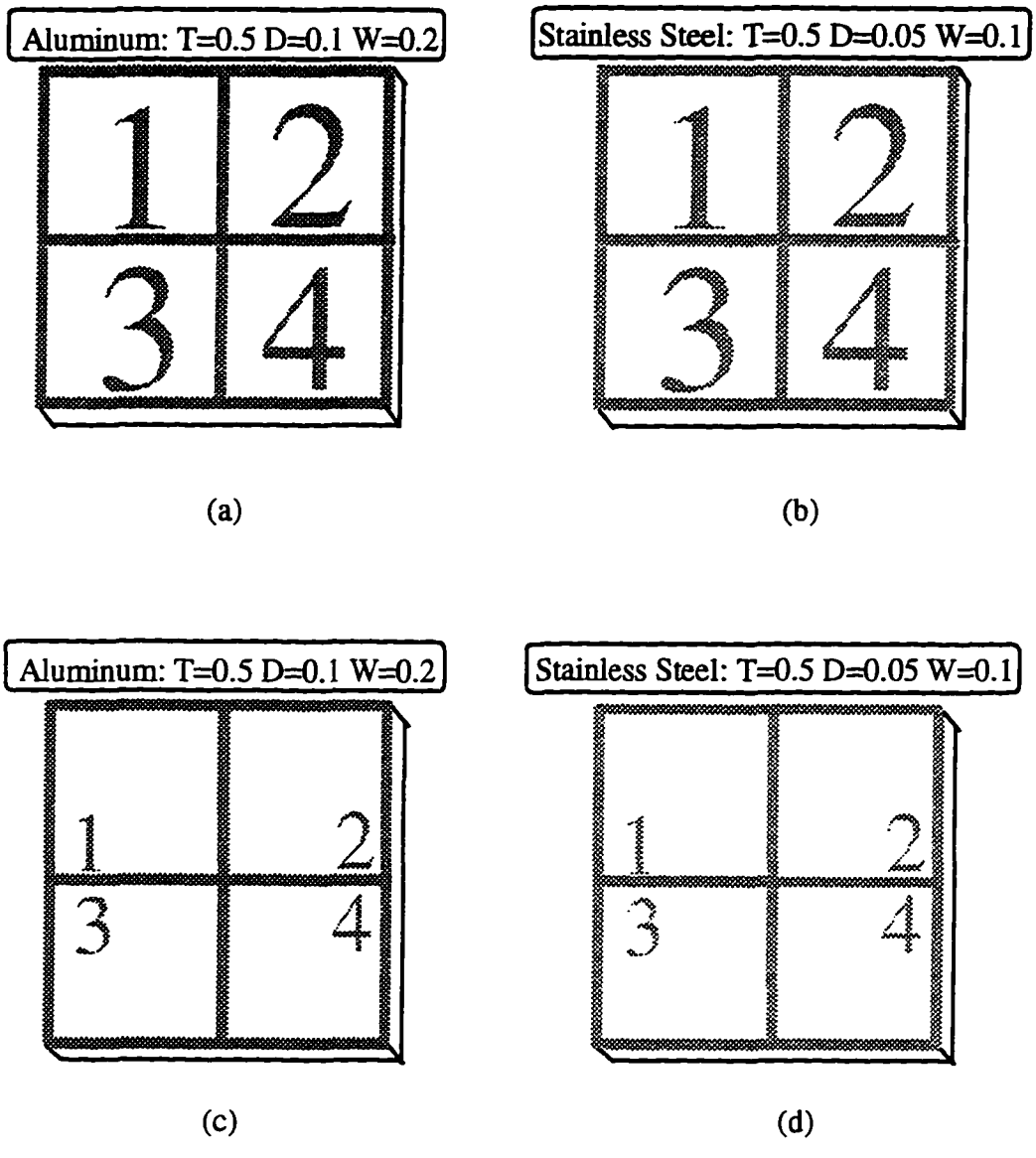

Figure 6.1. Details of the test specimens used for validating the proposed speckle noise reduction algorithm.

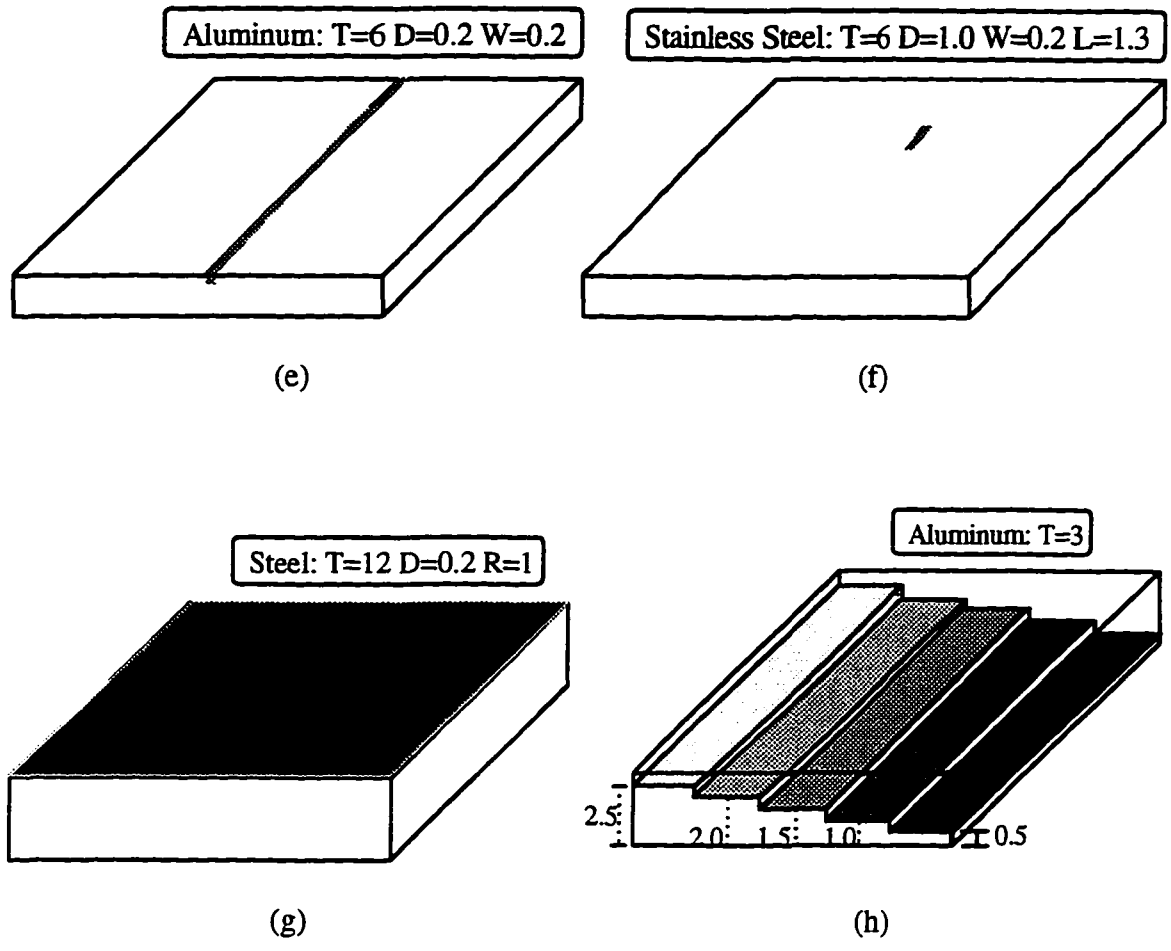

Figure 6.1. (Continued)

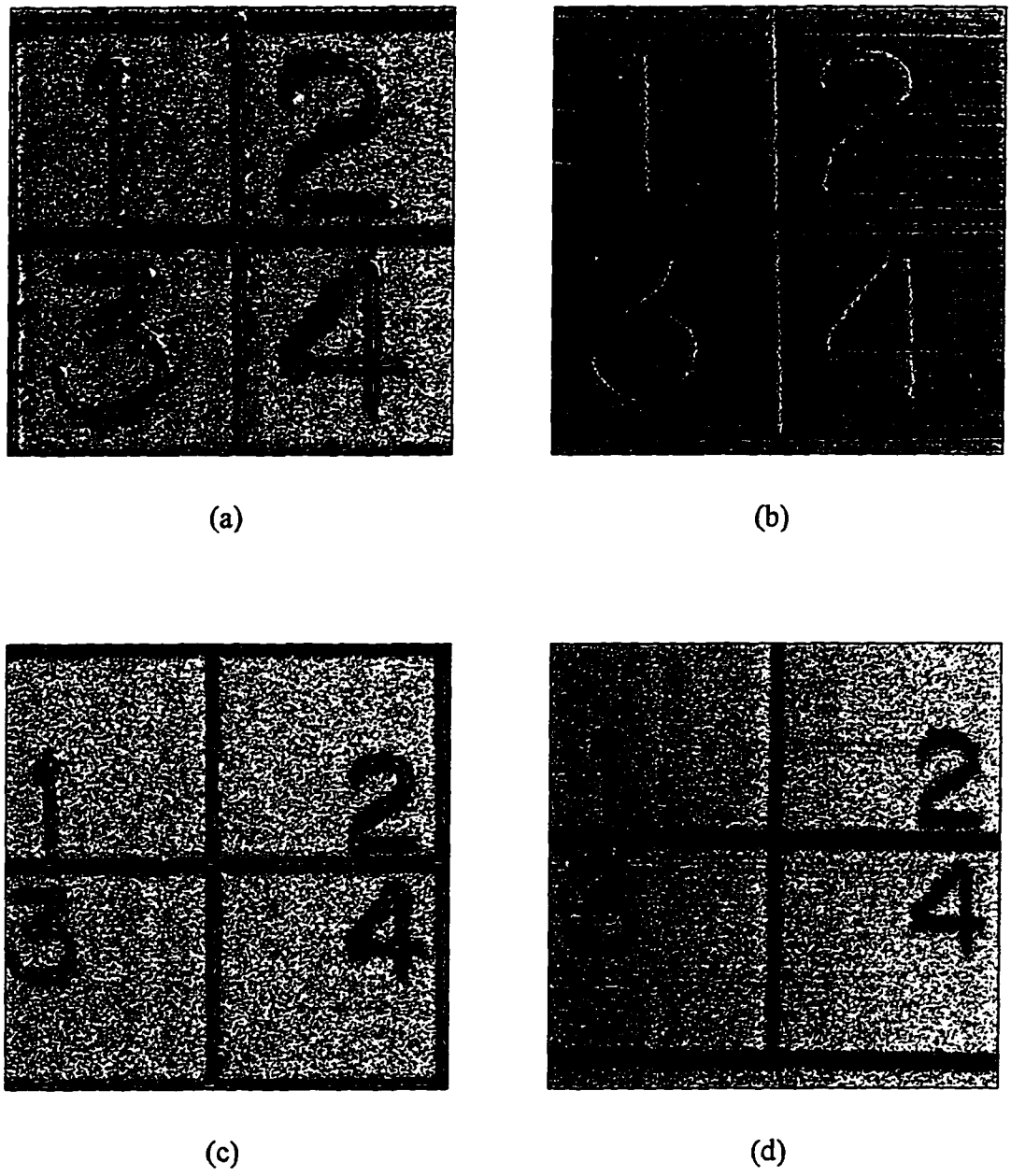

Figure 6.2. Original C-scan ultrasonic images obtained from the specimens shown in Figure 6.1.

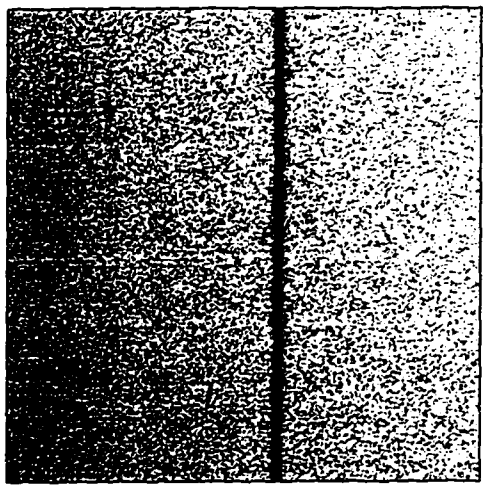

(e)

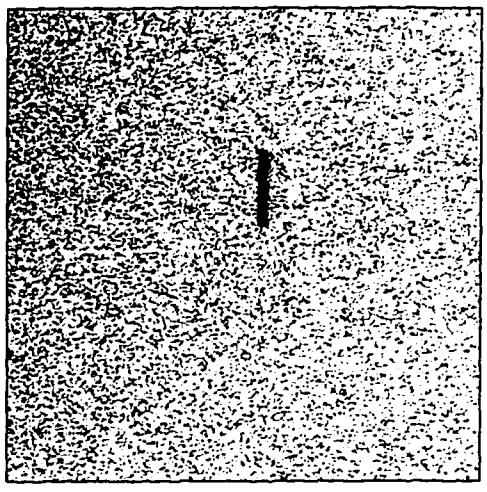

(f)

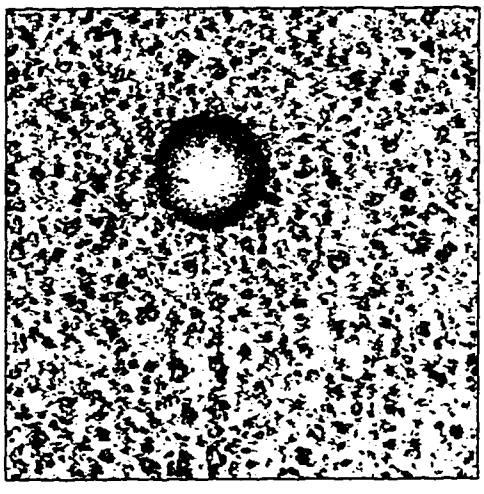

(g)

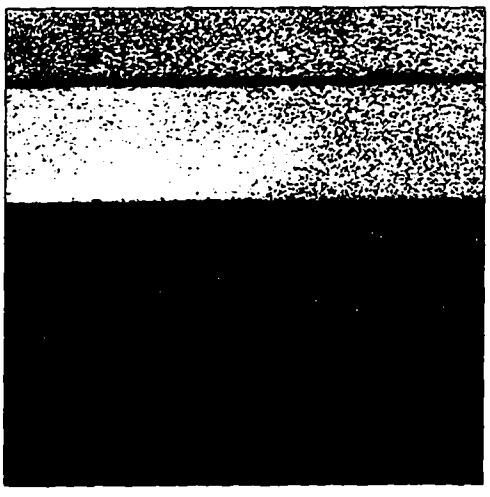

(h)

Figure 6.2. (Continued)

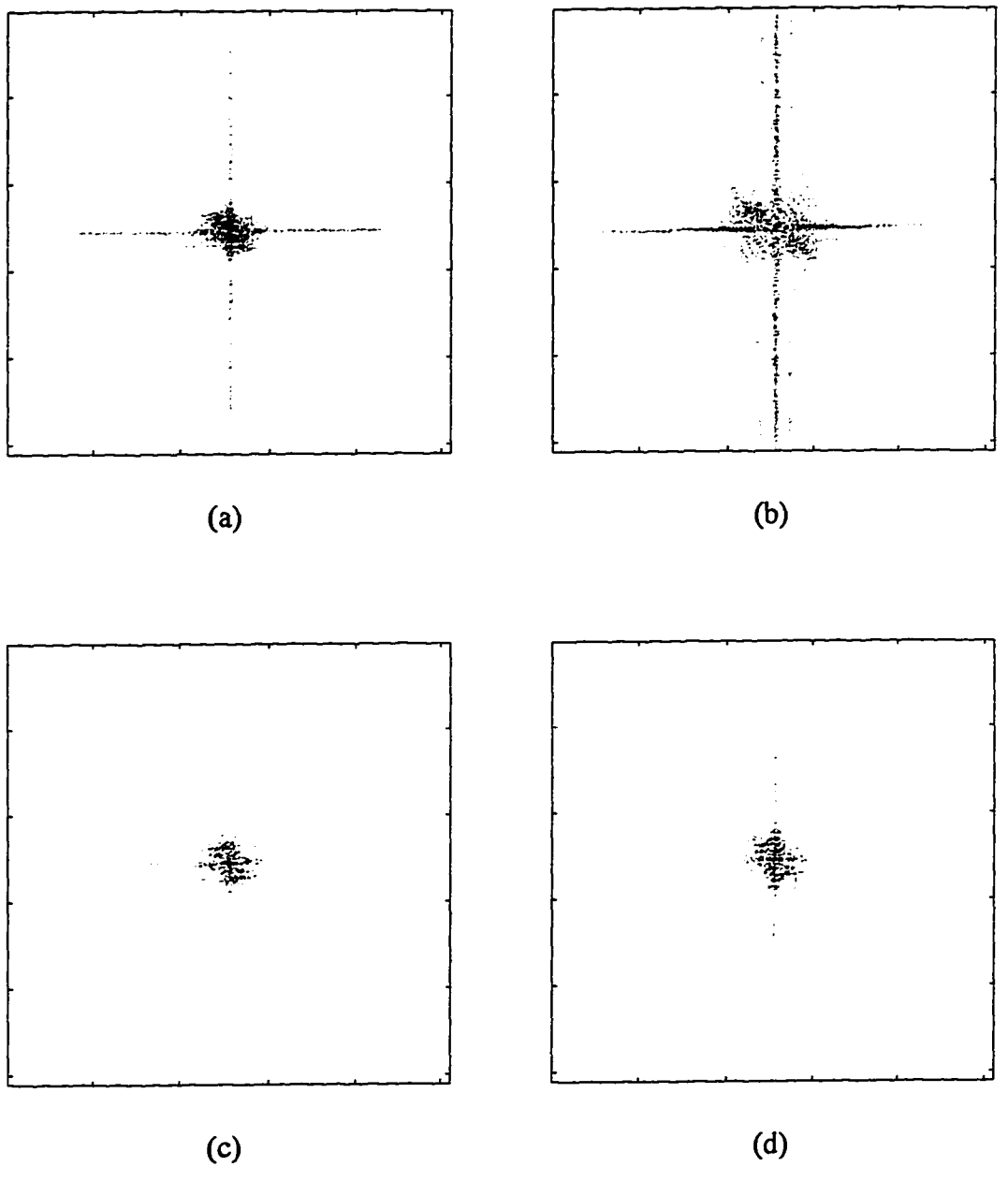

Figure 6.3. Fourier spectra of the ultrasonic images shown in Figure 6.2.

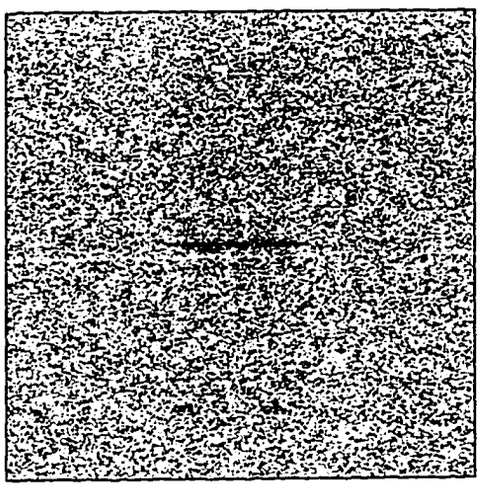

(e)

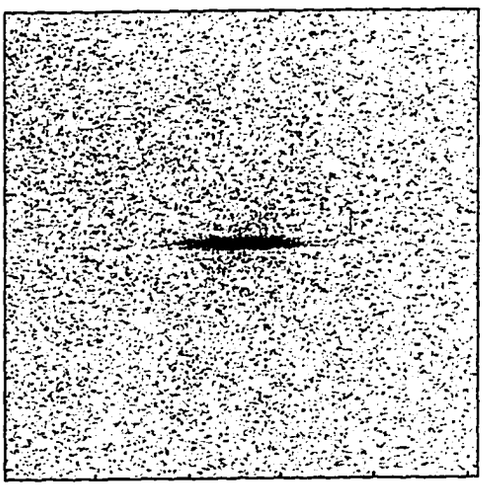

(f)

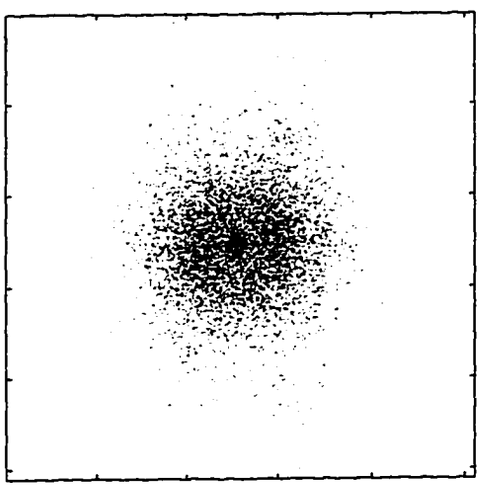

(g)

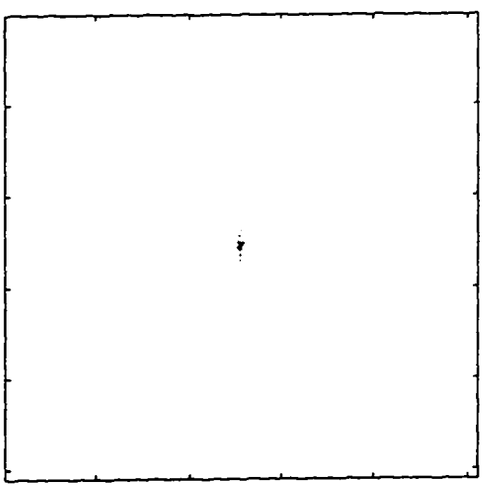

(h)

Figure 6.3. (Continued)

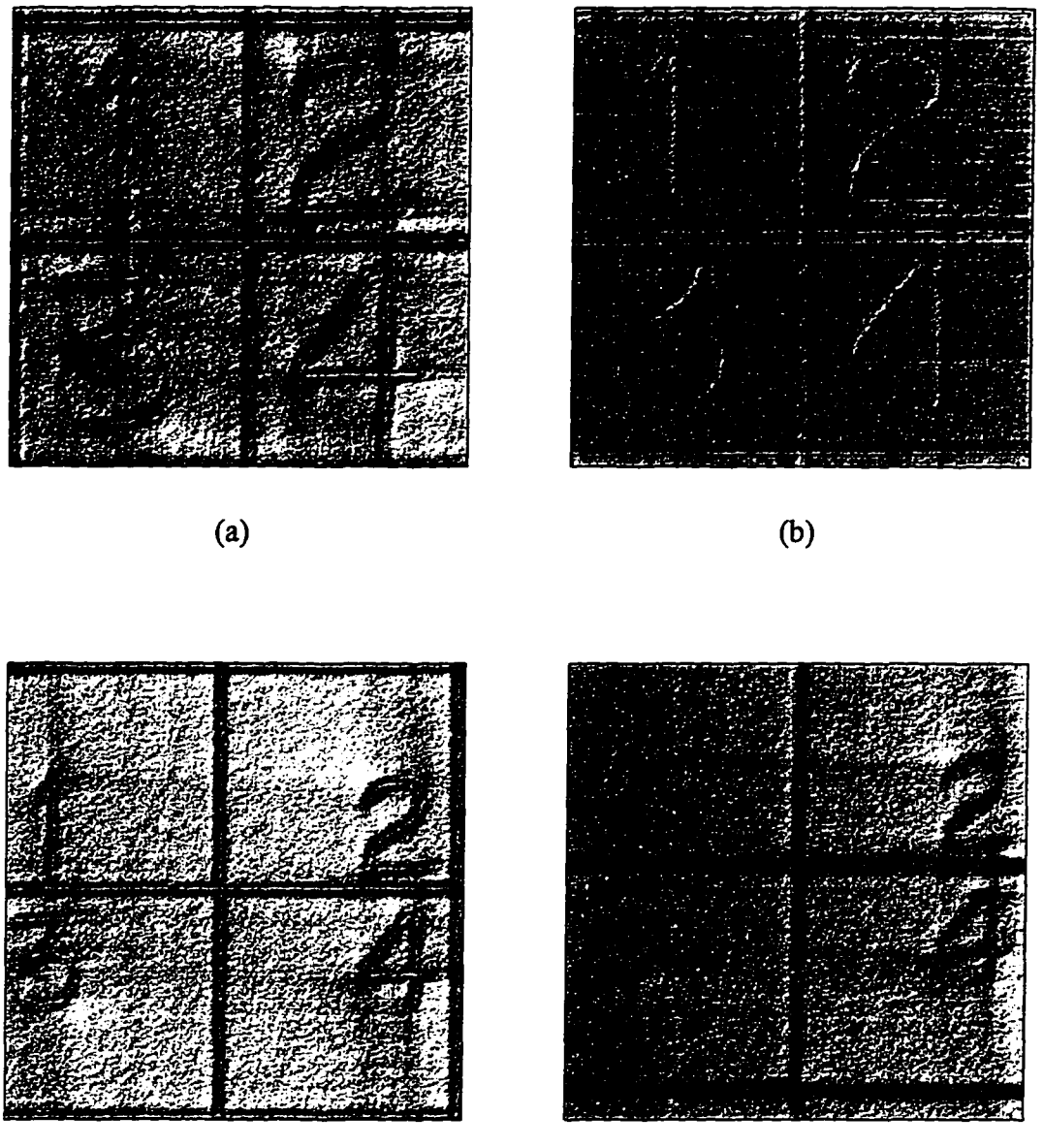

(a) (b)

(c) (d)

Figure 6.4. Lowpass filtered images. Original images are shown in Figure 6.2.

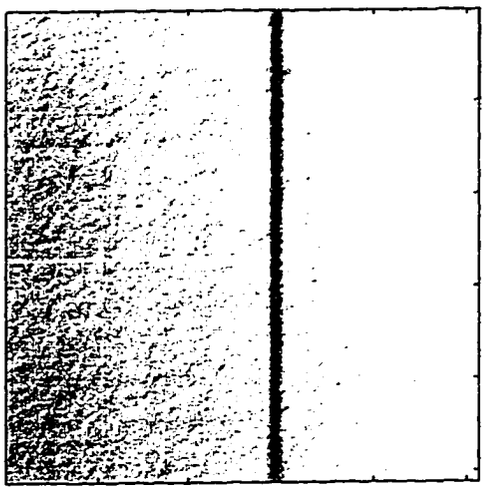

(e)

(f)

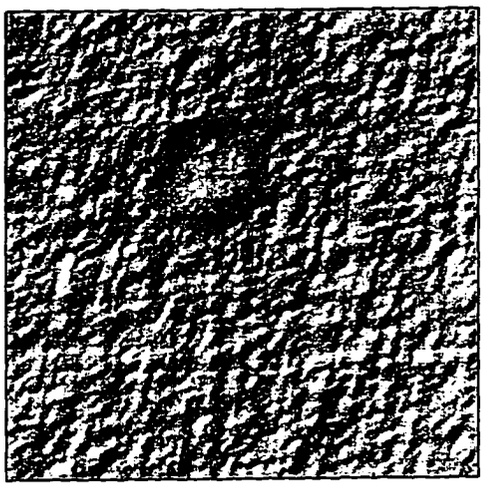

(g)

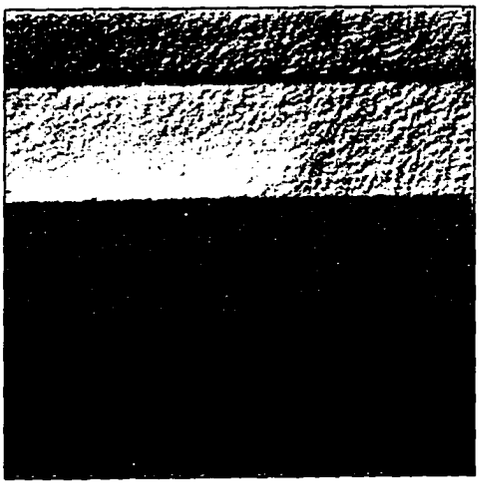

(h)

Figure 6.4. (Continued)

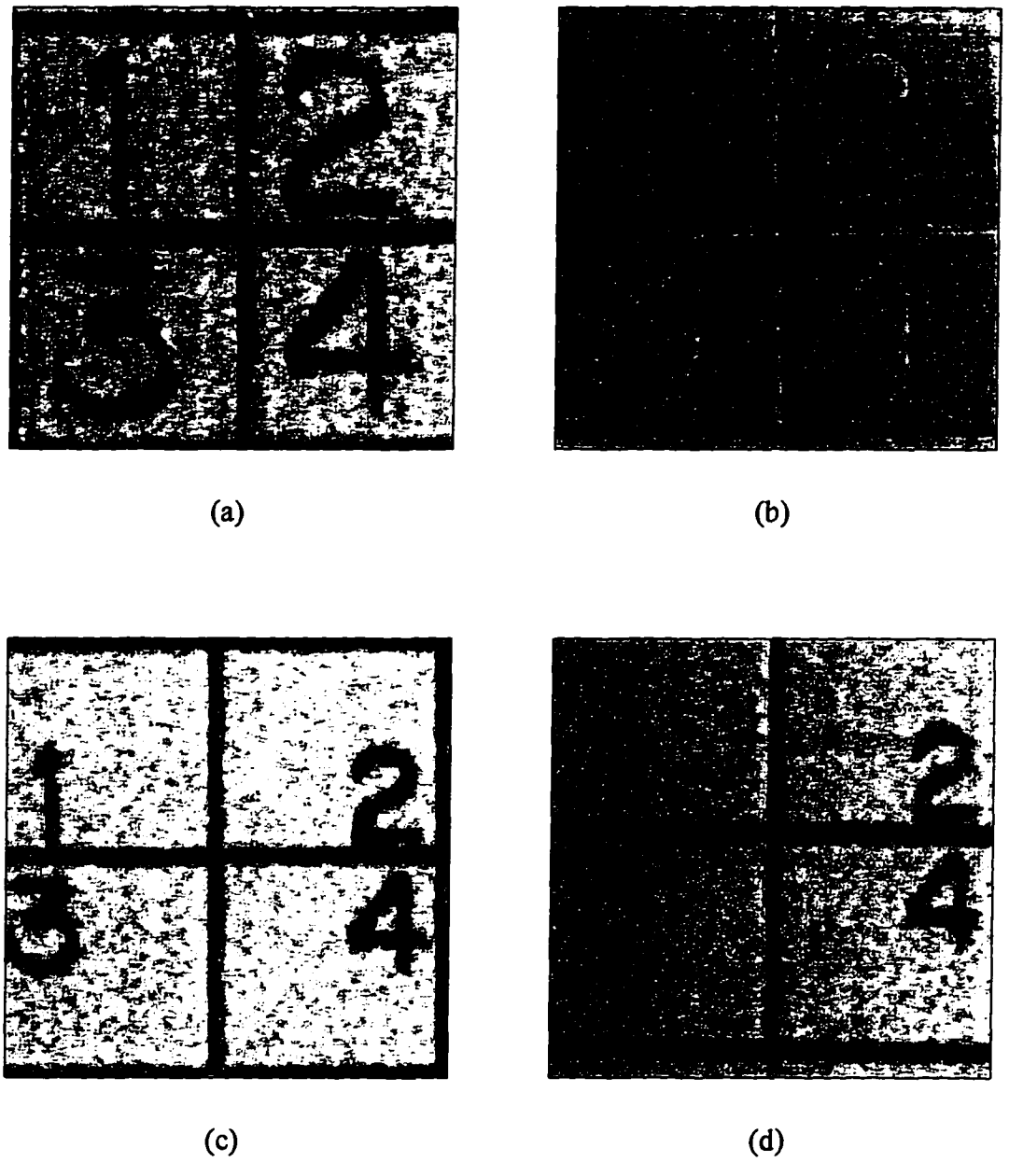

Figure 6.5. Median filtered images. Original images are shown in Figure 6.2.

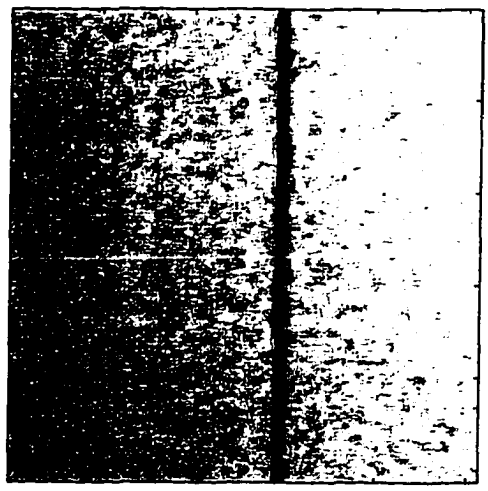

(e)

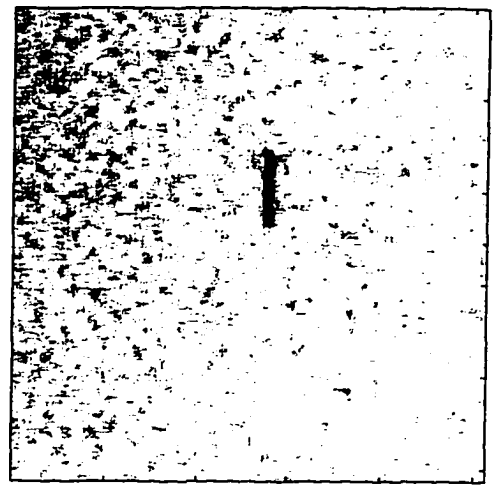

(f)

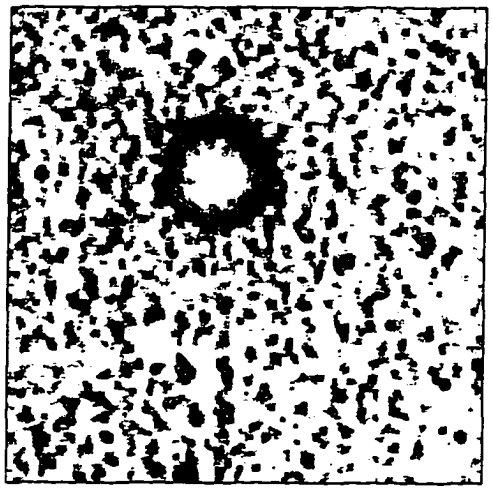

(g)

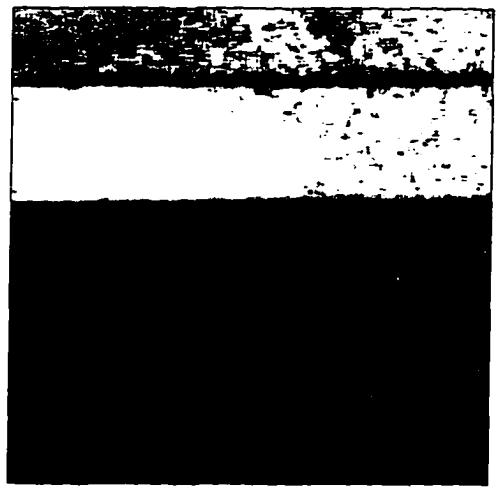

(h)

Figure 6.5. (Continued)

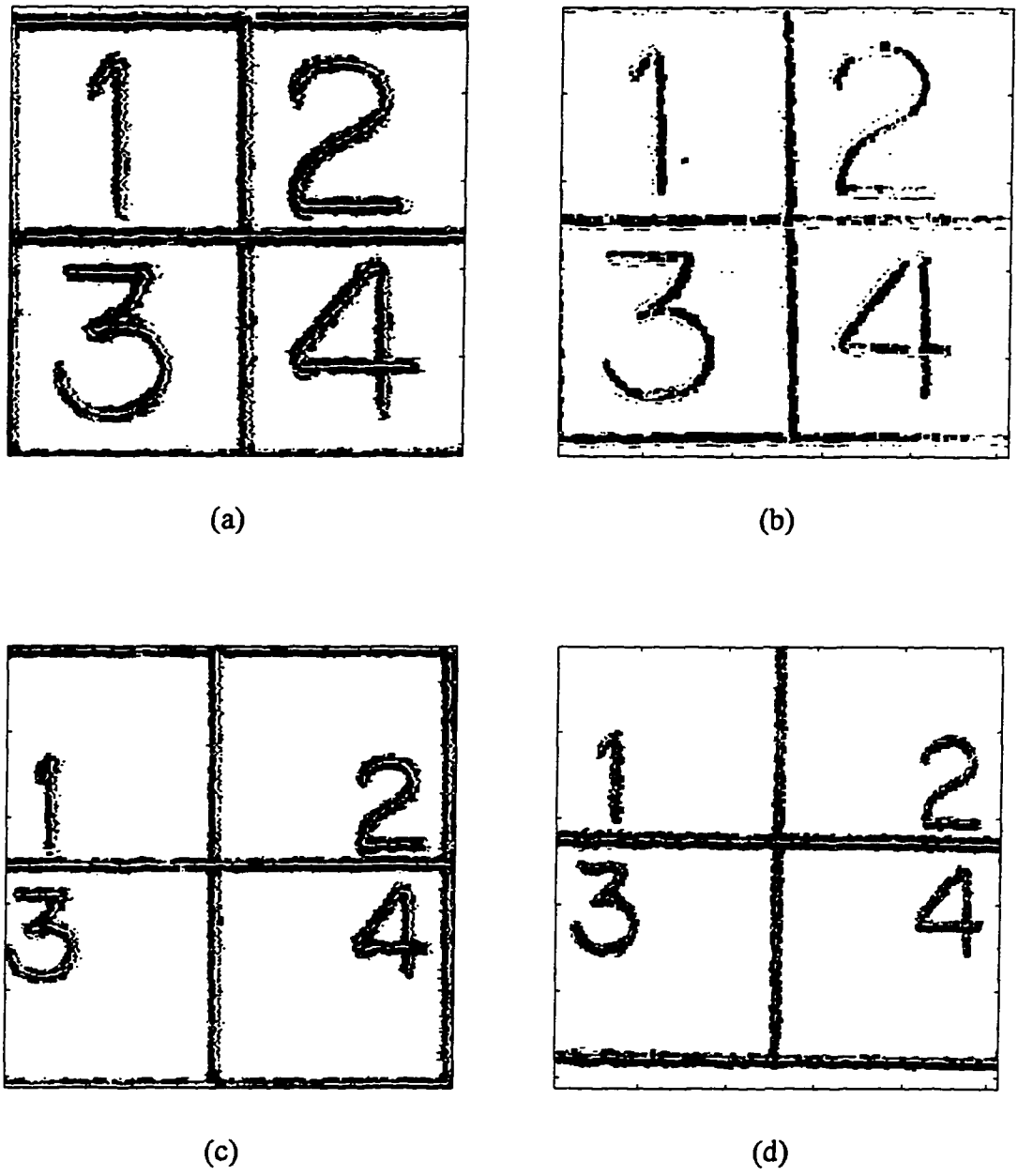

Figure 6.6. Speckle noise reduced images obtained using the proposed algorithm. Original images are shown in Figure 6.2.

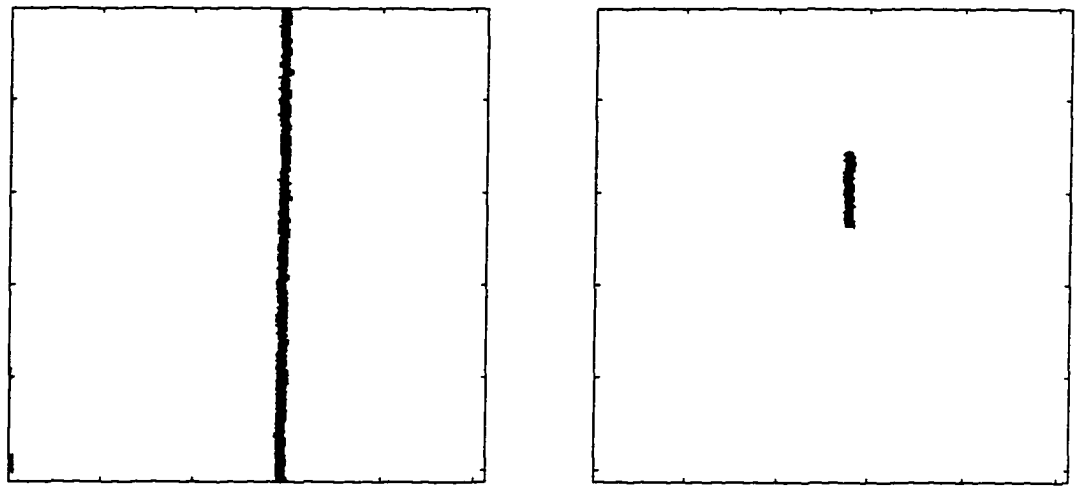

(e) (f)

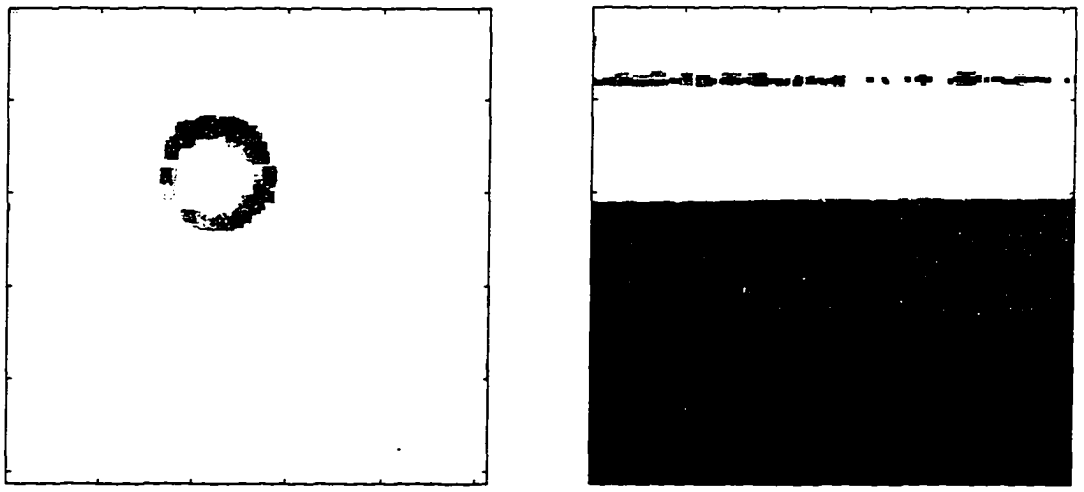

(g) (h)

Figure 6.6. (Continued)

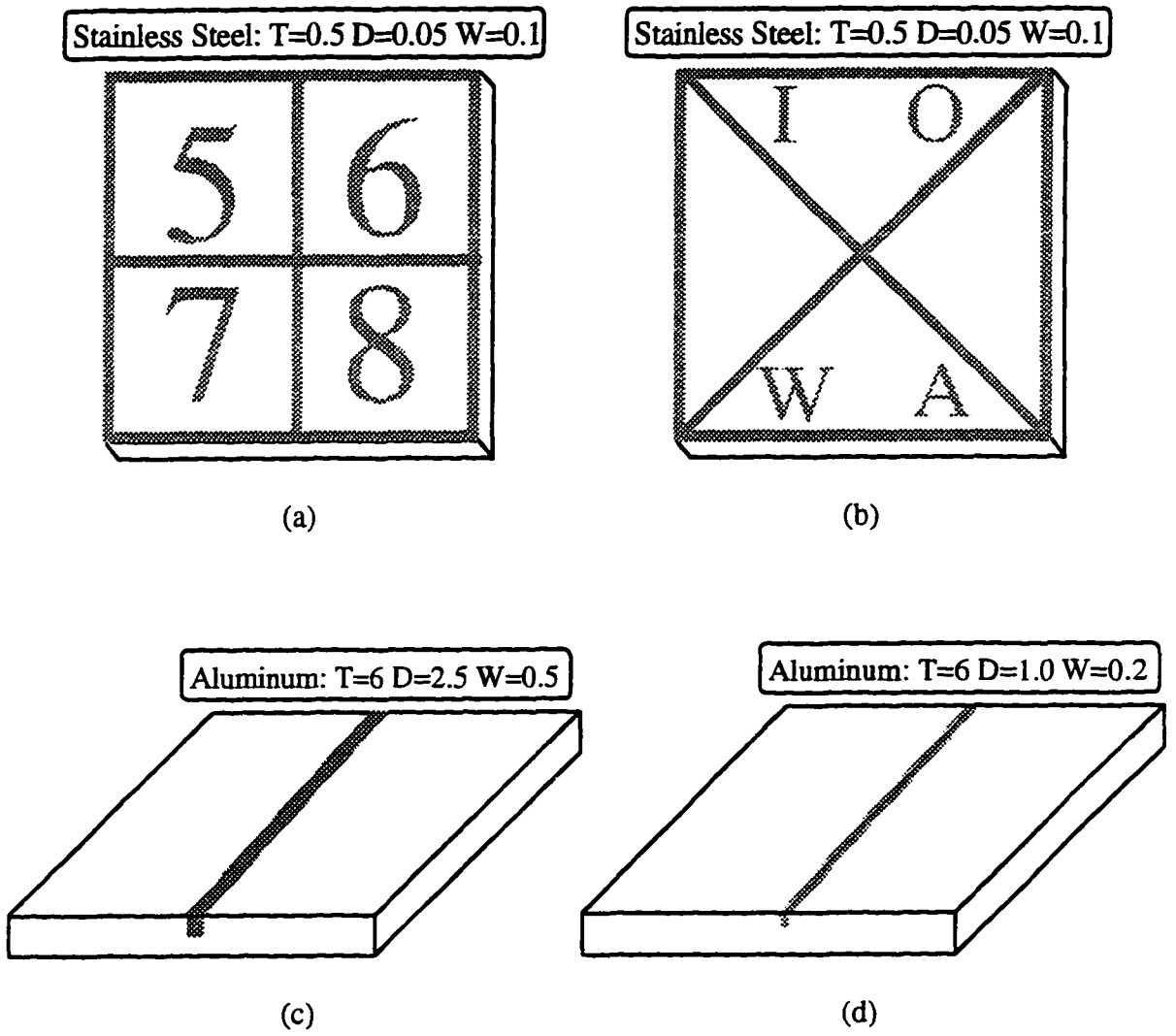

Figure 6.7. Details of the test specimens used for validating the proposed NDE data fusion algorithm.

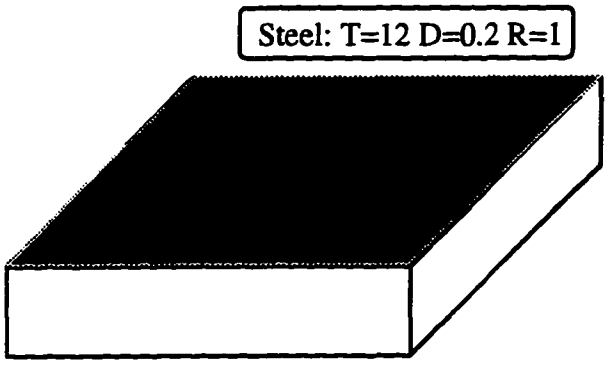

(e)

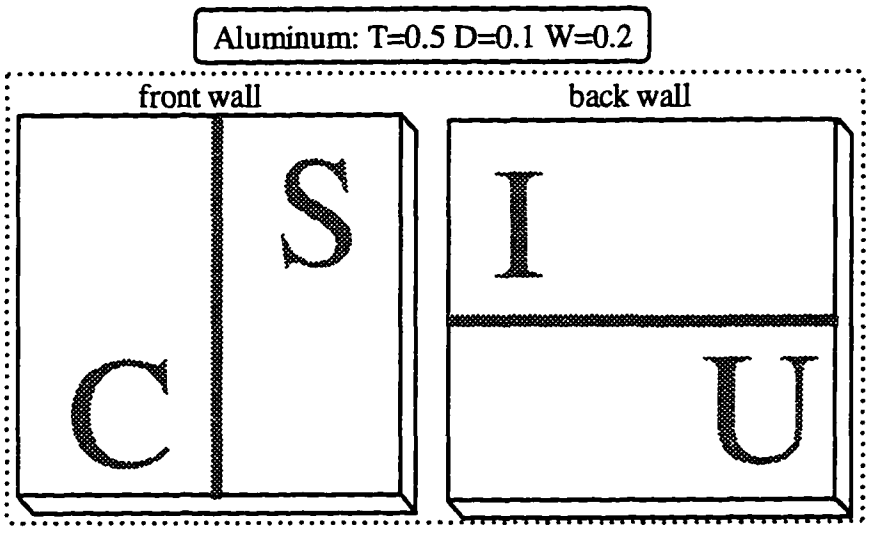

(f)

Figure 6.7. (Continued)

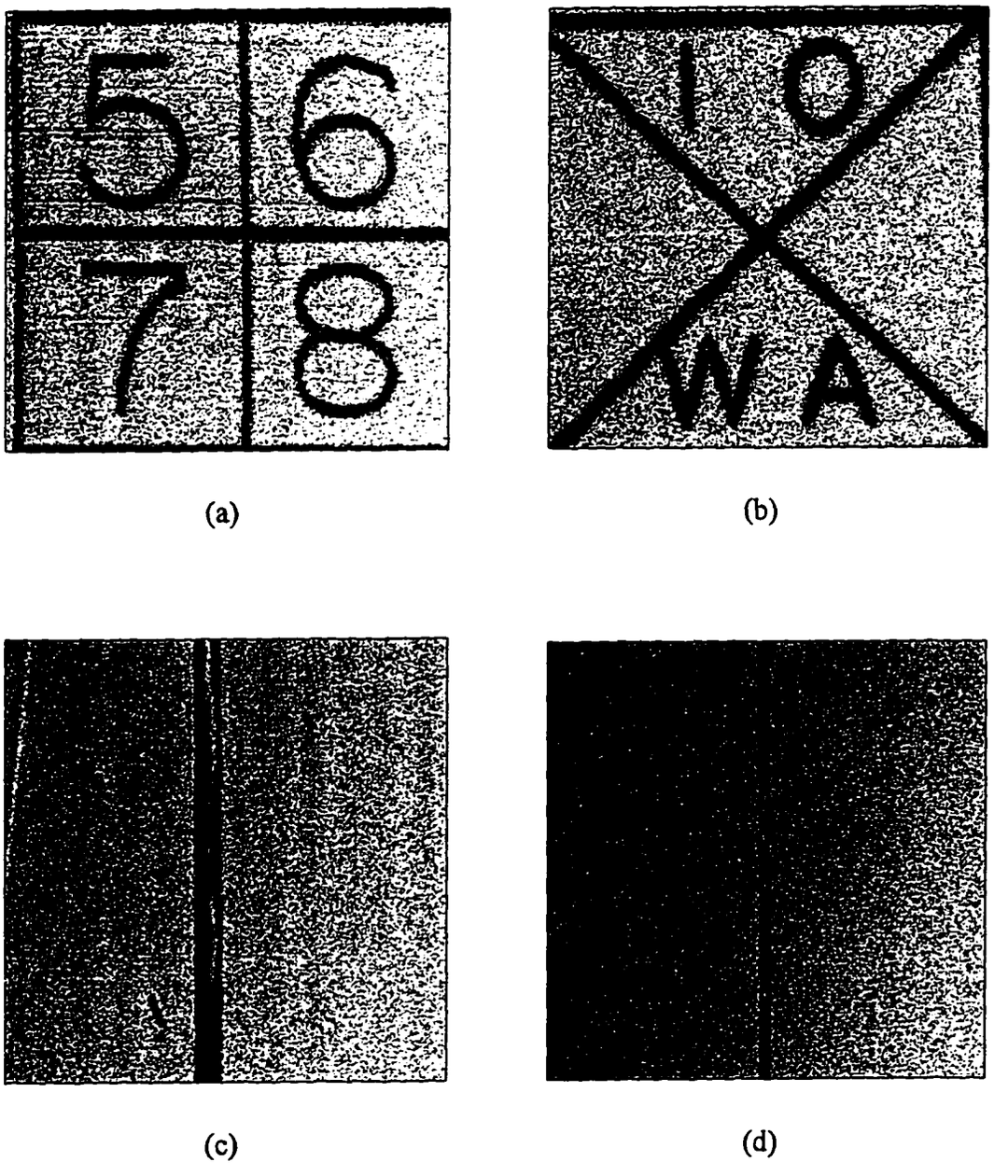

(a) (b)

(c) (d)

Figure 6.8. Original C-scan ultrasonic images.

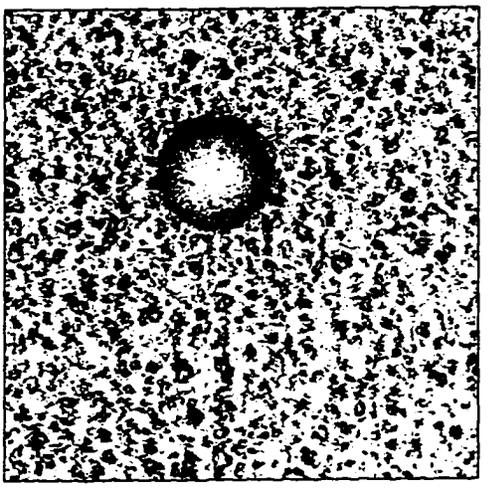

(e)

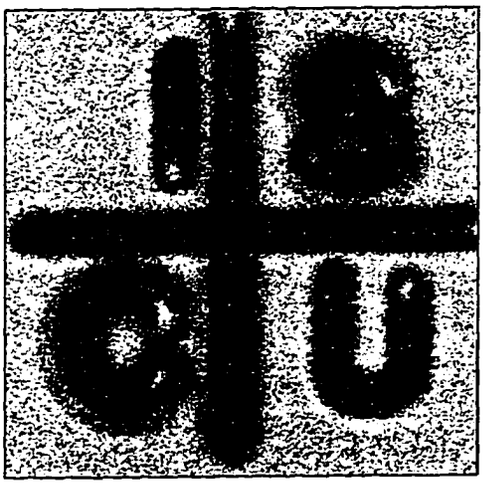

(f)

Figure 6.8. (Continued)

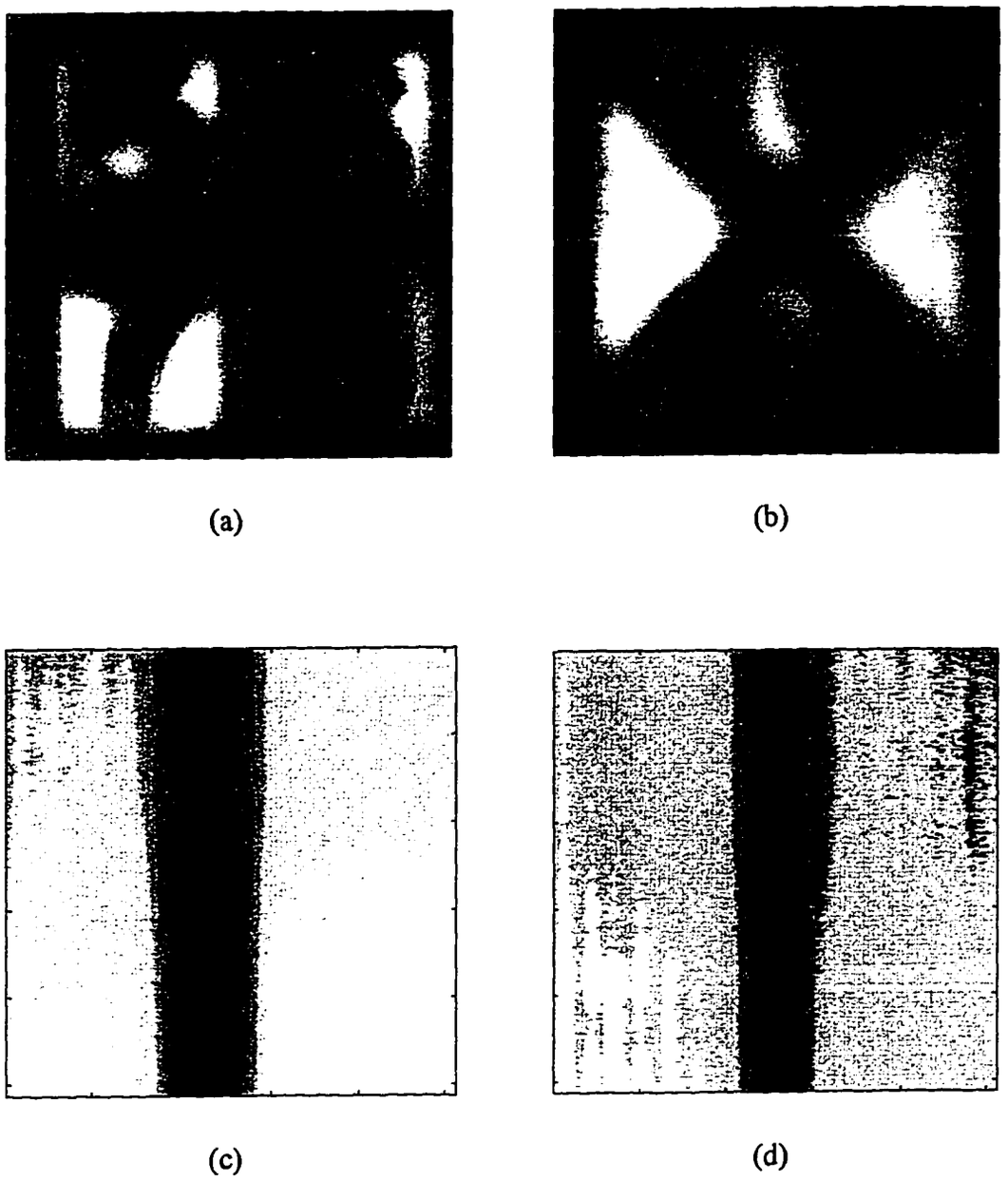

Figure 6.9. Original eddy current images.

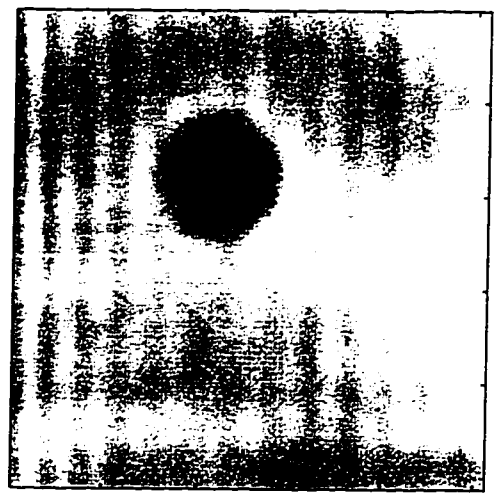

(e)

(f)

Figure 6.9. (Continued)

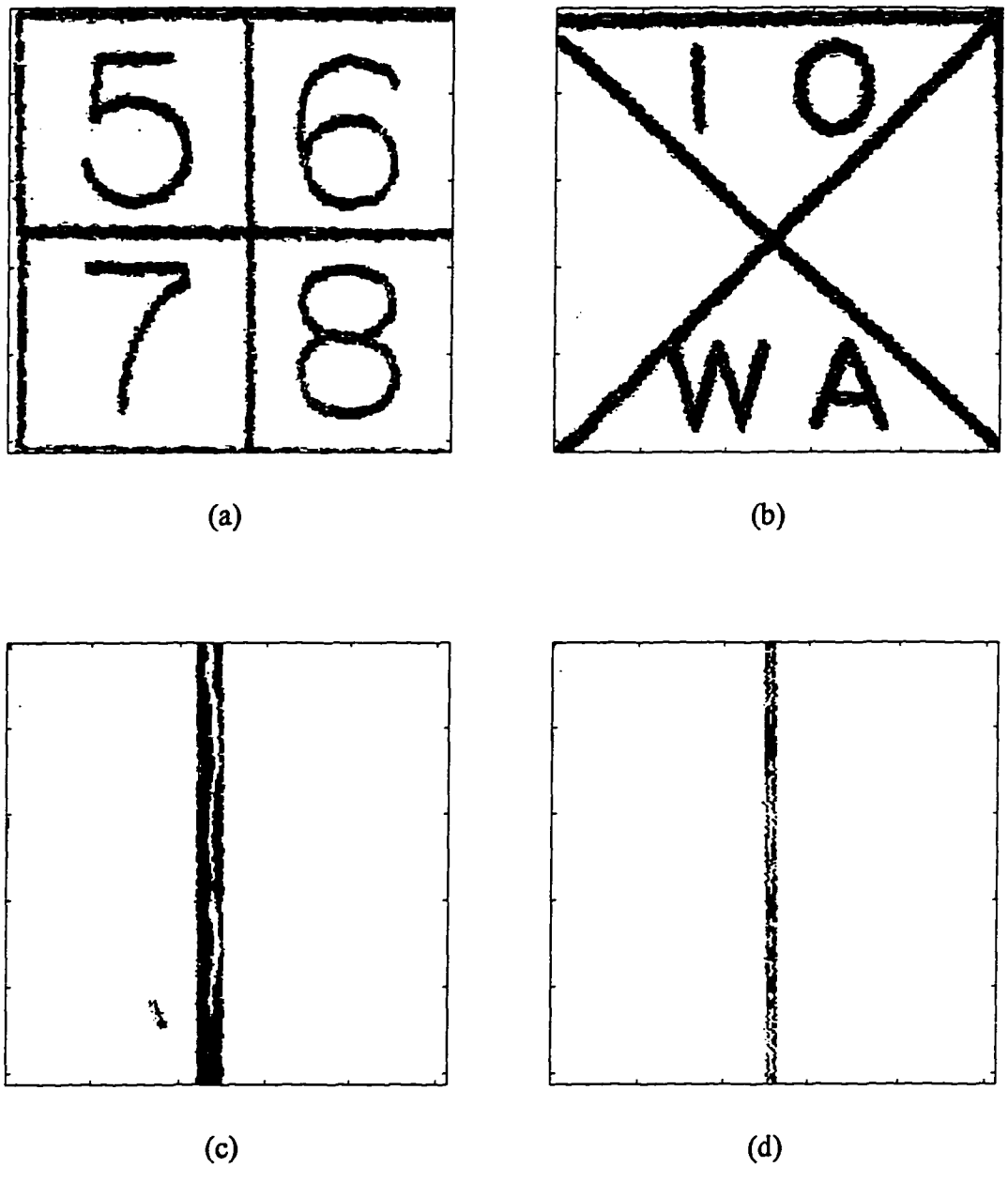

Figure 6.10. Speckle noise reduced images obtained using the proposed speckle noise reduction algorithm.

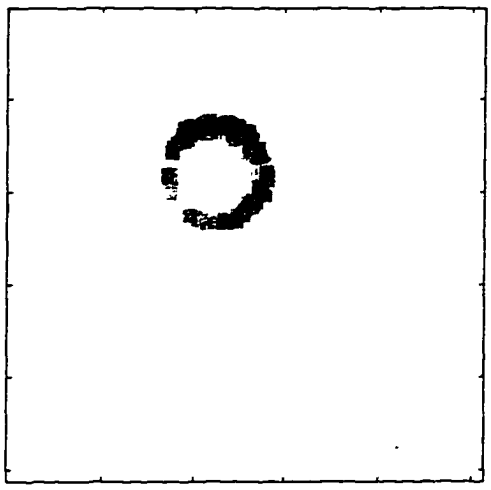

(e)

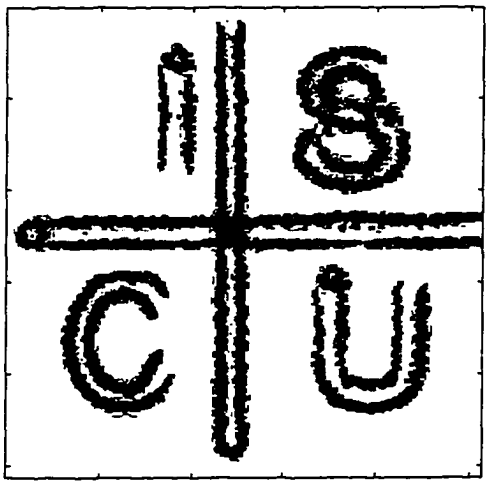

(f)

Figure 6.10. (Continued)

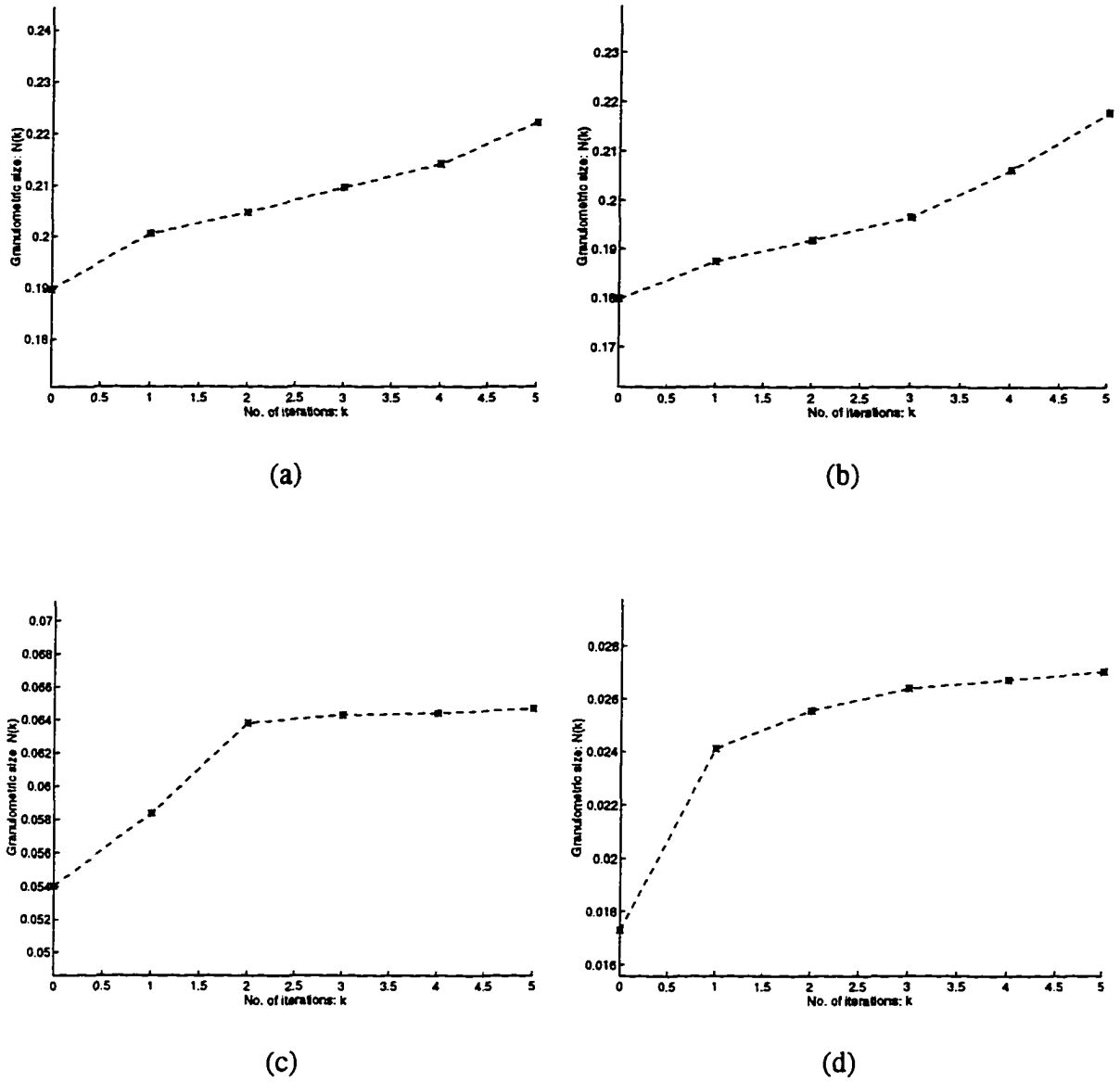

Figure 6.11. Granulometric size distributions of the images obtained using iterative closing operations.

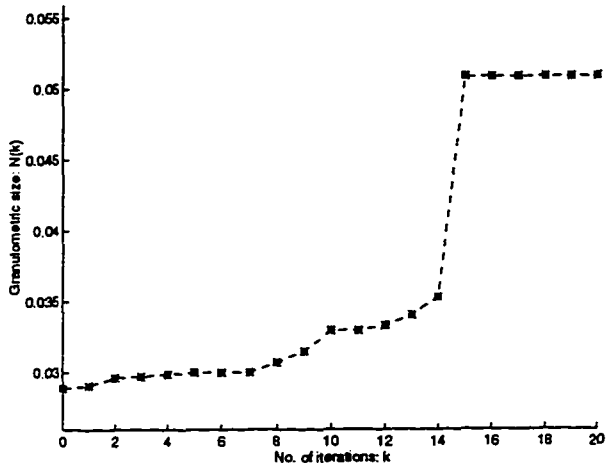

(e)

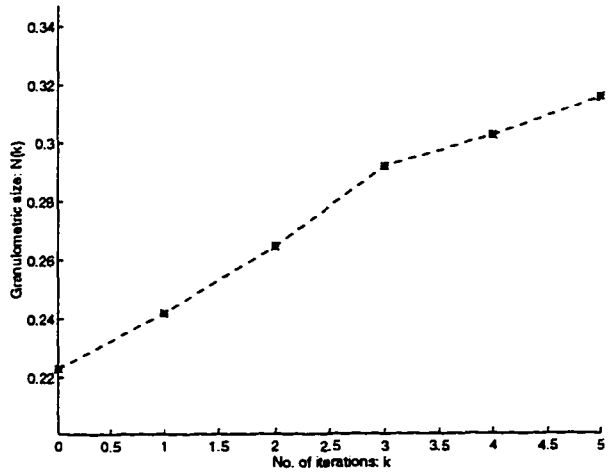

(f)

Figure 6.11. (Continued)

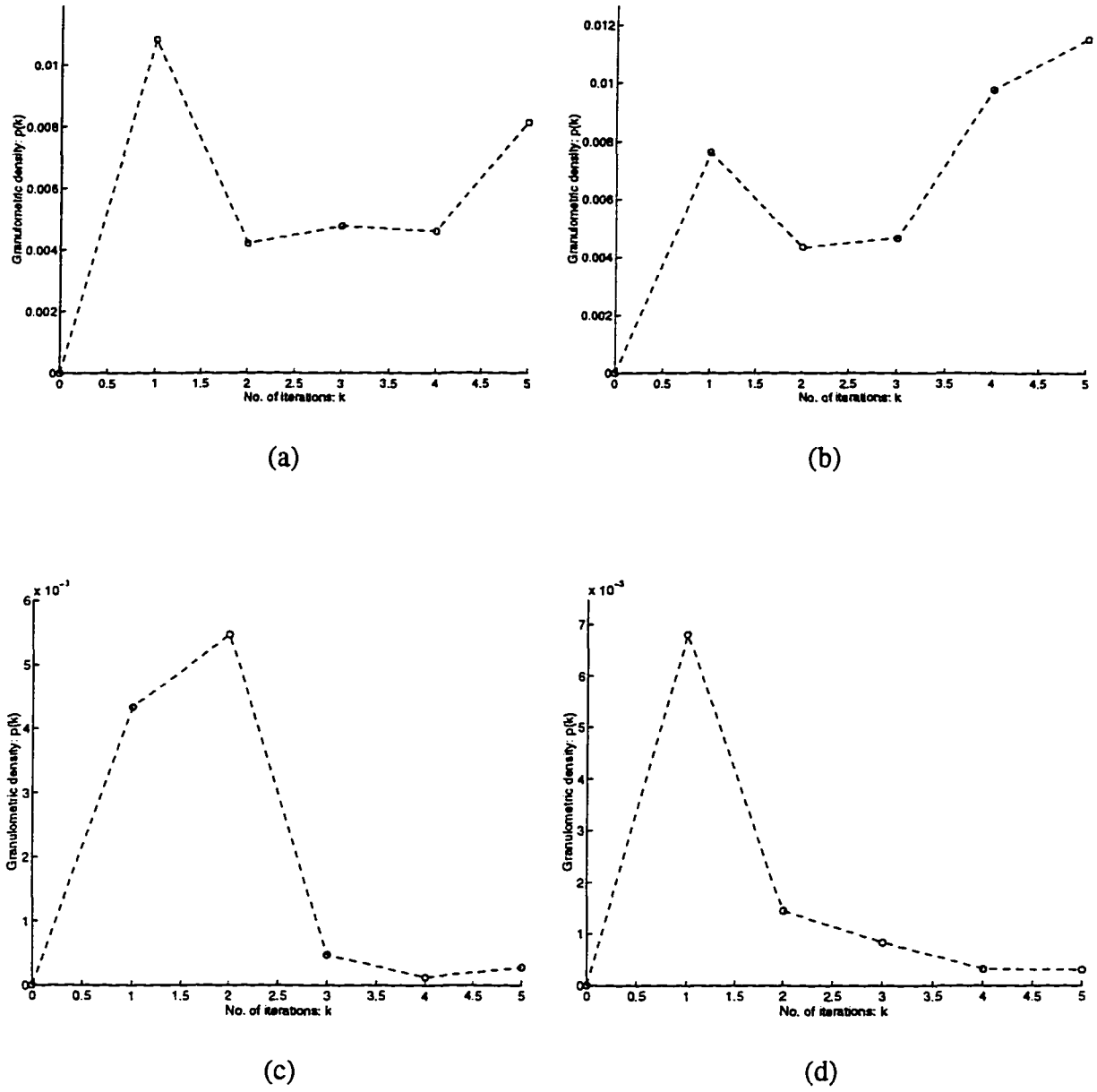

Figure 6.12. Granulometric size densities obtained using the granulometric size distributions shown in Figure 6.11.

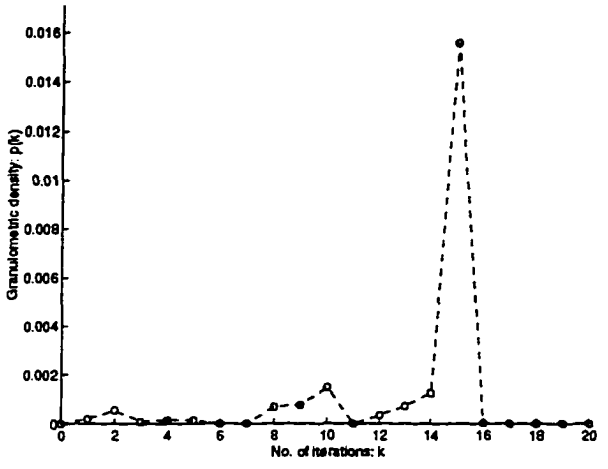

(e)

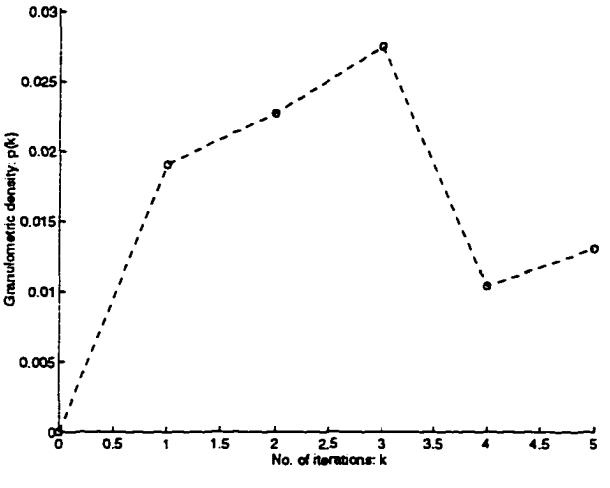

(f)

Figure 6.12. (Continued)

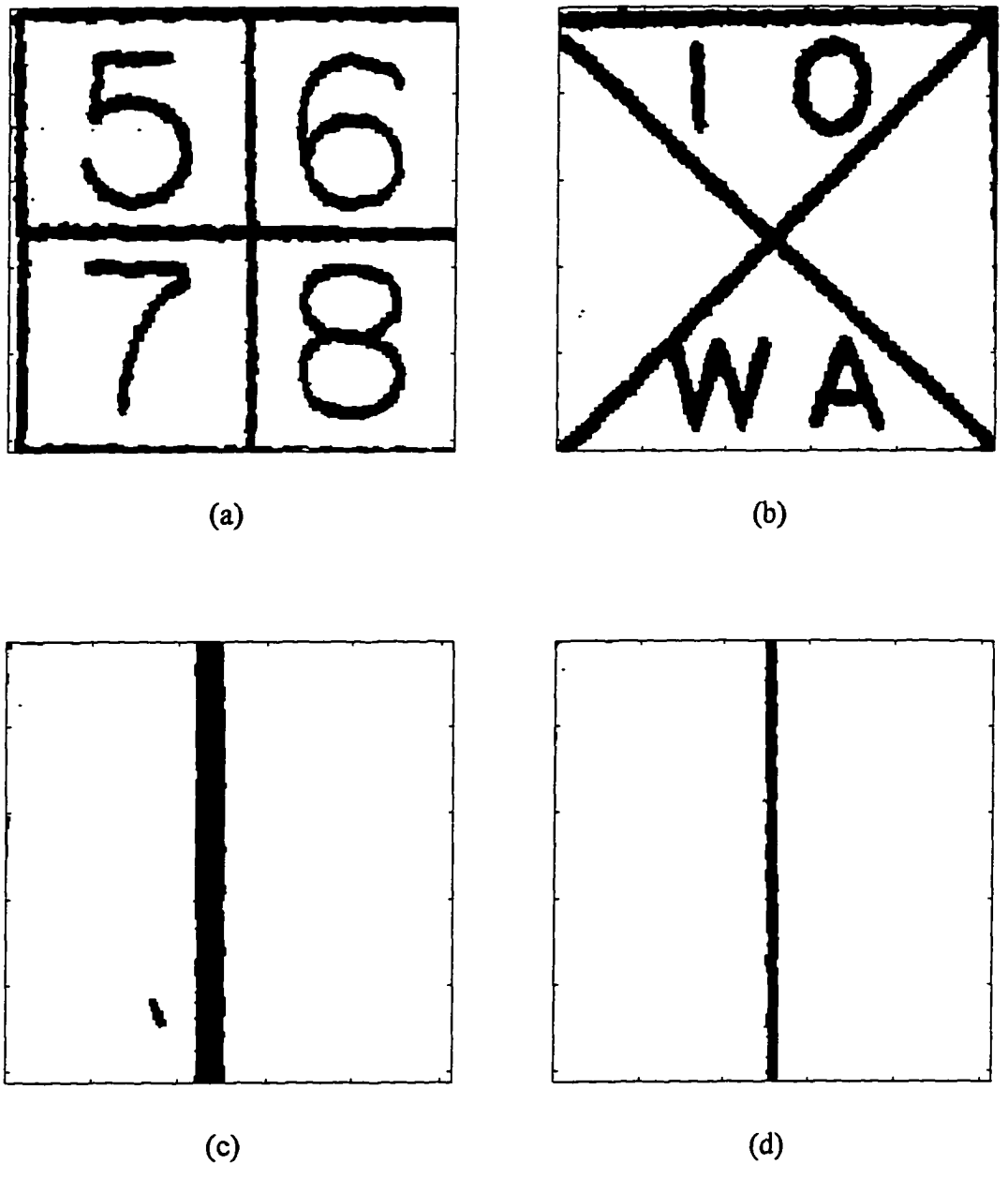

(a) (b)

(c) (d)

Figure 6.13. Restored binary images.

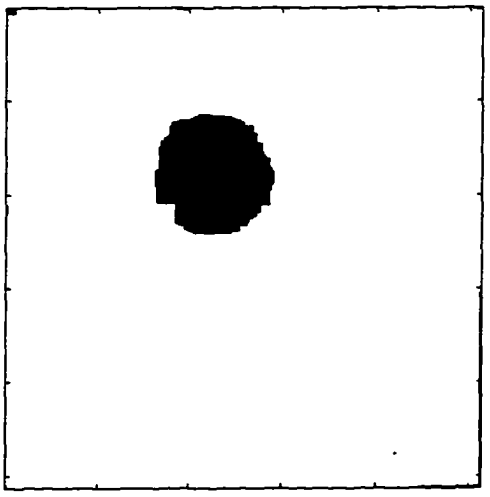

(e)

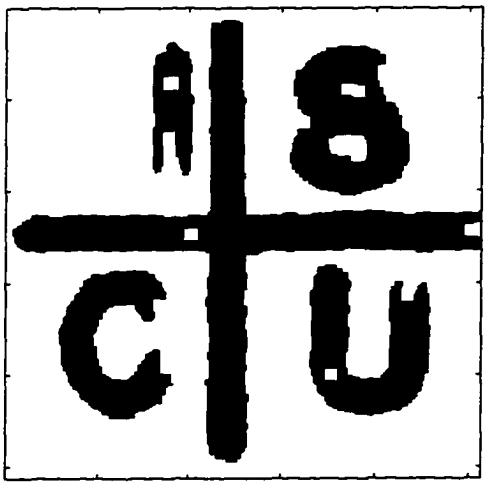

(f)

Figure 6.13. (Continued)

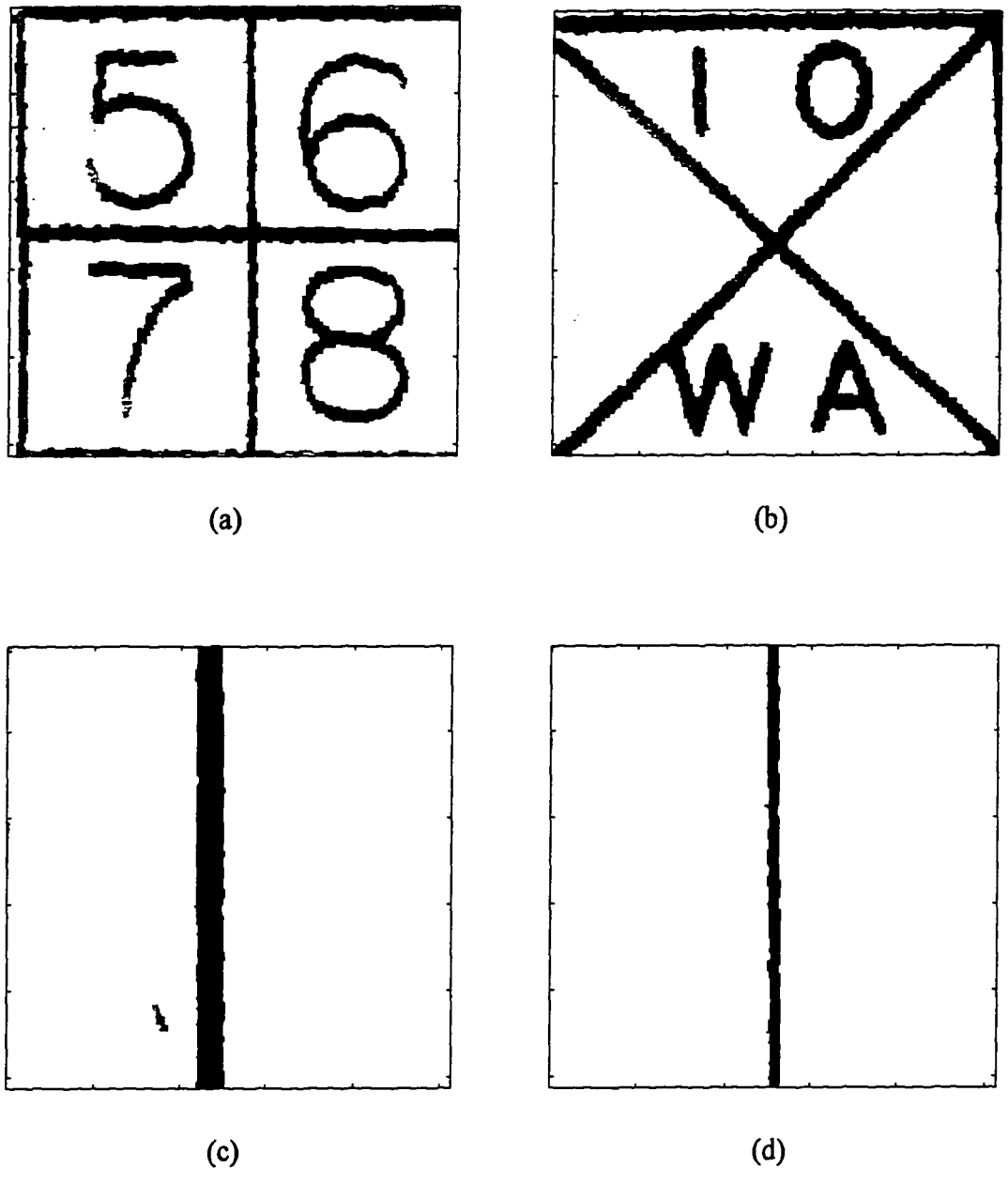

Figure 6.14. Fused images obtained using the proposed NDE data fusion algorithm.

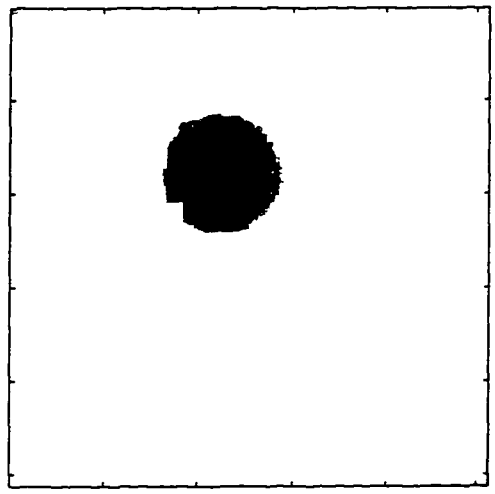

(e)

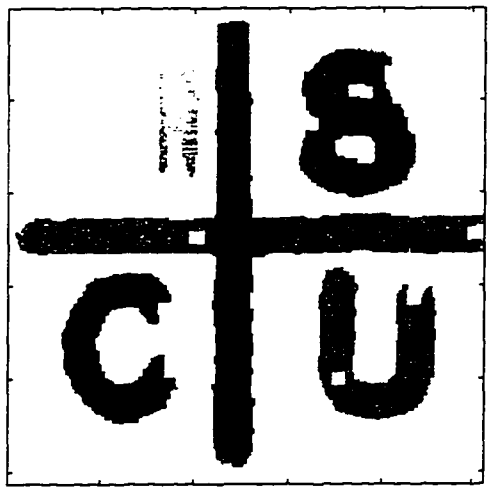

(f)

Figure 6.14. (Continued)

CHAPTER 7 PERFORMANCE EVALUATION

This chapter focuses on evaluating the performance of the speckle noise reduction and data fusion algorithms described in chapters 4 and 5. The chapter begins with a description of the procedure used for evaluating the performance of the speckle noise reduction algorithm. The performance of the algorithm is then compared with those obtained using lowpass and median filters. Next, the performance of the data fusion algorithm is compared with that obtained using the multi-resolution decomposition technique employing the LMMSE filter approach.

Performance of the Proposed Speckle Noise Reduction Algorithm

It is common practice to employ a noise free reference image to measure and compare the effectiveness of noise reduction algorithms. The degraded image is typically obtained by adding random noise to the reference image. The noisy image is then restored using the new algorithm. The performance of the algorithm is then evaluated by computing such measures as the mean squared error (MSE) using the reference and restored images. In NDE image processing applications, it is difficult to obtain a clean reference image due to noise introduced by the measurement system and the speckle noise/clutter caused by the microstructure of the material under test. Consequently we are forced to assume an appropriate reference image to evaluate the performance of the proposed algorithm quantitatively.

In this dissertation we use the speckle noise reduced images as reference images and

superimpose additive Gaussian random noise to obtain the "degraded" or "corrupted" image. Figure 7.1 summarizes the performance evaluation procedure that includes the method used for generating the noise corrupted image. The procedure is initiated by adding a small amount of noise to the reference image. The MSE between the reference and degraded images is then calculated. If the MSE of the degraded image is less than that of the measured original image, the additive noise level is increased iteratively until the MSE of degraded image is close to that of the measured original image. Images shown in Figures 7.2(a) through (n) show noise corrupted images obtained from images shown in Figures 6.6(a) through (h), 6.10(a) through (f) (except (e)), and 4.14(c), respectively. Table 7.1 shows the MSE of the measured original (Figures 6.2, 6.8(a) through (f) (except (e)), and 4.3(b)) and the degraded images (Figure 7.2). One could argue that at least in the MSE sense, the degraded images are similar to the original images. Figures 7.3(a) through (n) show histograms of the degraded images shown in Figures 7.2(a) through (n), respectively. In order to compare the gray level distributions of the degraded images with the measured original images, Figures 7.4(a) through (n) show histograms of the measured original images shown in Figures 6.6(a) through (h), 6.10(a) through (f) (except (e)), and 4.14(c), respectively. These histograms show that the gray level distribution of the two sets of images are approximately the same.

Figures 7.5(a) through (n) show the speckle noise reduced images obtained from images shown in Figures 7.2(a) through (n), respectively, using the proposed speckle noise reduction algorithm. If the reference and processed image functions are denoted by $G(m,n)$ and $Y(m,n)$, respectively, the MSE is defined as

$$MSE = \frac{1}{MN} \sum_{i=1}^{M} \sum_{j=1}^{N} \{Y(i,j) - G(i,j)\}^2 \tag{7.1}$$

where M and N denote the image sizes along the horizontal and vertical directions. Table 7.2 shows the MSE obtained as a result of processing the images corrupted by Gaussian noise with lowpass and median filters as well as the algorithm described in chapter 4.

It is evident that the use of the proposed algorithm results in a much lower MSE compared with those obtained with lowpass and median filters. Three alternate definitions of signal-to-noise ratio (SNR) were also used to evaluate the performance of the algorithm quantitatively [100]:

$$\begin{aligned} &SNR_1 = 10 \log_{10} \frac{\sigma^2}{MSE} (dB) \\ &where\ \sigma^2 = \frac{1}{MN} \sum_{i=1}^{M} \sum_{j=1}^{N} [G(i,j) - \overline{G}]^2, \overline{G} = \frac{1}{MN} \sum_{i=1}^{M} \sum_{j=1}^{N} G(i,j) \end{aligned} \tag{7.2}$$

$$SNR_2 = 10 \log_{10} \frac{\frac{1}{MN} \sum_{i=1}^{M} \sum_{j=1}^{N} G(i,j)^2}{MSE} (dB) \tag{7.3}$$

$$PSNR = 10 \log_{10} \frac{\{max(G)\}^2}{MSE} (dB) \tag{7.4}$$

Tables 7.3 through 7.5 summarize the results obtained using the three definitions. These results demonstrate that the proposed algorithm offers superior SNR compared to lowpass and median filters. In the case of the image shown in Figure 7.2(b) where the gray levels of defect features are comparable to those of noise, the peak SNR (PSNR) as defined by equation (7.4) of the images processed by lowpass filter, median filter and the proposed algorithm are 7.25, 7.36 and 17.08 dB, respectively. Similarly in the case of the image shown

in Figure 7.2(f) where the defect features are clearly distinguishable from noise, the PSNR of images obtained by using lowpass and median filters, and the proposed algorithm are 14.51, 14.69 and 41.69 dB, respectively. In summary, the increase in PSNR resulting from the use of the proposed algorithm for the images shown in Figure 7.2 ranges from about 6 to 27 dB.

Performance of the Proposed NDE Data Fusion Algorithm

Simulation results obtained using the multi-resolution decomposition technique employing LMMSE filters are presented for comparison with results obtained by employing the data fusion algorithm using morphological approaches. Figures 7.6(a) through (f) show fused images obtained from images shown in Figures 6.8 and 6.9(a) through (f), respectively, using the multi-resolution decomposition technique. As shown in Figure 7.6, the results do not combine the complementary information effectively. The complementary includes information about the depth of the defect contained in the eddy current image and information pertaining to the boundaries of the defect that is contained in the ultrasonic image. In addition, the speckle noise in the ultrasonic image is also fused thereby degrading the results. Figure 6.14 shows the images fused from the images shown in Figures 6.8 and 6.9 using the proposed algorithm. The fused images shown in Figure 6.14 demonstrate the effectiveness of the algorithm. The resulting images show that the algorithm combines information relating to locations and boundaries of the defect obtained from the ultrasonic images with the depth information derived from the eddy current image. The result also indicates that image obtained using the proposed algorithm shown in Figure 6.14(f) provides a greater level of

information than either the ultrasonic or eddy current image. Figures 7.7 and 7.8 show line scans obtained from the original ultrasonic and eddy current images. Figure 7.9 shows the line scans obtained from the fused images. These line scans reveal the gray level transitions in the defect regions very clearly.

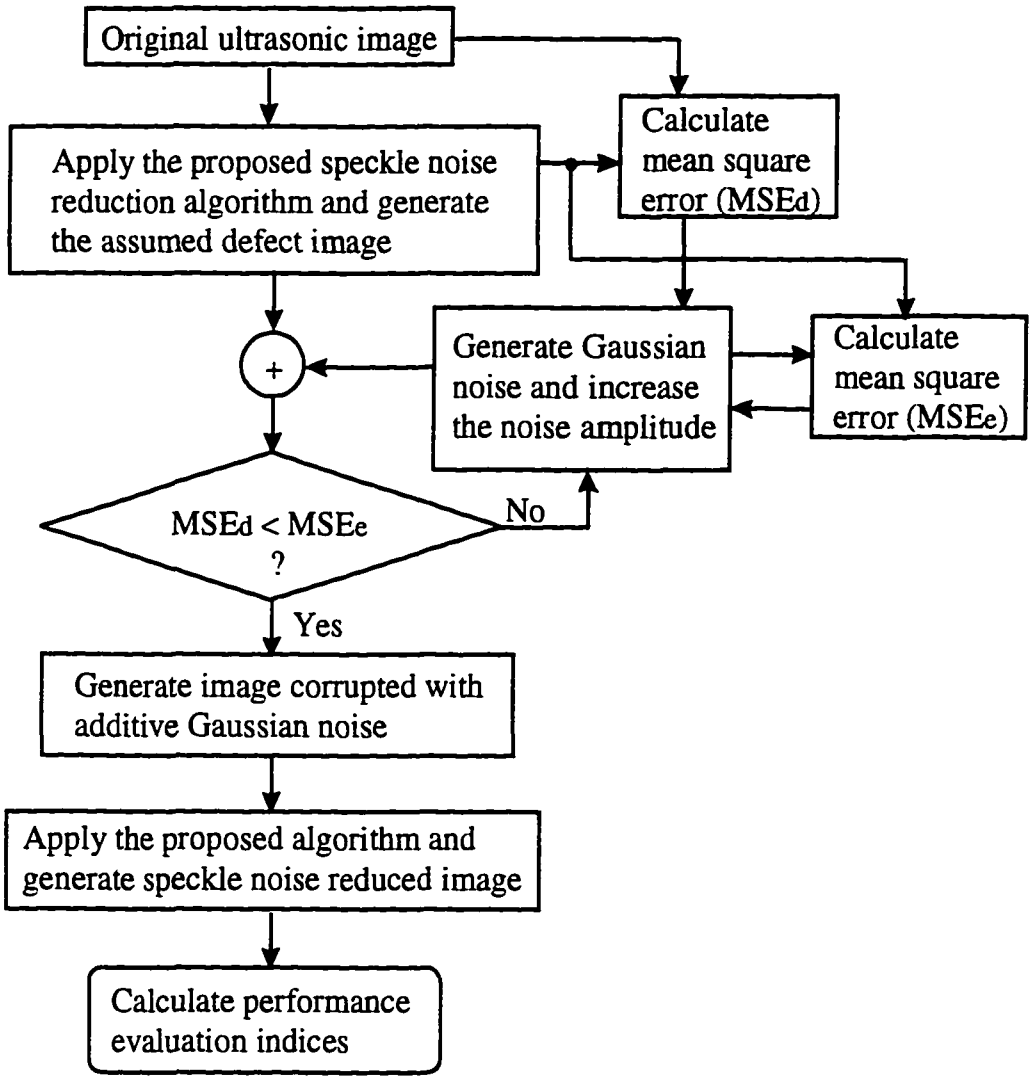

Figure 7.1. Procedure for evaluating the performance of the proposed speckle noise reduction algorithm.

Table 7.1. Comparison of MSE of the measured original and degraded images.

Reference Image	Measured Original Image	Degraded Image
Figure 6.6(a)	4918	4985
Figure 6.6(b)	12210	12228
Figure 6.6(c)	4667	4732
Figure 6.6(d)	6238	6295
Figure 6.6(e)	3362	3434
Figure 6.6(f)	2258	2346
Figure 6.6(g)	5824	5911
Figure 6.6(h)	2993	3023
Figure 6.10(a)	2381	2479
Figure 6.10(b)	2956	2970
Figure 6.10(c)	5210	5249
Figure 6.10(d)	8738	8804
Figure 6.10(f)	2884	2953
Figure 4.14(c)	2624	2668

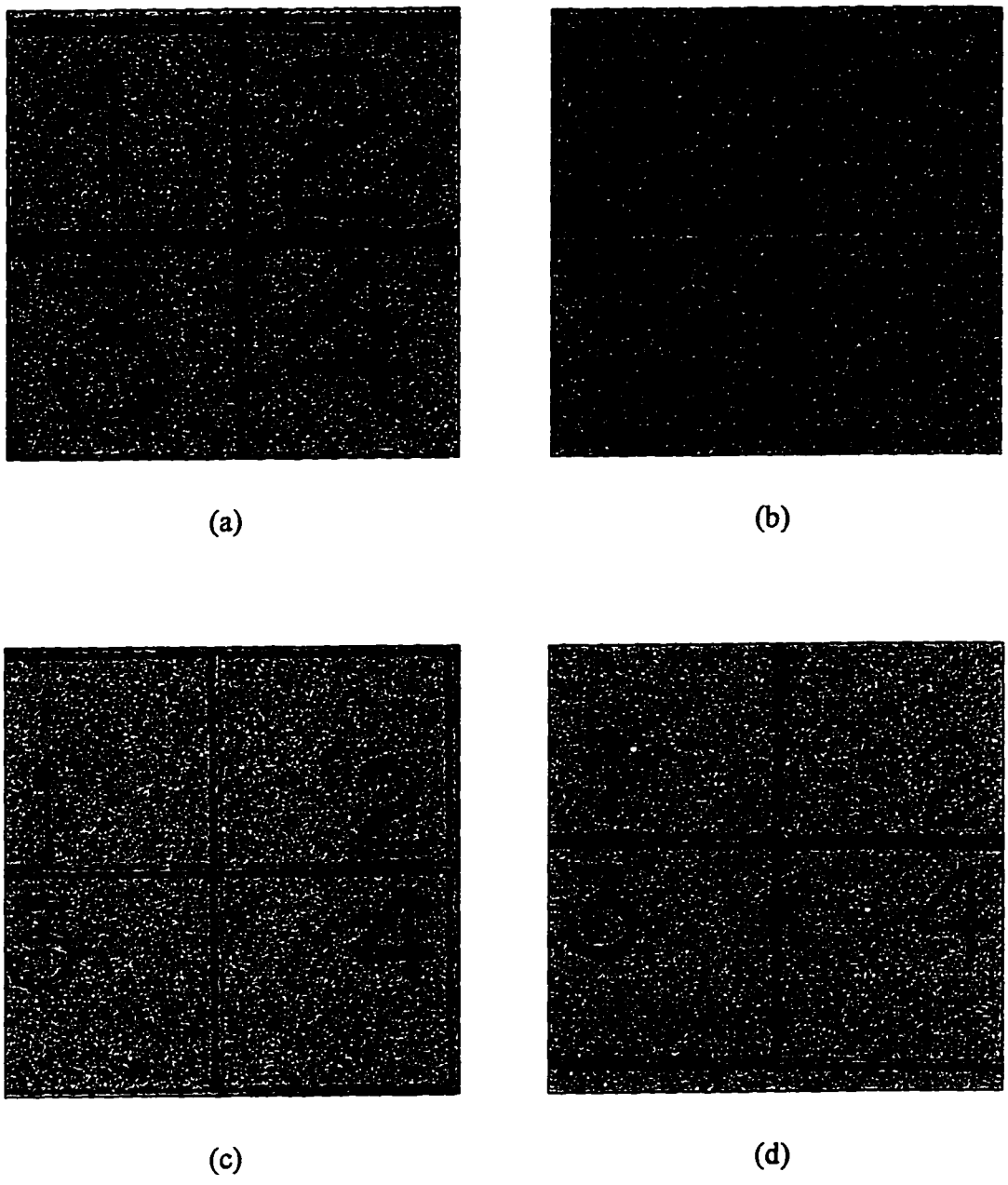

Figure 7.2. Noise corrupted images.

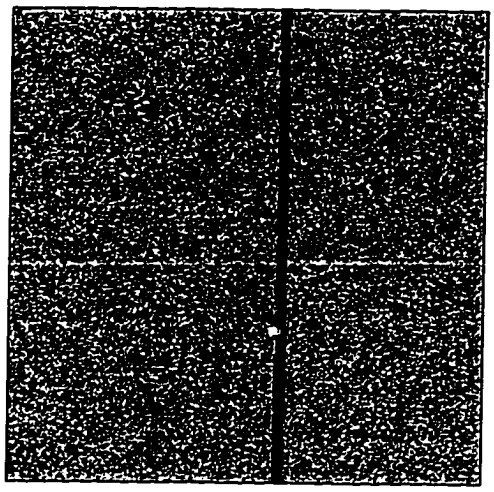

(e)

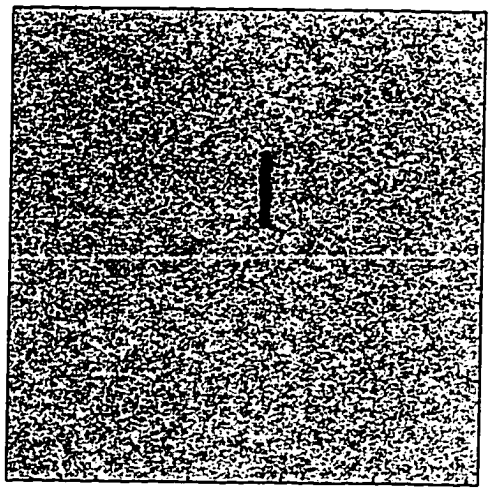

(f)

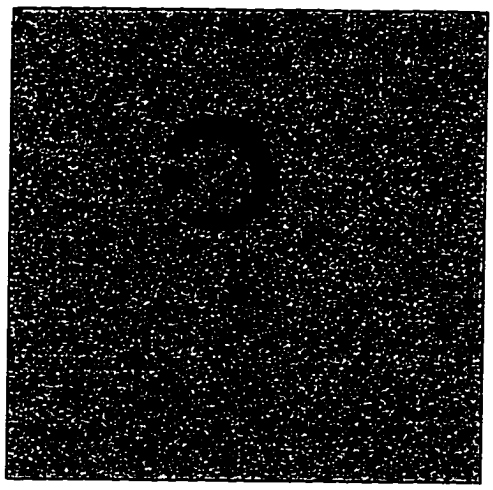

(g)

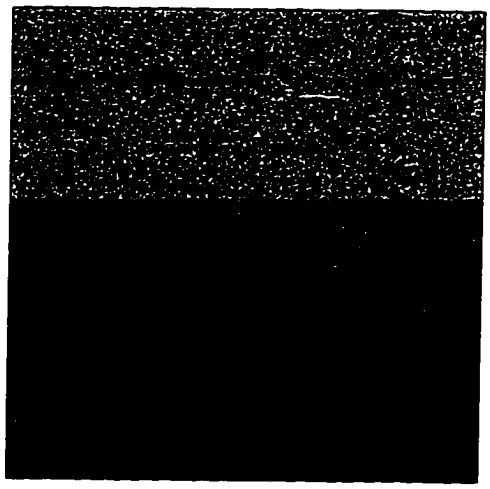

(h)

Figure 7.2. (Continued)

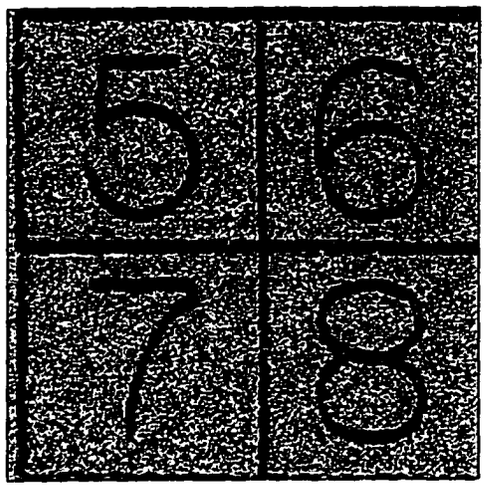

(i)

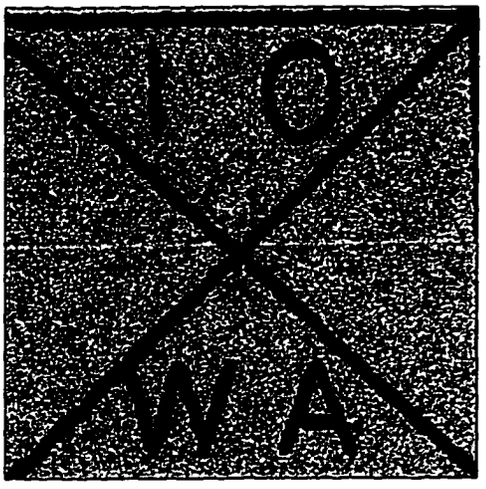

(j)

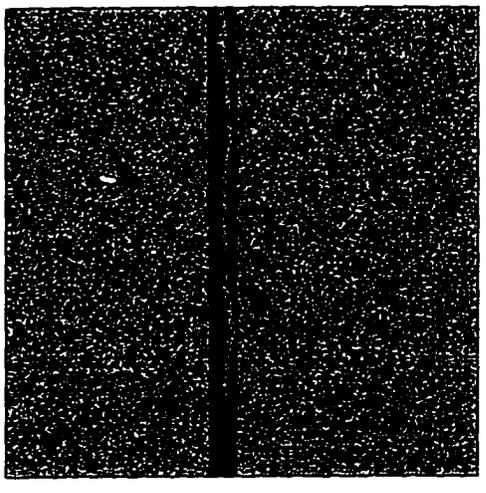

(k)

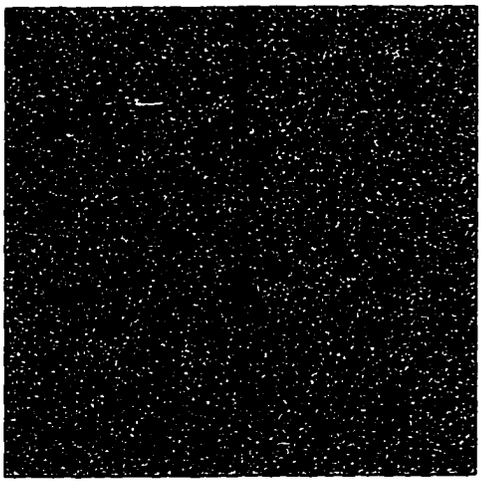

(l)

Figure 7.2. (Continued)

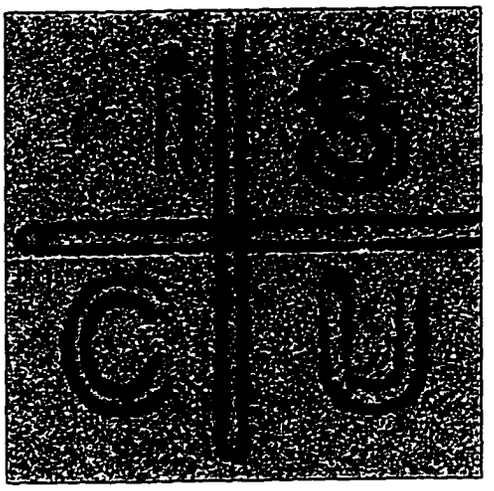

(m)

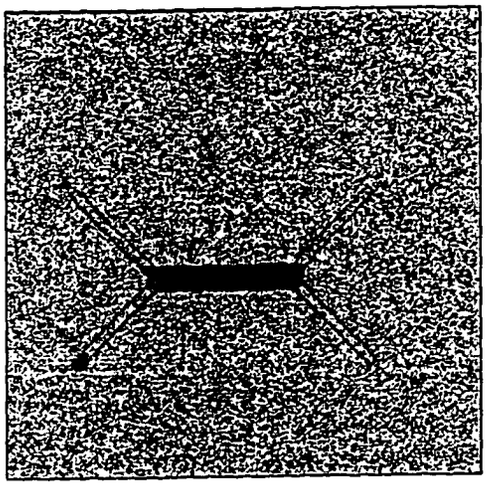

(n)

Figure 7.2. (continued)

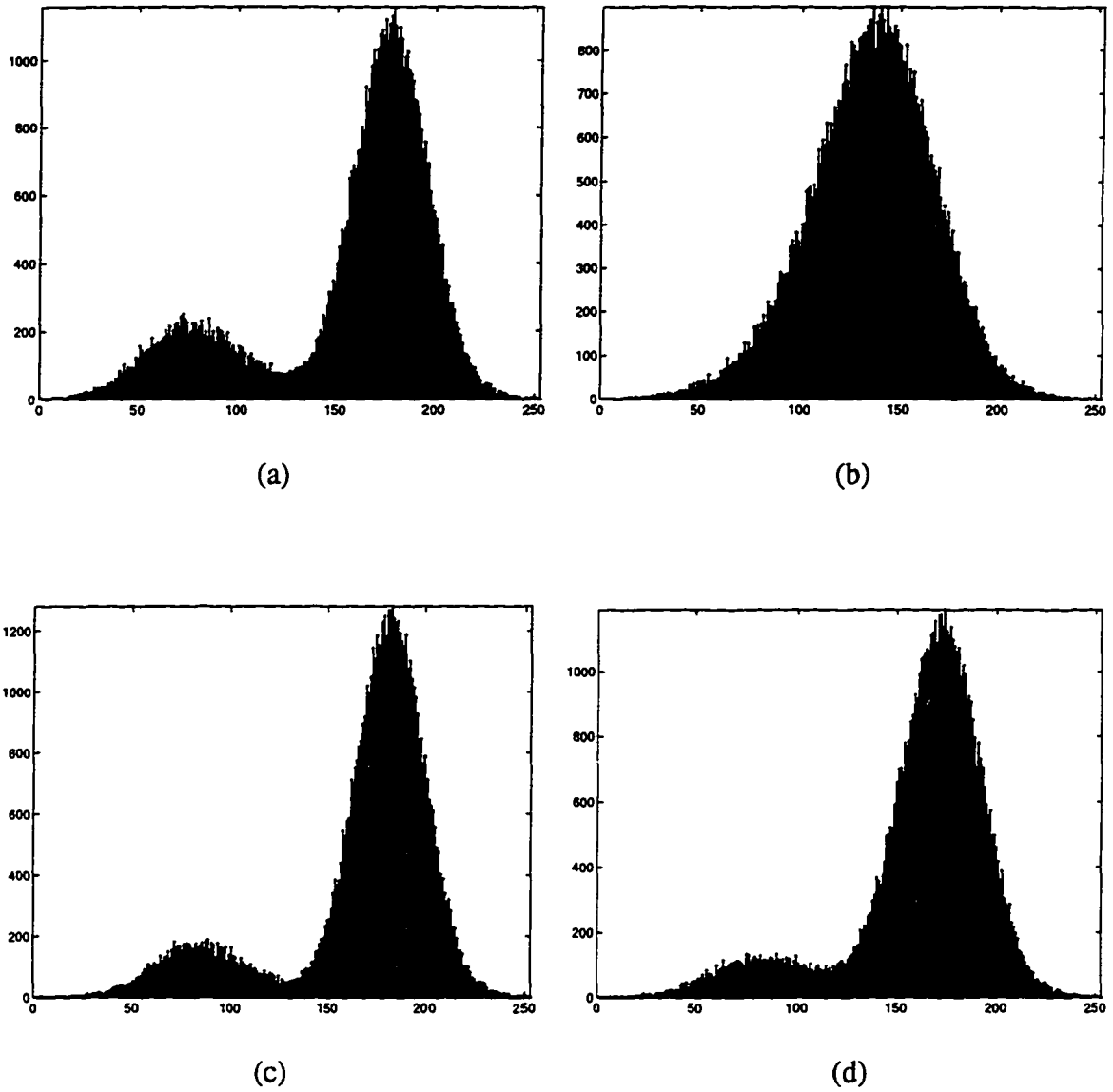

Figure 7.3. Histograms of the noise corrupted images. Images are shown in Figure 7.2.

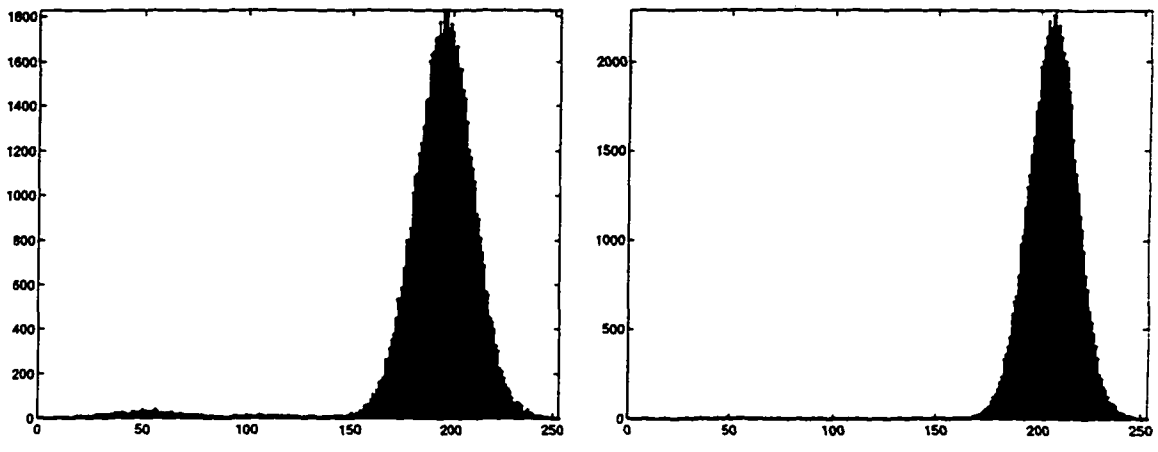

(e) (f)

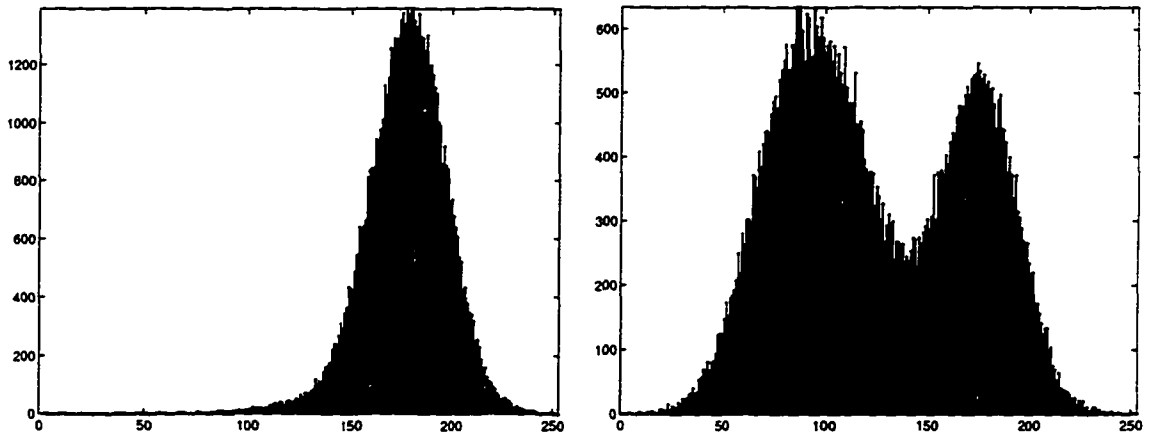

(g) (h)

Figure 7.3. (Continued)

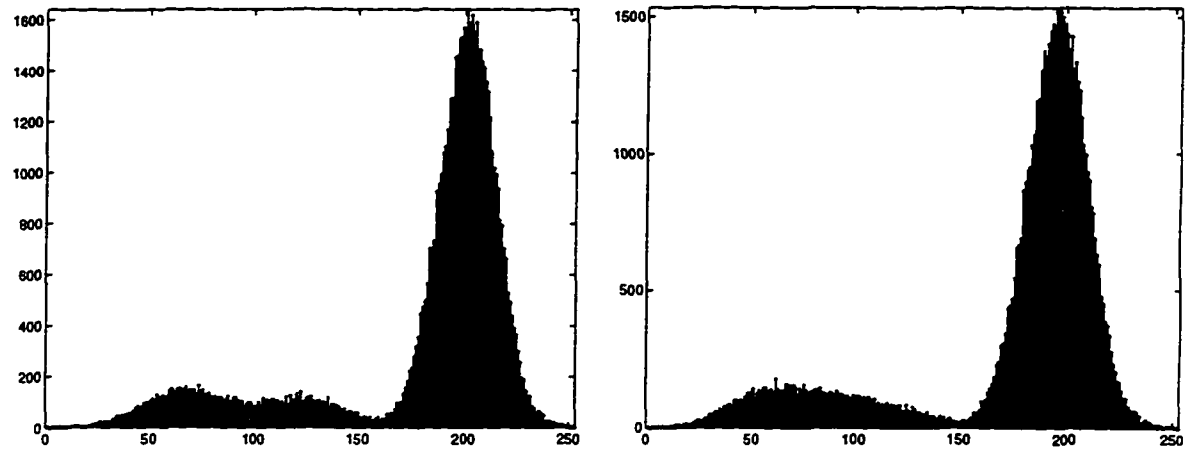

(i)

(j)

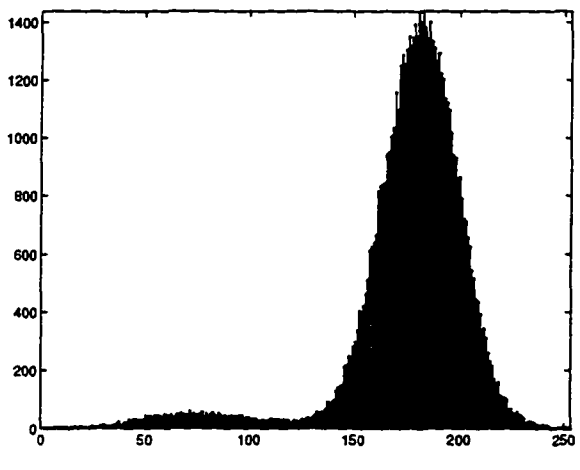

(k)

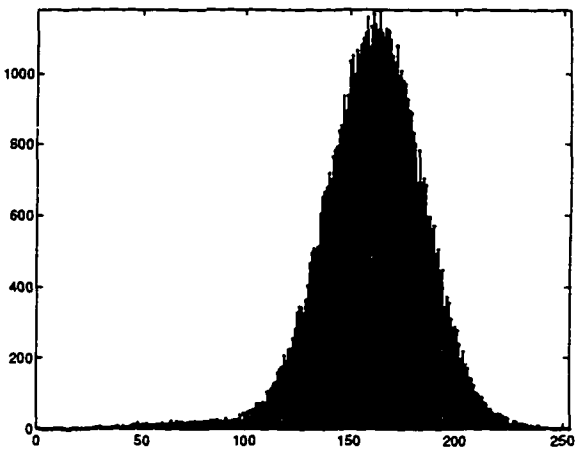

(l)

Figure 7.3. (Continued)

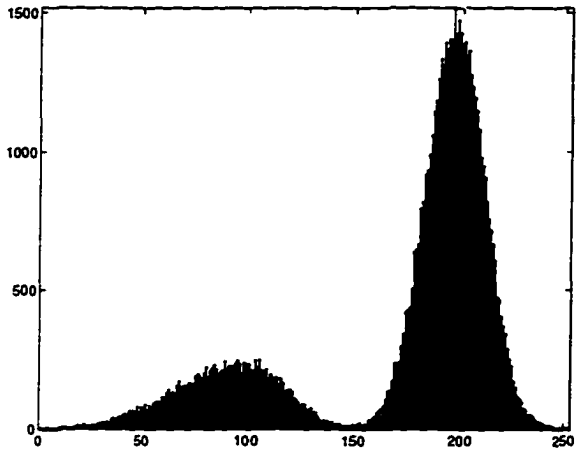

(m)

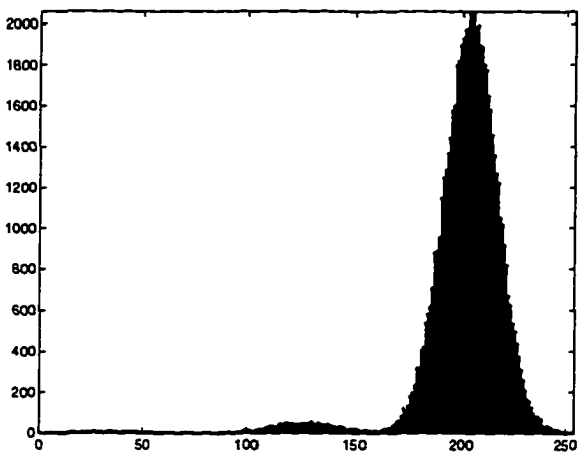

(n)

Figure 7.3. (Continued)

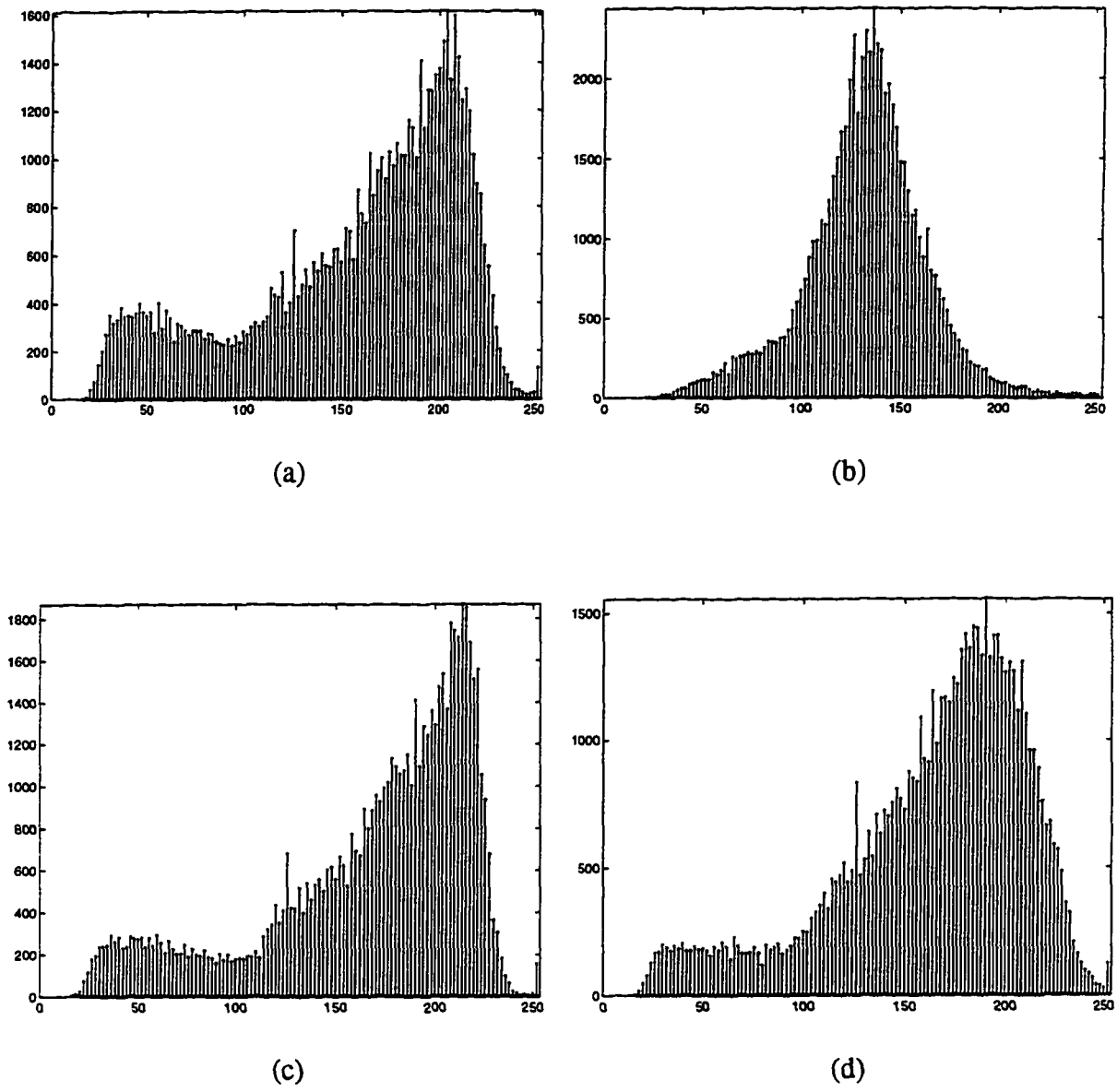

Figure 7.4. Histograms of the original ultrasonic images.

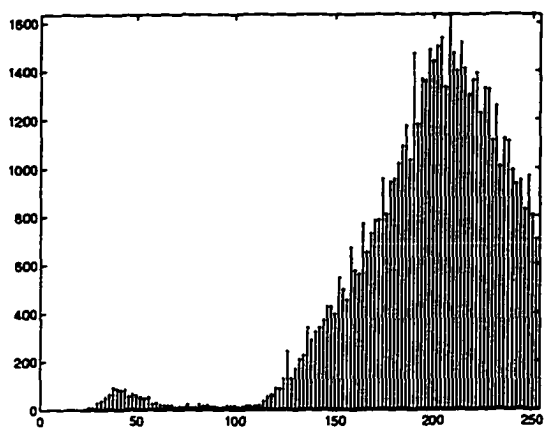

(e)

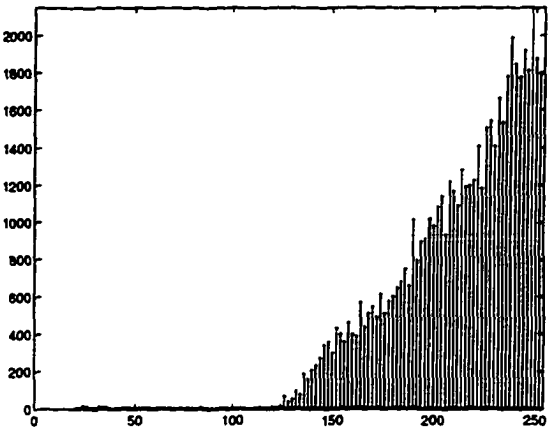

(f)

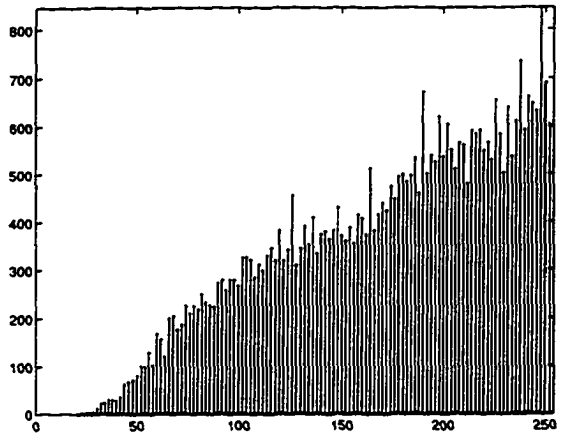

(g)

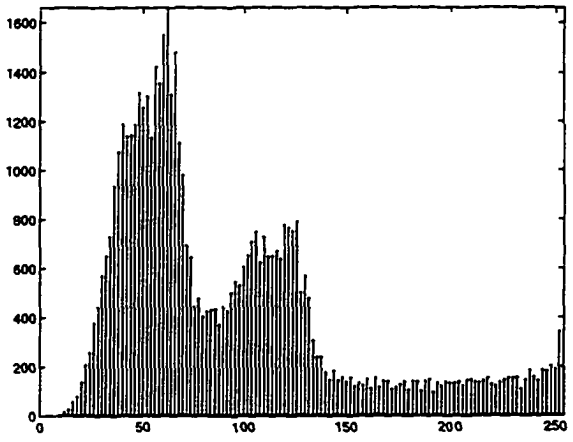

(h)

Figure 7.4. (Continued)

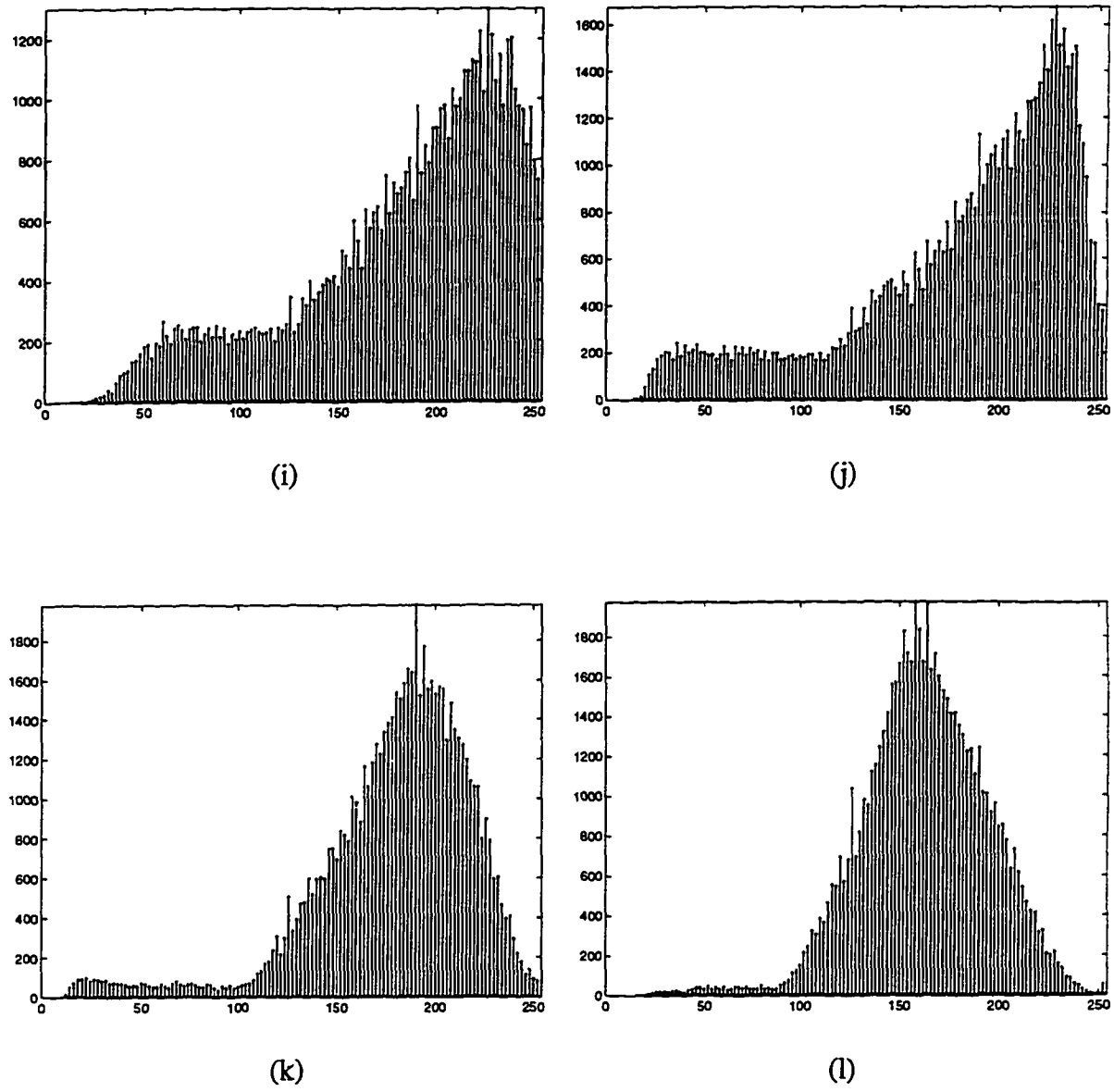

Figure 7.4. (Continued)

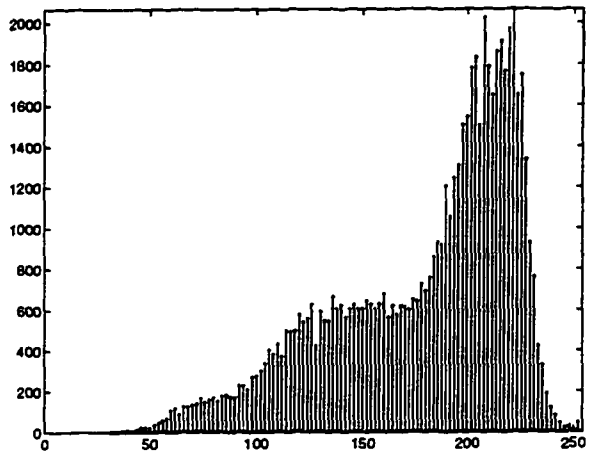

(m)

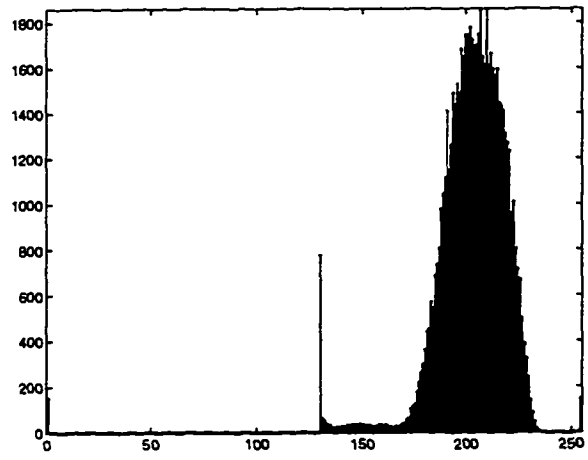

(n)

Figure 7.4. (Continued)

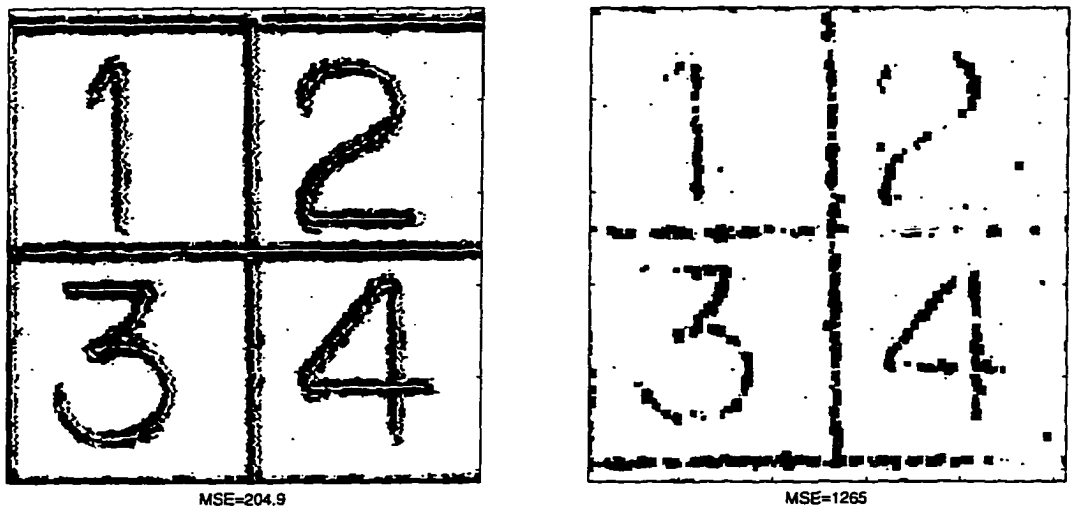

Figure 7.5. Speckle noise reduced images.

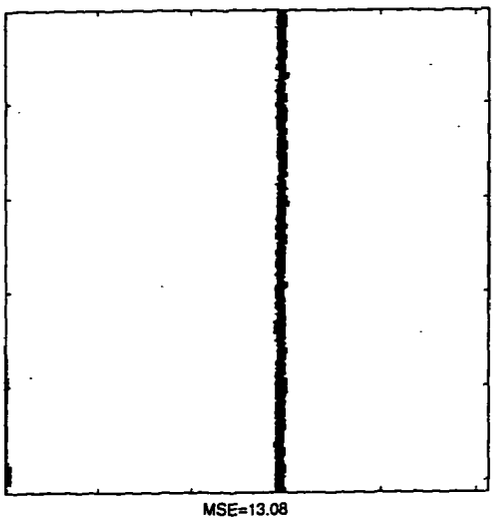

(e)

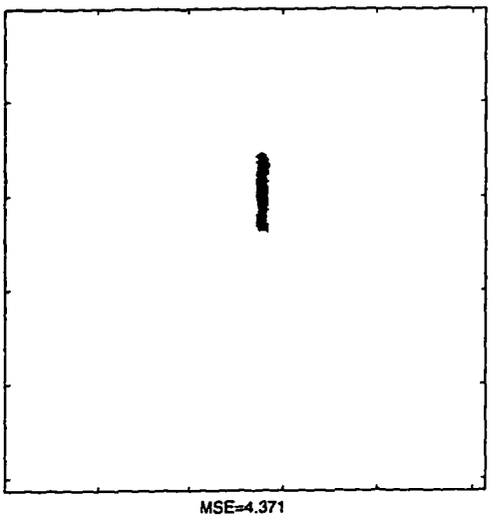

(f)

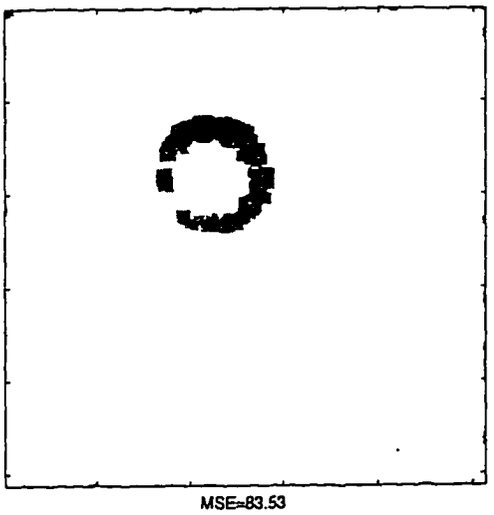

(g)

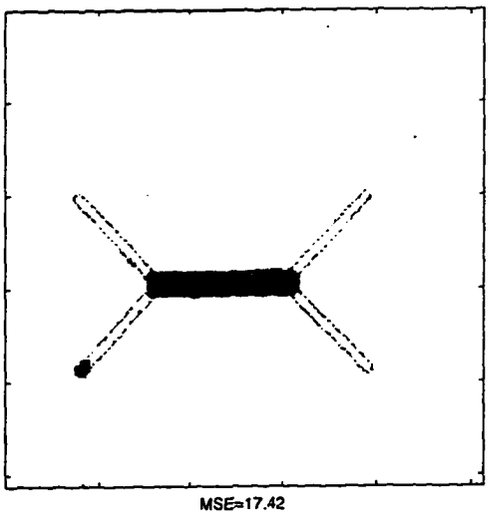

(h)

Figure 7.5. (Continued)

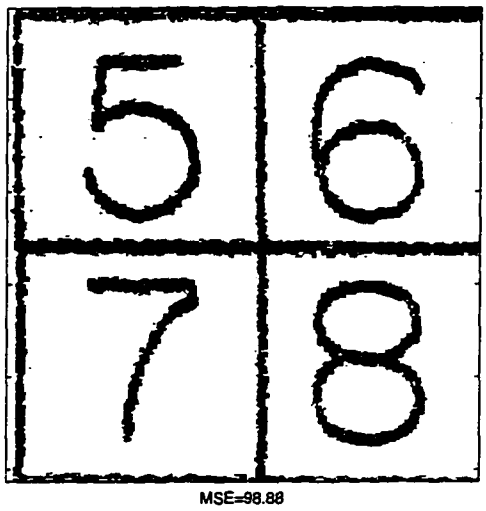

MSE=98.88

(i)

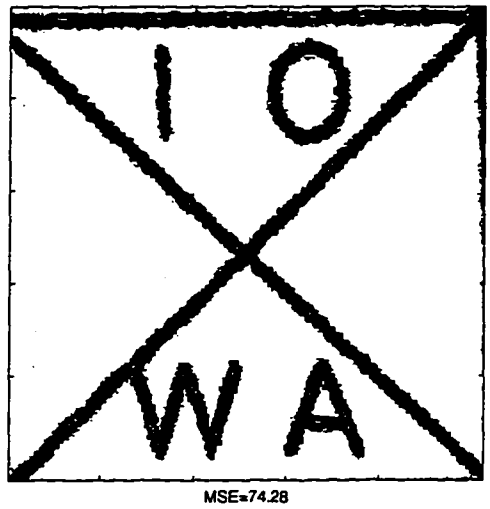

MSE=74.28

(j)

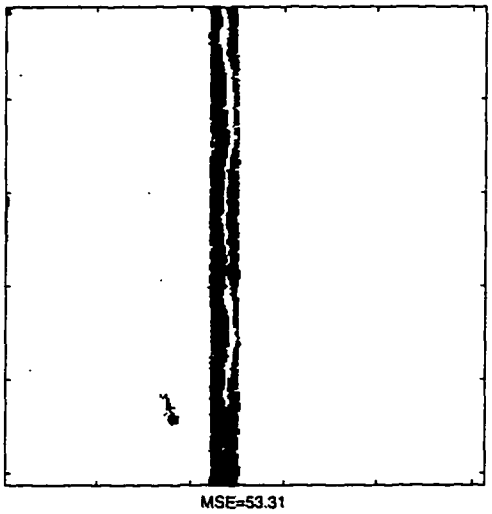

MSE=53.31

(k)

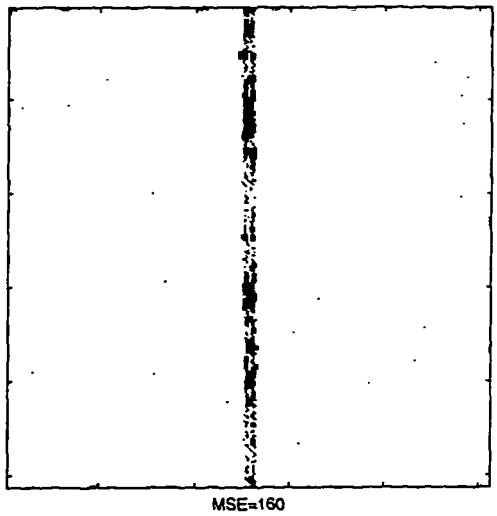

MSE=160

(l)

Figure 7.5. (Continued)

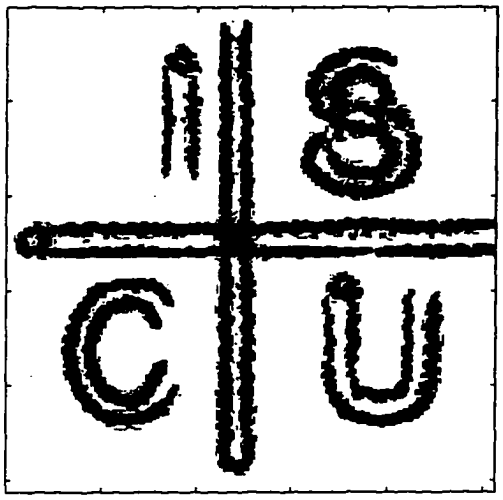

(m)

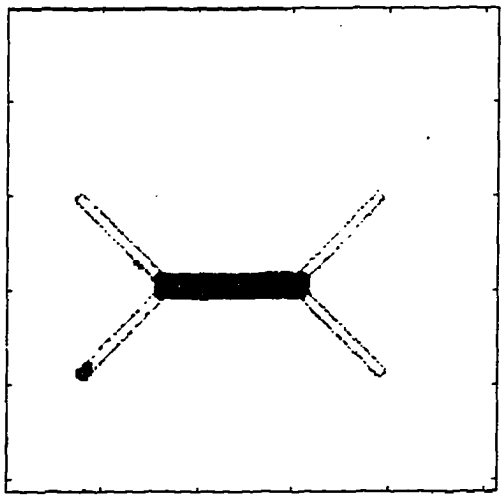

(n)

Figure 7.5. (Continued)

Table 7.2. Comparison of performance using MSE as a performance index.

Reference Image	Lowpass Filter	Median Filter	Proposed Algorithm
Figure 6.6(a)	6915	5806	205
Figure 6.6(b)	12144	11842	1265
Figure 6.6(c)	6112	5390	193
Figure 6.6(d)	7229	6456	256
Figure 6.6(e)	3512	3278	13
Figure 6.6(f)	2285	2190	4
Figure 6.6(g)	5634	5554	84
Figure 6.6(h)	2993	2726	685
Figure 6.10(a)	3894	2763	99
Figure 6.10(b)	4886	3244	74
Figure 6.10(c)	5576	5136	53
Figure 6.10(d)	8511	8460	160
Figure 6.10(f)	4431	3070	226
Figure 4.14(c)	2721	2625	17

Table 7.3. Comparison of performance using SNR_1(dB) as a performance index.

Reference Image	Lowpass Filter	Median Filter	Proposed Algorithm
Figure 6.6(a)	-0.77	-0.01	14.52
Figure 6.6(b)	-6.13	-6.02	3.69
Figure 6.6(c)	-1.18	-0.63	13.82
Figure 6.6(d)	-2.97	-2.48	11.54
Figure 6.6(e)	-6.60	-6.30	17.69
Figure 6.6(f)	-12.33	-12.15	14.85
Figure 6.6(g)	-15.68	-15.62	2.61
Figure 6.6(h)	1.79	4.25	10.25
Figure 6.10(a)	-0.21	1.28	15.74
Figure 6.10(b)	-0.44	1.42	17.82
Figure 6.10(c)	-4.93	-4.57	15.26
Figure 6.10(d)	-11.53	-11.50	5.73
Figure 6.10(f)	-1.13	0.47	11.80
Figure 4.14(c)	-7.42	-7.26	14.52

Table 7.4. Comparison of performance using SNR_2(dB) as a performance index.

Reference Image	Lowpass Filter	Median Filter	Proposed Algorithm
Figure 6.6(a)	5.63	6.46	24.07
Figure 6.6(b)	1.83	2.03	16.70
Figure 6.6(c)	6.69	7.33	24.60
Figure 6.6(d)	5.62	6.18	23.52
Figure 6.6(e)	10.22	10.61	36.84
Figure 6.6(f)	12.66	12.89	41.67
Figure 6.6(g)	7.46	7.48	28.79
Figure 6.6(h)	5.39	8.24	16.85
Figure 6.10(a)	9.41	10.97	27.38
Figure 6.10(b)	7.98	9.95	28.64
Figure 6.10(c)	7.50	7.98	30.62
Figure 6.10(d)	4.83	4.90	25.98
Figure 6.10(f)	8.43	10.05	23.62
Figure 4.14(c)	11.74	11.86	35.62

Table 7.5. Comparison of performance using PSNR(dB) as a performance index.

Reference Image	Lowpass Filter	Median Filter	Proposed Algorithm
Figure 6.6(a)	9.70	10.46	24.98
Figure 6.6(b)	7.25	7.36	17.08
Figure 6.6(c)	10.23	10.78	25.23
Figure 6.6(d)	9.51	10.00	24.01
Figure 6.6(e)	12.64	12.94	36.93
Figure 6.6(f)	14.51	14.69	41.69
Figure 6.6(g)	10.59	10.65	28.88
Figure 6.6(h)	11.28	13.74	19.74
Figure 6.10(a)	12.19	13.68	28.15
Figure 6.10(b)	11.12	12.99	29.39
Figure 6.10(c)	10.63	10.99	30.83
Figure 6.10(d)	8.80	8.82	26.06
Figure 6.10(f)	11.63	13.22	24.56
Figure 4.14(c)	13.79	13.94	35.72

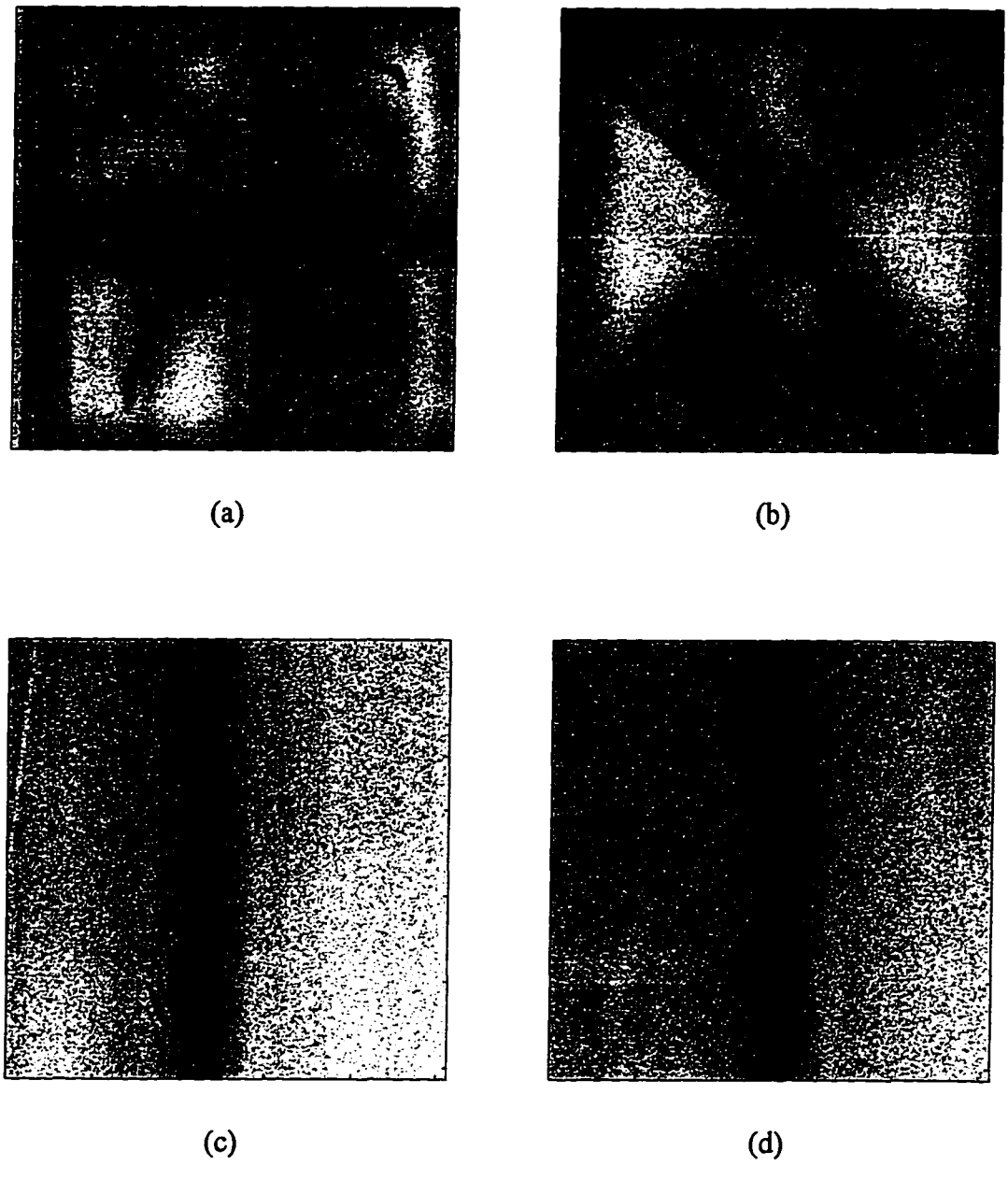

Figure 7.6. Fused images obtained using multi-resolution decomposition techniques employing LMMSE filters.

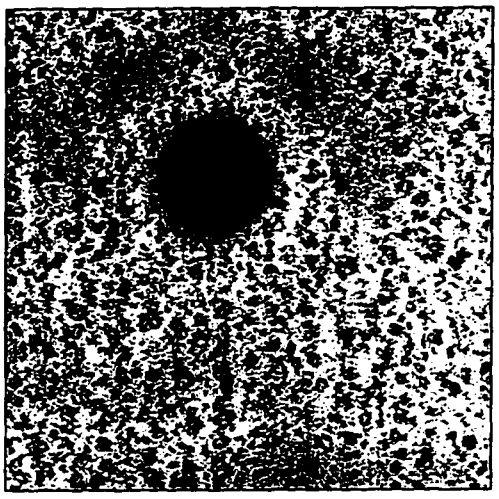

(e)

(f)

Figure 7.6. (Continued)

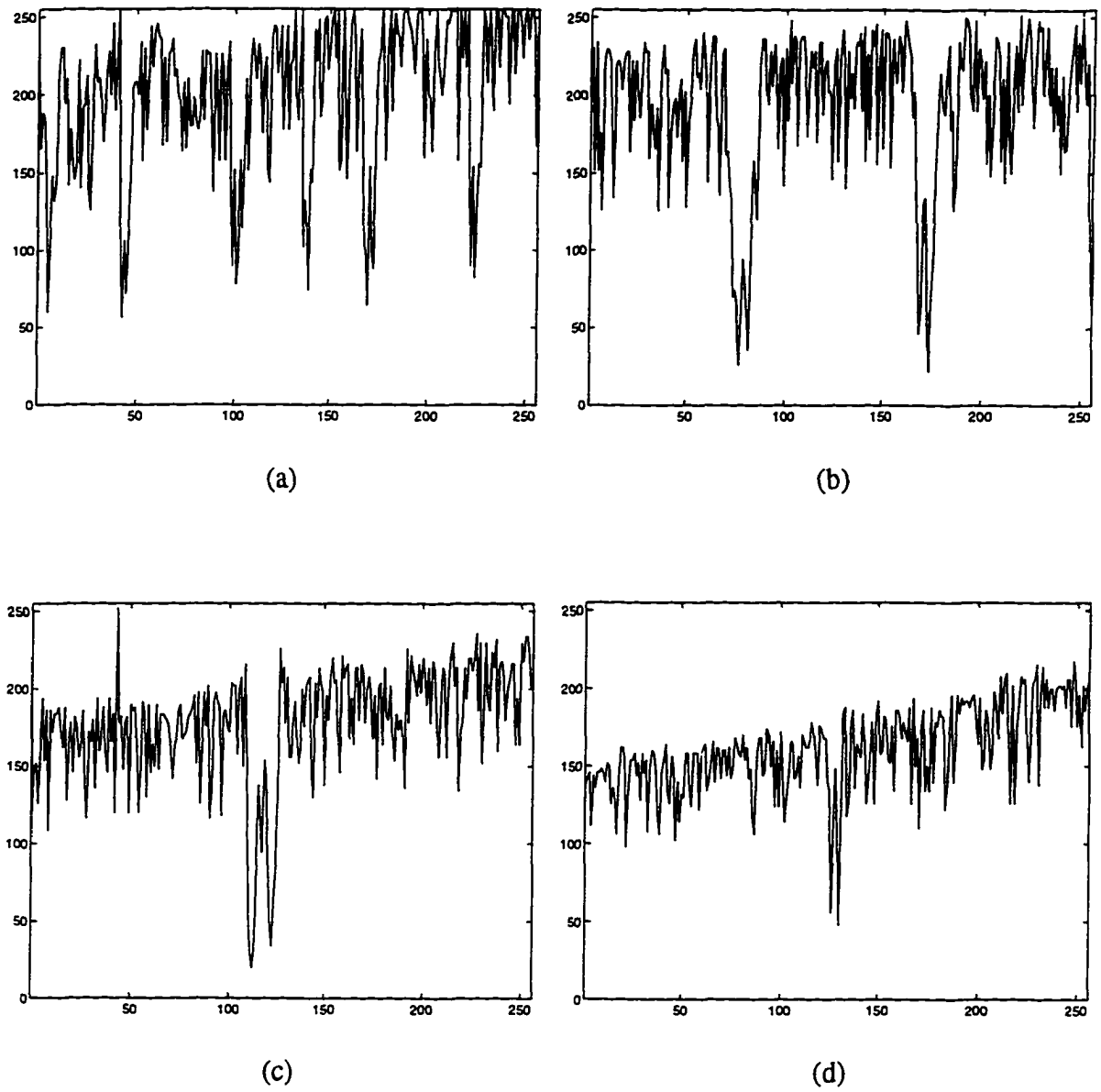

Figure 7.7. Line scans obtained from the original ultrasonic images.

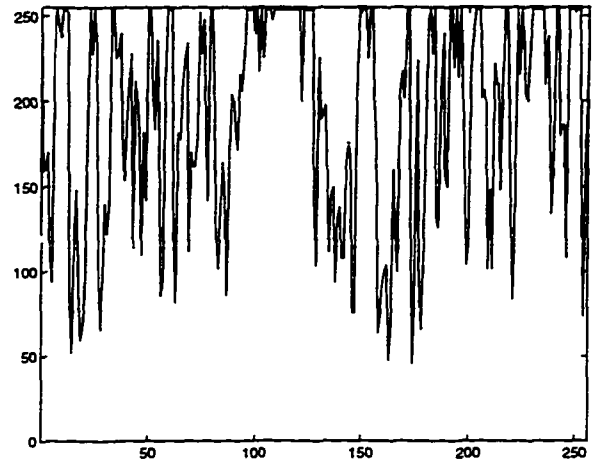

(e)

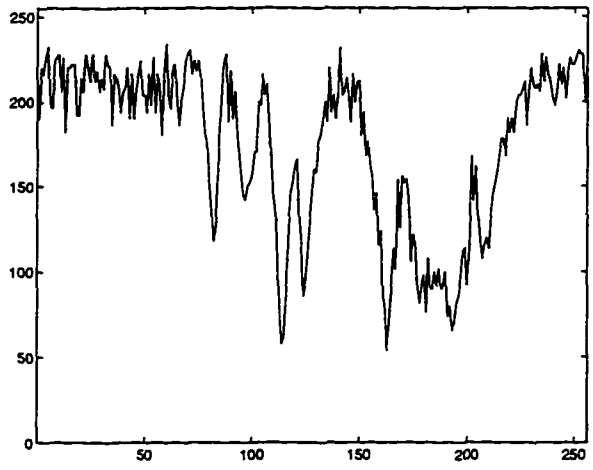

(f)

Figure 7.7. (Continued)

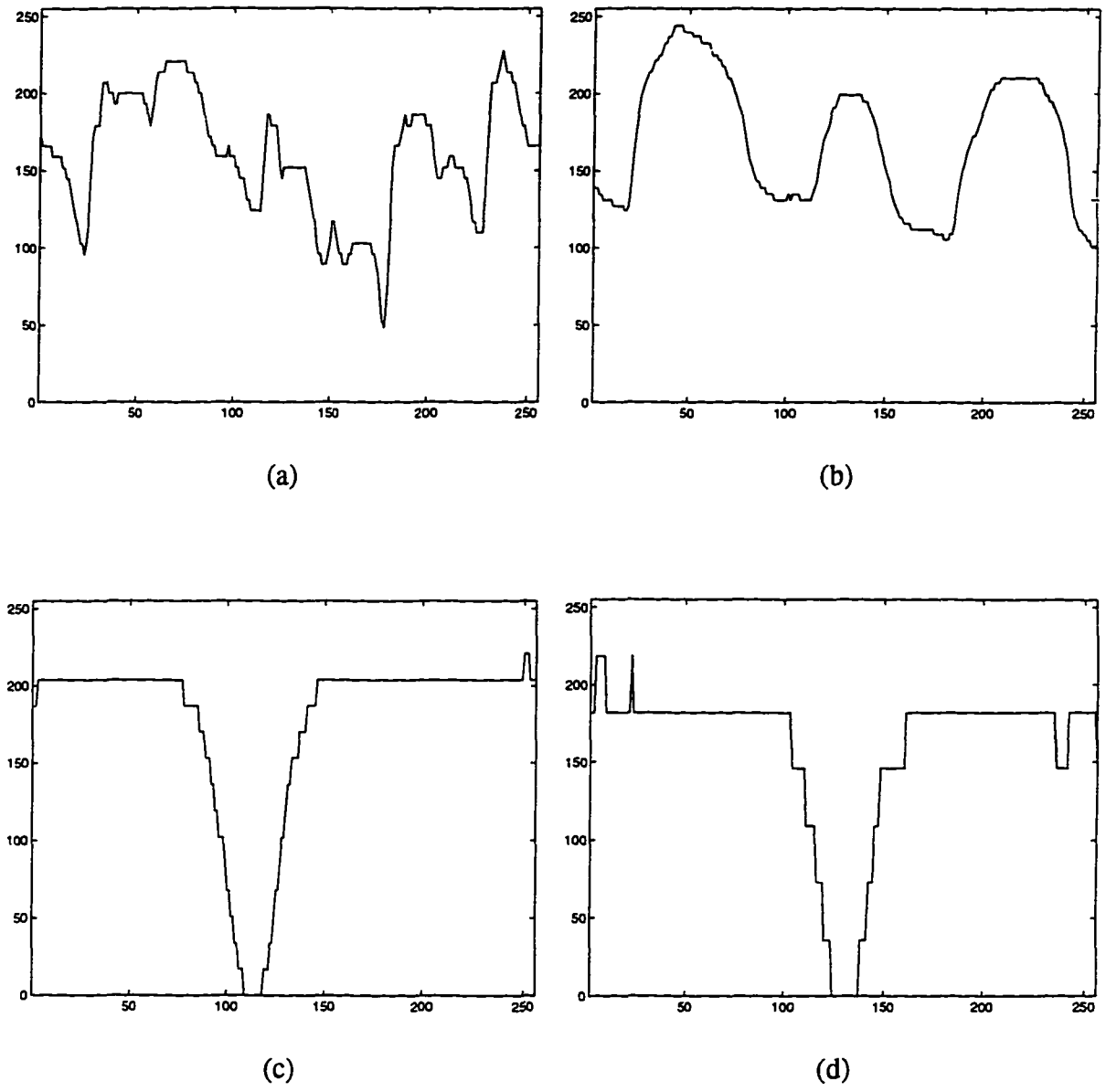

Figure 7.8. Line scans of the original eddy current images.

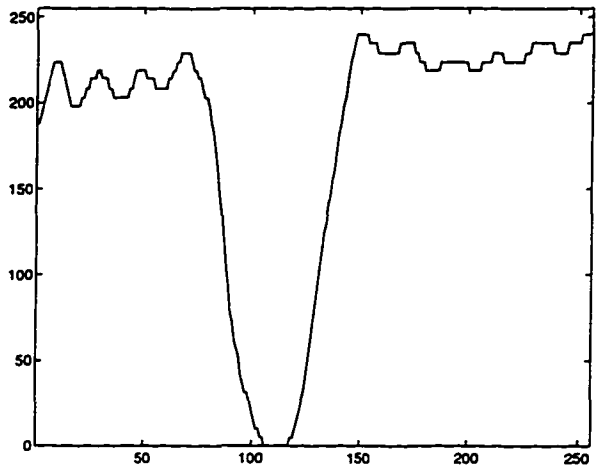

(e)

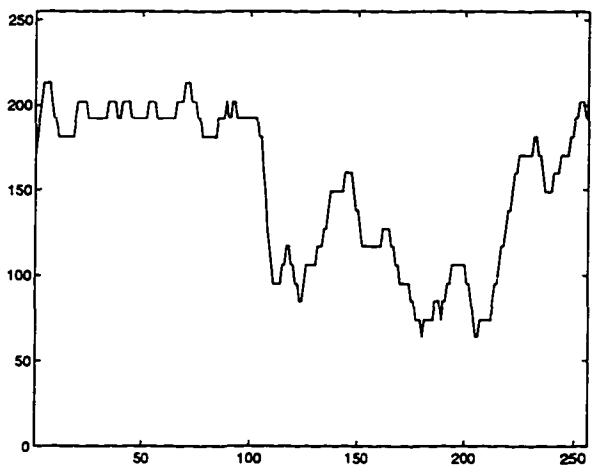

(f)

Figure 7.8. (Continued)

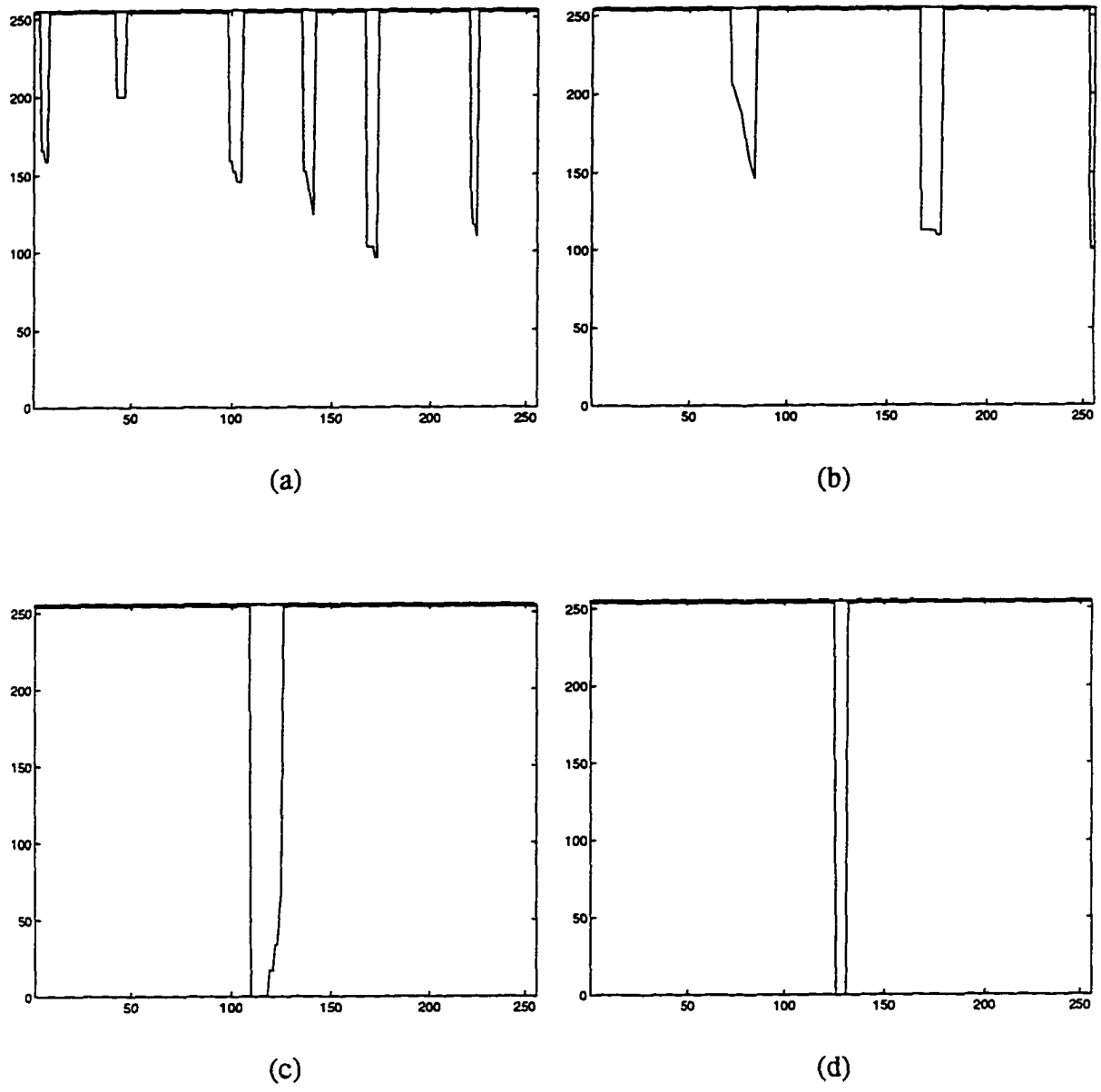

Figure 7.9. Line scans obtained from the fused images.

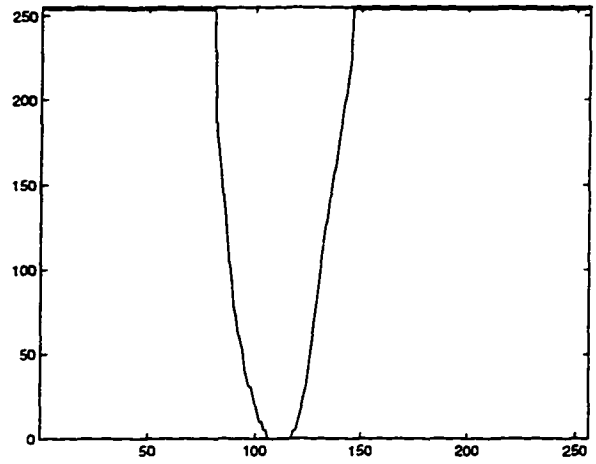

(e)

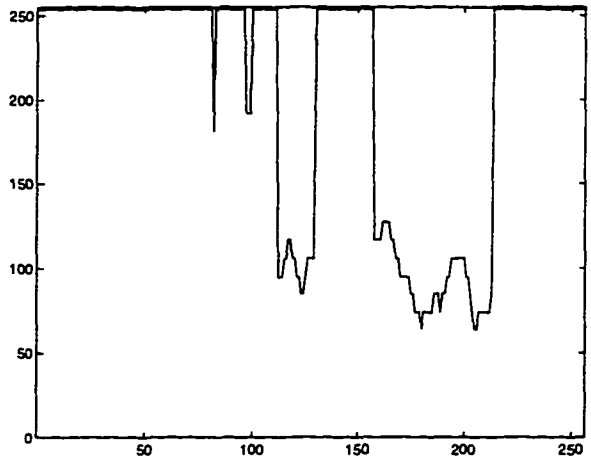

(f)

Figure 7.9. (Continued)

CHAPTER 8 CONCLUSIONS AND FUTURE WORK

Summary of Contributions

The two main contributions described in this dissertation are: (1) A new NDE data fusion algorithm using morphological approaches (2) A new morphological algorithm for reducing speckle noise in ultrasonic images which is used as a part of the preprocessing step. These algorithms have been implemented and evaluated. The simulation results obtained from a variety of experimentally derived ultrasonic and eddy current NDE images demonstrate that the proposed algorithm offers excellent results. The approach clearly illustrates the benefits of fusing data from a heterogeneous set of sensors. In addition, the simulation results show that the noise reduction algorithm is capable of minimizing speckle noise very effectively without losing thin features such as those due to thin cracks in ultrasonic images.

Summary of Dissertation

A new NDE data fusion strategy using morphological approaches has been developed. As part of the preprocessing step, a new morphological algorithm for reducing speckle noise in ultrasonic images is also presented.

In developing an efficient NDE data fusion algorithm, it is important to understand the fundamental capabilities and limitations of the NDE test methods. Chapter 2 describes the fundamentals of ultrasonic and eddy current test methods. The capabilities and limitations of each method are illustrated and discussed using experimentally derived ultrasonic and eddy current images.

Fundamental operations of binary and gray scale morphologies in image processing are reviewed in chapter 3. Their mathematical definitions and algebraic properties are described briefly. The advantages and disadvantages of the conventional morphological noise reduction filters are illustrated.

In chapter 4, a new NDE data fusion method using morphological approaches is developed. A new morphological algorithm for reducing speckle noise in ultrasonic images is also presented in this chapter. The proposed speckle noise reduction algorithm is described in detail using block diagrams.

Chapter 5 describes the proposed new morphological data fusion technique which represents the second stage in the fusion algorithm.

Chapter 6 shows simulation results obtained from a variety of experimentally derived data.

In chapter 7 a procedure for evaluating the performance of the proposed speckle noise reduction algorithm is presented. The performance of the proposed algorithm is compared with those obtained using the lowpass and median filters. The performance of the data fusion algorithm is compared with that obtained using the multi-resolution decomposition technique. The MSE of the proposed speckle noise reduction algorithm is much lower than those obtained using lowpass and median filters. The increase in peak signal-to-noise ratios (PSNR) ranges from 6 to 27 dB in the simulation studies.

Future work

This dissertation presents an efficient strategy for fusing NDE data from ultrasonic and eddy current images. The proposed algorithm is an incremental step towards the development of a comprehensive algorithm for NDE data fusion. As is the case with other existing algorithms, the proposed algorithm may not be perfect for all applications.

First, lift-off variations in eddy current images affect the performance of the algorithm. A procedure for compensating for such lift-off variations has to be developed. Second, significant misalignments between the ultrasonic and eddy current images may result in incorrect estimates of defect depth or boundary. Issues such as image registration must be addressed as part of future work in this area. Algorithms developed for these purpose can be used for making data fusion approach far more robust.

APPENDIX MATHEMATICAL DESCRIPTION OF RESIDUAL IMAGES

The mathematical expressions involved in arriving at the residual image can be derived as follows: In Figure 4.4, the *k*th residual image is given by

$$R_k(m,n) = C_k(m,n) - C_{k-1}(m,n) \tag{A.1}$$

where $C_K(m,n)$ and $C_{K-1}(m,n)$ denote the *k*th and *(k-1)*th closing operation outputs of the structuring elements S_K and S_{K-1}, respectively. If we assume that an image can be modeled as a set of objects containing various sizes, then the image can be expressed as

$$G = \{\, U_t(m_t,n_t) \mid (m_t,n_t) \in D_{U_t},\ t = 1, \ldots, N_L \,\} \tag{A.2}$$

where $U_t\ (m_t,n_t)$ and D_{Ut} denote an object image function and the corresponding domain, respectively and N_L is the index for the largest object. Here, we assume that (image size U_t) < (image size U_{t+1}), for $t = 1, \ldots, N_L\text{-}1$. Substituting (A.2) into equation (3.27) of chapter 3 and then the result into (A.1) for $k=1$ yields:

$$\begin{aligned}
&R_1 = C_1 - G \\
&= \min[\max\{(U_t(m_t - p_t + i_t, n_t - q_t + j_t) \mid (m_t,n_t) \in D_{U_t}, t = 1,\ldots,N_L) \\
&+S_1(p_t,q_t) \mid (p_t,q_t) \in D_{S_1}\} - S_1(i_t,j_t) \mid (i_t,j_t) \in D_{S_1}] \\
&-(U_t(m_t,n_t) \mid (m_t,n_t) \in D_{U_t}, t = 1,\ldots,N_L) \\
&= \{\min[\max\{U_t(m_t - p_t + i_t, n_t - q_t + j_t) + S_1(p_t,q_t) \mid (p_t,q_t) \in D_{S_1}\} \\
&-S_1(i_t,j_t) \mid (i_t,j_t) \in D_{S_1}] - U_t(m_t,n_t) \mid (m_t,n_t) \in D_{U_t}, t = 1,\ldots,N_L\}
\end{aligned} \tag{A.3}$$

If objects in an image are equal to or greater than the size of the predetermined structuring element, the objects survive at the output of closing operation. Thus the subtraction of original input image *G* from the output of closed image results in an image containing objects

that do not fit into the predetermined structuring element. Hence, mathematically (A.3) can be rewritten as

$$R_1(m,n)=\begin{cases}[\min\{\max(U_t(m_t-p_1+i_1,n_t-q_1+j_1)+S_1(p_1,q_1)|(p_1,q_1)\in D_{S_1})\\ -S_1(i_1,j_1)|(i_1,j_1)\in D_{S_1}\}-U_t(m_t,n_t)|(m_t,n_t)\in D_{U_t}], & t=1\\ 0 \quad , & (m,n)\in D_{U_t}, t\neq 1\end{cases}$$

(A.4)

From (A.4) we know that the residual image R_1 contains objects which fit into S_1. An image that does not fit into S_1 is set to zero. Similarly the residual image function R_k at the kth step can be expressed as

$$R_k(m,n)=\begin{cases}[min\{max(U_t(m_t-p_k+i_k,n_t-q_k+j_k)+S_k(p_k,q_k)|(p_k,q_k)\in D_{S_t})\\ -S_k(i_k,j_k)|(i_k,j_k)\in D_{S_t}\}-U_t(m_t,n_t)|(m_t,n_t)\in D_{U_t}], & t=k\\ 0 \quad , & (m,n)\in D_{U_t}, t\neq k\end{cases}$$

(A.5)

BIBLIOGRAPHY

1. R. C. McMaster, *Nondestructive Evaluation, Vol. 1*, Columbus, OH: The American Society for Nondestructive Testing, 1959.
2. W. J. McGonnagle, *Nondestructive Testing*, New York, NY: Gordon and Breach Science Publishers, 1982.
3. R. C. McMaster, *Nondestructive Evaluation, Vol. 2*, Columbus, OH: The American Society for Nondestructive Testing, 1959.
4. J. Krautkramer and H. Krautkramer, *Ultrasonic Testing of Materials*, New York, NY: Springer-Verlag, 1990.
5. H. L. Libby, *Introduction to Electromagnetic Nondestructive Testing Methods*, New York, NY: Wiley-Interscience Publication, 1971.
6. W. Lord, S. Nath, Y.K. Shin and Z. You, "Electromagetic Methods of Defect Detection," *IEEE Transactions on Magnetics*, Vol. 26, No. 5, pp. 2070-2075, September 1990.
7. S. R. Satish, "Parametric Signal Processing for Eddy Current NDT," Ph.D. Dissertation, Colorado State University, Fort Collins, CO, 1983.
8. R. Palanisamy, "Development of Theoretical Models for Nondestructive Testing Eddy-Current Phenomena," In *Eddy-Current Characterization of Materials and Structures, STP 722*, Edited by G. Birnbaum and G. Free, Philadephia, PA: American Society for Testing and Materials, pp. 5-21, 1981.

9. W. D. Lawson and J. H. Sabey, "Infrared Techniques," In *Research Techniques in Nondestructive Testing*, Edited by R. S. Sharpe, New York, NY: Academic Press, pp. 443-489, 1970.

10. V.P. Vavilov and R. Taylor, "Theoretical and Practical Aspects of the Thermal Nondestructive Testing," In *Research Techniques in Nondestructive Testing*, Edited by R. S. Sharpe, New York, NY: Academic Press, pp. 239-280, 1982.

11. N. K. Del Grande and P. F. Durbin, "Precise Thermal NDE for Quantifying Structural Damage," *Review of Progress in Quantitative Nondestructive Evaluation*, Vol. 15A, pp.525-531, 1996.

12. R. Halmshaw, *Nondestructive Testing*, London: Edward Arnold Publishers, 1987.

13. C.-C. Tai, J. H. Rose and J. C. Moulder, "Thickness and Coductivity of Metallic Layers from Pulsed Eddy Current Measurements," *Review of Progress in Quantitative Nondestructive Evaluation*, Vol. 15A, pp. 409-416, 1996.

14. D. Cooley, Y. S. Sun and S. S. Udpa, "Eddy Current Measurement of Thickness in Multiple-Layered Film," *Review of Progress in Quantitative Nondestructive Evaluation*, Vol. 15B, pp. 1581-1587, 1996.

15. J. Manyika and H. Durrant-Whyte, *Data Fusion and Sensor Management: A Decentralized Information-Theoretic Approach*, Chichester, West Sussex: Ellis Horwood, 1994.

16. E. L. Waltz and J. Llinas, *Multisensor Data Fusion*, Norwood, MA: Artech House, 1990.

17. R. C. Luo and M. G. Kay, "Data Fusion and Sensor Integration: State-of-the-Art 1990s," In *Data Fusion in Robotics and Machine Intelligence*, Edited by M.A. Abidi and R.C. Gonzalez, San Diego, CA: Academic Press, pp. 7-135, 1992.

18. M.A. Abidi and R.C. Gonzalez, *Data Fusion in Robotics and Machine Intelligence*, San Diego, CA: Academic Press, 1992.

19. J. Franklin, L. Davis, R. Shumaker and P. Morawski, "Military Applications," In *Encyclopedia of Artificial Intelligence*, New York, NY: Wiley, pp. 604-614, 1986.

20. M.A. Abidi and R.C. Gonzalez, "The Use of Multisensor Data for Robotic Application," *IEEE Transactions on Robotics and Automation*, Vol. RA-6, No. 2, pp. 159-177, 1990.

21. S. S. Blackman and T. J. Broida, "Multiple Sensor Data Association and Fusion in Aerospace Applications," *Journal of Robotic Systems*, Vol. 7, No. 3, pp. 445-485, June 1990.

22. A. Choudry, W. Duinker, L. O. Hertzberger and F. Tuijnman, "Simulating the Sensory-Control of an Autonomous Vechicle," *Proceedings of the 5th International Conference on Robot Vision and Sensory Controls*, pp. 147-154, 1985.

23. D. J. Kremers, C. Blahnik, A. Brain, R. Cain, J. DeCurtins, J. Mesegner and N. Peppers, "Development of a Machine-Vision Based Robotic Arc-Welding System," *Proceeding of the 13th International Symposium on Industrial Robots*, pp. 14.19-14.33, 1983.

24. I. Edward, X. E. Gros, D. W. Lowden and P. Strachan, "Fusion of NDT Data" *British Journal of NDT*, Vol. 35, No. 12, pp. 710-713, December 1993.

25. X. E. Gros, P. Strachan and D. W. Lowden, "Theory and Implementation of NDT Data Fusion," *Research in Nondestructive Evaluation*, Vol. 6, No. 4, pp. 227-236, 1995.

26. S. T. Barnard and W. B. Thompson, "Disparity Analysis of Images," *IEEE Transactions on Pattern Anaysis and Machine Intelligence*, Vol. PAMI-2, No. 4, pp. 333-340, July 1980.

27. G. Stockman, S. Kopstein and S. Benett, "Matching Images to Models for registration and Object Detection Via Clustering," *IEEE Transactions on Pattern Anaysis and Machine Intelligence*, Vol. PAMI-4, No. 3, pp. 229-241, May 1982.

28. A. V. Cideciyan, S. G. Jacobson, C. M. Kemp, R. W. Knighton and J. M. Nagel, "Registration of High Resolution Images of the Retina," *Medical Imaging VI: Image Processing*, SPIE Vol. 1652, pp. 310-322, 1992.

29. J. A. Khan, "Analysis and Interpretation of Scanning Acoustic Microscopy Images," MS Thesis, Iowa State University, Ames, IA, 1994.

30. D. L. Hall, *Mathematical Techniques in Multisensor Data Fusion*, Norwood, MA: Artech House, 1992.

31. R. C. Luo and M. G. Kay, "Multisensor Integration and Fusion in Intelligent Systems," *IEEE Transactions on Systems Man and Cybernetics*, Vol. 19, No. 5, pp. 901-931, 1989.

32. Y. Nakamura and Y. Xu, "Geometrical Fusion Method for Multi-Sensor Robotic Systems," *Proceeding of the 1989 IEEE International Conference on Robotics and Automation*, pp. 668-673, 1989.

33. G. P. Singh and S. Udpa, "The Role of Digital Signal Processing in NDT," *NDT International*, Vol. 19, No. 3, pp.125-132, June 1986.

34. M. Takadaya, J. D. Achenbach, Q. C. Guo and M. Kitahara, "Crack Parameter Characterization by a Neural Network," *Review of Progress in Quantitative Nondestructive Evaluation*, Vol. 15A, pp.797-804, 1996.

35. L. M. Brown and J. S. Lin, "Introduction of the Signature Classification Development System," *Review of Progress in Quantitative Nondestructive Evaluation*, Vol. 15A, pp.821-828, 1996.

36. S. Nath, J. P. Fulton and B. Wincheski, "Magneto-Optic Image Characterization Using Neural Networks," *Review of Progress in Quantitative Nondestructive Evaluation*, Vol. 15A, pp.891-896, 1996.

37. G. X. Xie, M. Chao, C. H. Yeoh, S. Mandayam, S. S. Udpa and L. Udpa, "Optimization of Neural Network Parameters for Defect Characterization," *Review of Progress in Quantitative Nondestructive Evaluation*, Vol. 15B, pp.2189-2196, 1996.

38. O. Rioul and M. Vetterli, "Wavelets and Signal Processing," *IEEE Signal Processing Magazine*, pp. 14-38, October 1991.

39. L. Udpa and S. S. Udpa, "Eddy Current Defect Characterization Using Neural Networks," *Materials Evaluation*, Vol. 48, No. 3, pp. 342-347, March 1990.

40. K. Sun, "NDE Data Fusion Using Phenomenological Approaches," Ph.D. Dissertation, Iowa State University, Ames, IA, 1995.

41. K. Sun, S. Udpa, L. Udpa, T. Xue and W. Lord, "Registration Issues in the Fusion of Eddy Current and Ultrasound NDE Data Using Q-Transform," *Review of Progress in Quantitative Nondestructive Evaluation*, Vol. 15A, pp. 813-820, 1996.

42. S. A. Hutchinson and A. C. Kak, "Multisensor Strategies Using Dempster-Shafer Belief Accumulation," In *Data Fusion in Robotics and Machine Intelligence*, Edited by M.A. Abidi and R.C. Gonzalez, New York, NY; Academic Press, pp. 165-209, 1992.

43. J. Yim, "Image Fusion Using Multi-Resolution Decomposition and LMMSE Filter," Ph.D. Dissertation, Iowa State University, Ames, IA, 1995.

44. J. Yim, S. S. Udpa, M. Mina and L. Udpa, "Optimal Filter Based Techniques for Data Fusion," *Review of Progress in Quantitative Nondestructive Evaluation*, Vol. 14A, pp. 773-780, 1995.

45. J. S. J. Lee, "Multiple Sensor Fusion Based on Morphological Processing," *Sensor Fusion: Spatial Reasoning and Scene Interpretation*, SPIE-Vol. 1003, pp. 94-100, 1988.

46. R. B. Thompson and D. O. Thompson, "Ultrasonics in Nondestructive Evaluation," *Proceedings of the IEEE*, Vol. 73, No. 12, pp. 1716-1755, December 1985.

47. J. Blitz, *Ultrasonics: Methods and Applications*, New York, NY: Van Nostrand Reinhold, 1971.

48. G. S. Kino, *Acoustic Waves: Devices, Imaging, and Analog Signal Processing*, Englewood Cliffs, NJ: Prentice-Hall, 1987.

49. J. A. Hudson, *The Excitation and Propagation of Elastic Waves*, Cambridge: Cambridge University Press, 1980.

50. A. D. Pierce, Acoustics: *An Introduction to Its Physical Principles and Applications*, New York, NY: McGraw-Hill, 1981.

51. E. G. Cook and H. E. Van Valkenburg, "Surface Waves at Ultrasonic Frequencies," *The American Society for Testing and Materials*, Bulletin No. 198, pp. 81-84, May 1954.

52. I. Viktorov, *Rayleigh and Lamb Waves*, New York, NY: Plenum Press, 1967.

53. D. E. Bray and R. K. Stanley, *Nondestructive Evaluation: A Tool for Design, Manufacturing and Service*, New York, NY: McGraw-Hill, 1989.

54. J. Blitz, *Elements of Acoustics*, London: Butterworths, 1964.

55. F. R. Connor, *Noise*, London: Edward Arnold Publishers, 1982.

56. S. S. Udpa, "Signal Processing for Eddy Current Nondestructive Evaluation," In *Signal Processing and Pattern Recognition in Nondestructive Evaluation of materials, NATO ASI Series, Vol. F44*, Edited by C. H. Chen, Berlin Heidelberg, Springer-Verlag, pp.129-144, 1988.

57. L. Udpa and S. S. Udpa, "Solution of Inverse Problems in Eddy-Current Nondestructive Evaluation (NDE)," Journal of Nondestructive Evaluation, Vol. 7, No. 1/2, pp. 111-120, 1988.

58. D. J. Hagemaier, "Eddy Current Impedance Plane Analysis," *Materials Evaluation*, Vol. 41, pp. 211-218, February 1983.

59. R. E. Beissner and J. L. Fisher, "A Model of Pulsed Eddy Current Crack Detection," *Review of Progress in Quantitative Nondestructive Evaluation*, Vol. 5A, pp. 189-197, 1985.

60. S. N. Rajesh, "Probability of Detection Models for Eddy Current NDE Methods," MS Thesis, Iowa State University, Ames, IA, 1993.

61. E. R. Dougherty, *An Introduction to Morphological Image Processing*, Bellingham: WA: SPIE Optical Engineering Press, 1992.

62. G. Matheron, *Random Sets and Integral Geometry*, New York, NY: Wiley, 1975.

63. J. Serra, Editor, *Image Analysis and Mathematical Morphology*, Vol. 1, New York, NY: Academic Press, 1988.

64. J. Serra, Editor, *Image Analysis and Mathematical Morphology*, Vol. 2, New York, NY: Academic Press, 1988.

65. E. R. Dougherty, *Morphological Methods in Image and Signal Processing*, Englewood Cliffs, NJ: Prentice Hall, 1987.

66. S. R. Sternberg, "Grayscale Morphology," *Computer, Vision, Graphics and Image Processing*, Vol. 35, No. 3, pp. 333-355, 1986.

67. R. C. Gonzales and P. Woods, *Digital Image Processing*, Reading, MA: Addison-Wesley, 1992.

68. X. Zhuang and R. M. Haralick, "Morphological Structuring Element Decomposition," *Computer, Vision, Graphics and Image Processing*, Vol. 35, No.3. pp. 370-382, 1986.

69. O. I. Camps, T. Kanungo and R. M. Haralick, "Gray-Scale Structuring Element Decomposition," *IEEE Transactions on Image Processing*, Vol. 5, No. 1, pp. 111-120, January 1996.

70. P. Maragos and R. W. Schafer, "Morphological Filters- Part I: Their Set Theoretic Analysis and Relations to Linear Shift Invariant Filters," *IEEE Transactions on Acoustics., Speech, Signal Processing*, Vol. 3, ASSP-35, No. 8, pp. 1153-1169, 1987.

71. E. R. Dougherty and C. R. Giardina, *Matrix Structured Image Processing*, Englewood Cliffs, NJ: Prentice-Hall, 1987.

72. E. R. Dougherty, "Optimal Mean-Square N-Observation Digital Morphological Filters. Part I: Optimal Binary Filters," *Computer Vision, Graphics, and Image Processing: Image Understanding*, Vol. 55, No. 1, pp. 36-54, January 1992.

73. E. R. Dougherty, "Optimal Mean-Square N-Observation Digital Morphological Filters, Part II: Optimal Gray-Scale Filters," *Computer Vision, Graphics, and Image Processing: Image Understanding*, Vol. 55, No. 1, pp. 55-72, January 1992.

74. R. P. Loce and E. R. Dougherty, "The Morphological Filter Mean-Absolute Error Theorem," *Nonlinear Image Processing III*, SPIE-Vol. 1658, pp. 13-24, 1992.

75. A. Morales and R. Acharta, "Non-Linear Multiscale Filtering Using Mathematical Morphology," *SPIE Nonlinear Image Processing*, Vol. 1247, pp. 160-181, 1990.

76. J. Basart, M. S. Chackalackal and R. C. Gonzalez, "Introduction to Gray-Scale Morphology," In *Advances in Image Analysis*, Edited by Y. Mahdavieh and R. C. Gonzalez, Bellingham: WA: SPIE Optical Engineering Press, pp. 306-354, 1992.

77. A. K. Jain, *Fundamentals of Digital Image Processing*, Englewood Cliffs, NJ: Prentice Hall, 1989.

78. H. C. Andrews and B. R. Hunt, *Digital Image Restoration*, Englewood Cliffs, NJ: Prentice-Hall, 1977.

79. A. Rosenfeld and A. C. Kak, *Digital Image Processing*, New York, NY: Academic Press, 1982.

80. W. K. Pratt, *Digital Image Processing*, New York, NY: Wiley, 1978.

81. N. C. Gallagher, Jr. and G. L. Wise, "A Theoretical Analysis of the Properties of Median Filters," *IEEE Transactions on Acoustics, Speech, and Signal Processing*, Vol. ASSP-29, No. 6, pp. 1136-1141, December 1981.

82. T. A. Nodes and N. C. Gallagher, "Median Filters: Some Modifications and Their Properties," *IEEE Transactions on Acoustics, Speech, and Signal Processing*, Vol. ASSP-30, No. 6, pp. 739-746, October 1982.

83. A. C. Bovik, T. S. Huang and D. C. Munson, "A Generalization of Median Filtering Using Linear Combinations of Order Statistics," *IEEE Transactions on Acoustics, Speech, and Signal Processing*, Vol. ASSP-31, No. 6, pp. 1342-1349, December 1983.

84. B. I. Justusson, "Median Filtering: Statistical Properties" In *Two-Dimensional Signal Processing II: Transforms and Median Filters*, Edited by T. S. Huang, New York, NY: Springer-Verlag, pp. 161-196, 1981.

85. T. A. Nodes and N. C. Gallagher, "The Output Distributions of Median Type Filters," *IEEE Transactions on Communications*, Vol. COM-32, No. 5, pp. 532-541, 1984.

86. P. Maragos and R. W. Schafer, "Morphological Filters-Part II: Their Relations to Median, Order-Statistic, and Stack Filters," *IEEE Transactions on Acoustics, Speech, and Signal Processing*, Vol. ASSP-35, No. 8, pp. 1170-1184, August 1987.

87. R. A. Peter, II, "A New Algorithm for Noise Reduction Using Mathematical Morphology," *IEEE Transactions on Image Processing*, Vol. 4, No. 5, pp. 554-568, 1995.

88. A. C. Bokik, "Streaking in Median Filtered Images," *IEEE Transactions on Acoustics, Speech, and Signal Processing*, Vol. ASSP-35, No. 4, pp. 493-503, 1987.

89. J. Song, R. L. Stevenson and E. J. Delp, "The Use of Mathematical Morphology in Image Enhancement," *Proceeding of the 32nd Midwest Symposium on Circuits and Systems*, pp. 67-70, 1990.

90. D. Wang, V. Haese-Coat, A. Bruno and J. Ronsin, "Some Statistical Properties of Mathematical Morphology," *IEEE Transactions on Signal Processing*, Vol. 43, No. 8, pp. 1955-1965, August 1995.

91. J. Saniie and M. A. Mohamed, "Ultrasonic Flaw Detection Based on Mathematical Morphology," *IEEE Transactions on Ultrasonics, Ferroelectrics, and Frequency Control*, Vol. 41, No. 1, pp. 150-160, January 1994.

92. K-K. Chin and J. Saniie, "Morphological Processing for Feature Extraction," *Image Algebra and Morphological Image Processing IV*, SPIE-Vol. 2030, pp. 288-302, 1993.

93. C-H. H. Chu and E. J. Delp, "Impulsive Noise Suppression and Background Normalization of Electrocardiogram Signals Using Morphological Operators," *IEEE Transactions on Biomedical Engineering*, Vol. 36, No. 2, pp. 262-273, February 1989.

94. I. R. Joughin, R. M. Haralick and E. R. Dougherty, "Model-Based Algorithm for Designing Suboptimal Morphological Filters for Restoring Subtractive-Noise-Corrupted Images," *Journal of Electronic Imaging*, Vol. 2(4), pp.314-324, October 1993.

95. J. C. Handley and E. R. Dougherty, "Model-Based Optimal Restoration of FAX Images in the Context of Mathematical Morphology," *Journal of Electronic Imaging*, Vol. 3(2), April 1994.

96. P. Salembier and L. Jaquenoud, "Adaptive Morphological Multiresolution Decomposition," *Image Algebra and Morphological Image Processing II*, SPIE-Vol. 1568, pp. 26-37, 1991.

97. Y.-W. Song and S. S. Udpa, "A New Morphological Approach for Reducing Speckle Noise in Ultrasonic Images," Presented at the *1996 Midwest Symposium on Circuits and Systems*, Ames, IA, August 18-21, 1996.

98. Y.-W. Song and S. S. Udpa, "A New Morphological Approach for Removing Speckle Noise and Emphasizing Defects in Ultrasonic Images," Presented at the *23rd Annual Review of Progress in Quantitative Nondestructive Evaluation*, Brunswick, ME, July 28-August 2, 1996.

99. H. P. Kramer and J. B. Bruckner, "Iterations of Nonlinear Transformations for Enhancement on Digital Images," *Pattern Recognition*, Vol. 7, pp. 53-58, 1975.

100. R. J. Clarke, *Digital Compression of Still Images and Video*, San Diego, CA: Academic Press, 1995.